

ADA107700

NSWC TR 3891

EXPLOSIVE SHOCK DEPOLING  
OF FERROELECTRIC CERAMICS  
FOR THE PULSE CHARGING  
OF CAPACITORS TO HIGH VOLTAGES

by  
W. H. HOLT  
T. L. BERGER  
W. MOCK, JR.  
Weapons Systems Department

JUNE 1980

Approved for public release; distribution unlimited

AD-A107700

NSWC TR 3891

UNCLASSIFIED

SECURITY CLASSIFICATION OF THIS PAGE (When Data Entered)

REPORT DOCUMENTATION PAGE		READ INSTRUCTIONS BEFORE COMPLETING FORM	
1. REPORT NUMBER NSWC/TR-3891	2. GOVT ACCESSION NO. 4D-A107700	3. RECIPIENT'S CATALOG NUMBER	
4. TITLE (and Subtitle) EXPLOSIVE SHOCK DEPOLING OF PZT FERROELECTRIC CERAMICS FOR THE PULSE CHARGING OF CAPACITORS TO HIGH VOLTAGES		5. TYPE OF REPORT & PERIOD COVERED Final	
7. AUTHOR(s) W. H. Holt T. L. Berger W. Mock, Jr.		6. PERFORMING ORG. REPORT NUMBER	
9. PERFORMING ORGANIZATION NAME AND ADDRESS Naval Surface Weapons Center (G35) Dahlgren, VA 22448		8. CONTRACT OR GRANT NUMBER(s)	
11. CONTROLLING OFFICE NAME AND ADDRESS Naval Air Systems Command Washington, DC 20360		10. PROGRAM ELEMENT, PROJECT, TASK AREA & WORK UNIT NUMBERS 62332N/832382/ WF32382501/DF29	
14. MONITORING AGENCY NAME & ADDRESS (if different from Controlling Office)		12. REPORT DATE June 1980	
		13. NUMBER OF PAGES 117	
		15. SECURITY CLASS. (of this report) UNCLASSIFIED	
		16a. DECLASSIFICATION/DOWNGRADING SCHEDULE	
16. DISTRIBUTION STATEMENT (of this Report)  Approved for public release; distribution unlimited.			
17. DISTRIBUTION STATEMENT (of the abstract entered in Block 20, if different from Report)			
18. SUPPLEMENTARY NOTES			
19. KEY WORDS (Continue on reverse side if necessary and identify by block number) Ferroelectric Ceramics      High Voltage      Alumina-Filled Epoxy Shock Depoling      Shock Waves      Manganin Gauges Capacitor Charging      Stress Attenuation Pulse Power      Explosives			
20. ABSTRACT (Continue on reverse side if necessary and identify by block number) Lead zirconate titanate (PZT) 56/44 ferroelectric ceramic materials have been shock depoled in the normal mode with capacitive loads. The shock waves were obtained via explosive plane wave techniques and shock stress attenuators. A series of explosive shock-stress attenuation experiments using manganin gauges was performed to determine the stress amplitudes obtainable with the various attenuators. The PZT material was shock loaded in the stress range from 4.6 to 13.1 GPa. Pulse powers of hundreds of kilowatts were produced in			

DD FORM 1 JAN 73 1473

EDITION OF 1 NOV 65 IS OBSOLETE  
S/N 0102-LF-014-6601

UNCLASSIFIED

SECURITY CLASSIFICATION OF THIS PAGE (When Data Entered)

UNCLASSIFIED

SECURITY CLASSIFICATION OF THIS PAGE (When Data Entered)

20. ABSTRACT (Continued)

a few microseconds. The load capacitances ranged from 0.36 to 1.7 nF. Electrical breakdown or conduction in either the PZT unit or the external circuit occurred in all the experiments. A maximum load voltage of 95 kV was produced at 7.0 GPa.

UNCLASSIFIED

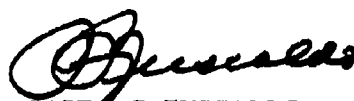
SECURITY CLASSIFICATION OF THIS PAGE (When Data Entered)

## FOREWORD

The high-voltage electrical response of lead zirconate titanate 56/44 ferroelectric ceramics has been investigated for normal-mode shock depoling. This information is important for applications involving single-shot ferroelectric pulse power sources. Funding for this work was provided by the Naval Air Systems Command (NAVAIR) Task No. A350-3500/004C/6WTW27-001.

This report has been reviewed and approved by C. A. Cooper, Head, Gun Systems and Munitions Division.

Released by:



CAPT. R. P. FUSCALDO  
Assistant for Weapons Systems  
Weapons Systems Department

Accession For	
Project	GM&I
Task	
Subtask	
Code	
Notes	
Remarks	

A

### ACKNOWLEDGEMENTS

The authors would like to acknowledge the assistance of J. B. Bickley in the fabrication of some of the PZT experimental configurations, and the assistance of C. E. Jenkins in the fabrication of experimental configurations for shock stress measurements and in pre-shot preparations at the explosive chamber facility.

## CONTENTS

	Page
I. INTRODUCTION .....	1
II. FERROELECTRIC CERAMIC MATERIAL .....	2
III. PREPARATION AND ASSEMBLY OF PZT UNITS .....	3
IV. ASSEMBLY OF EXPERIMENTAL CONFIGURATIONS .....	6
V. EXPLOSIVE SHOCK STRESS ATTENUATION MEASUREMENTS .....	13
VI. EXPLOSIVE SHOCK DEPOLING EXPERIMENTS .....	27
VII. SIMPLIFIED MODEL .....	35
VIII. RESULTS AND DISCUSSION .....	42
IX. SUMMARY .....	75
REFERENCES .....	76
APPENDIXES	
A -- DISCUSSION OF ELECTRICAL EQUATIONS FOR THE IDEAL RESPONSE OF A PZT UNIT WITH A CAPACITIVE LOAD .....	A-1
B -- VOLTAGE AND CURRENT OSCILLOSCOPE RECORDS FOR SHOCK DEPOLING EXPERIMENTS .....	B-1
C -- HUGONIOT RELATIONS FOR CASTALL 300 EPOXY .....	C-1
D -- DESCRIPTION OF BLAST CONFINEMENT CHAMBER .....	D-1
DISTRIBUTION	

## ILLUSTRATIONS

Figure		Page
1	Schematic of PZT element with electrodes. ....	2
2	Eight rectangular PZT elements and two brass electrodes prior to assembly into a unit. ....	4
3	Alignment of PZT elements and brass electrodes for assembly into a unit. ....	5
4	Completed small experimental configuration consisting of an epoxy-encapsulated PZT unit, CVR, trigger pin, and high-voltage output cable. ....	7
5	Assembly of large experimental configuration. ....	9
6	Completed large experimental configuration. ....	12
7	Stress-particle velocity curves for PZT 52/48 ceramic and Castall 300 epoxy. ....	13
8	Mold for fabricating epoxy disks. ....	14
9	Schematic of experimental configuration for shock stress attenuation measurements. ....	15
10	Schematic of epoxy-embedded low-impedance manganin gauge for shock stress measurements. ....	16
11	Piezoelectric pins and epoxy-embedded manganin gauge mounted on an aluminum plate. ....	17
12	Circuit schematic for manganin gauge and power supply. ....	18
13	Manganin gauge oscilloscope records for a shock stress measurement. ....	19
14	Peak shock stress for various thicknesses of Plexiglas attenuator. ....	21
15	Peak shock stress in Castall 300 epoxy for various epoxy thicknesses and explosive plane wave systems. ....	24
16	Peak shock stress in Castall 300 epoxy for various values of $x/x_0$ . ....	26
17	Schematics of shock depoling experiments. ....	30
18	PZT experimental configuration with an explosive plane wave lens and an explosive pad inside the blast confinement chamber. ....	36
19	Jennings high-voltage capacitor divider in camera room adjacent to the blast confinement chamber. ....	37
20	Schematic of normal-voltage-mode depoling of a PZT unit with a capacitive load. ....	38
21	Schematic of voltage and current pulses for the normal mode depoling of a PZT unit. ....	40

Figure		Page
22	Voltage and current pulses for Shot 12 . . . . .	44
23	Voltage and current pulses for Shot 15 . . . . .	45
24	Voltage and current pulses for Shot 16 . . . . .	46
25	Current pulses for Shot 38 . . . . .	47
26	Current pulses for Shot 39 . . . . .	48
27	Current pulses for Shot 40 . . . . .	49
28	Current pulse for Shot 41 . . . . .	50
29	Voltage and current pulses for Shot 42 . . . . .	50
30	Voltage and current pulses for Shot 43 . . . . .	51
31	Voltage and current pulses for Shot 44 . . . . .	52
32	Voltage and current pulses for Shot 47 . . . . .	53
33	Voltage and current pulses for Shot 58 . . . . .	54
34	Current pulse for Shot 59 . . . . .	55
35	Voltage and current pulses as a function of shock stress (Shots 12 and 15). . . . .	57
36	Current pulses as a function of shock stress (Shots 38, 39, and 40). . . . .	58
37	Voltage and current pulses as a function of shock stress (Shots 41, 42, and 43) . . . . .	59
38	Voltage and current pulses as a function of shock stress (Shots 44, 47, and 59) . . . . .	60
39	Maximum voltage as a function of shock stress . . . . .	62
40	Maximum current in the PZT unit as a function of shock stress . . . . .	63
41	Fraction of available charge released as a function of shock stress. . . . .	64
42	Fraction of available charge released as a function of $C_L/C$ . . . . .	65
43	Fraction of available charge released as a function of Castall 300 epoxy thickness . . . . .	66
44	Measured charge release compared with theoretical charge release. . . . .	67
45	Maximum electric field as a function of shock stress. . . . .	68
46	Maximum load energy as a function of shock stress . . . . .	69
47	Average power transferred to load as a function of shock stress . . . . .	70
A-1	Normalized charge and voltage on the PZT unit for various values of $C_L/C$ . . . . .	A-4
A-2	Normalized circuit current for various values of $C_L/C$ . . . . .	A-5
A-3	Normalized energy on the PZT unit for various values of $C_L/C$ . . . . .	A-7
A-4	Normalized energy on the load capacitor for various values of $C_L/C$ . . . . .	A-7
A-5	Normalized circuit energy for various values of $C_L/C$ . . . . .	A-8



Figure		Page
B-1	Voltage and current records for Shot 12 .....	B-3
B-2	Voltage and current records for Shot 15 .....	B-4
B-3	Voltage and current records for Shot 16 .....	B-5
B-4	Current records for Shot 38 .....	B-6
B-5	Current records for Shot 39 .....	B-7
B-6	Current records for Shot 40 .....	B-8
B-7	Current record for Shot 41 .....	B-9
B-8	Voltage and current records for Shot 42 .....	B-10
B-9	Voltage and current records for Shot 43 .....	B-11
B-10	Voltage and current records for Shot 44 .....	B-12
B-11	Voltage and current records for Shot 47 .....	B-13
B-12	Voltage and current records for Shot 58 .....	B-14
B-13	Current record for Shot 59 .....	B-15
C-1	Stress-particle velocity data for Castall 300 epoxy .....	C-4
D-1	Top view schematic of the blast confinement chamber (center) and appurtenant structures .....	D-3

## TABLES

Table		Page
1	Average properties of PZT elements used in depoling experiments . . . . .	3
2	Summary of measurements with Plexiglas-aluminum shock attenuation systems . . .	22
3	Summary of measurements with Castall 300 epoxy shock attenuation systems . . .	23
4	PZT/epoxy experimental configuration details . . . . .	28
5	Electrical properties of PZT units . . . . .	29
6	Electrical pulse diagnostics for shock depoling experiments . . . . .	33
7	Explosive plane wave systems for shock depoling experiments . . . . .	34
8	Data summary for shock depoling experiments . . . . .	43
9	Comparison of voltage results for the shock-depoled PZT units with calculations based on the theoretical maximum voltage assuming ideal units . . . . .	71
10	Comparison of current and charge measurements from the two CVRs used in Shots 38, 39, and 40 . . . . .	73
11	Comparison of voltage and current probe measurements of charge transferred to capacitive load . . . . .	74
C-1	Explosive shock-wave data for Castall 300 epoxy . . . . .	C-3

## I. INTRODUCTION

The work described in this report concerns the pulse charging of capacitors in the nanofarad range via the normal-mode depoling of lead zirconate titanate (PZT) ferroelectric ceramics by explosive-generated shock waves. This work is an extension of earlier capacitor charging experiments in which PZT ceramics were depoled via gas-gun projectile impact.<sup>1</sup>

It is well established that electrical energy can be obtained from poled ferroelectric ceramics either through their piezoelectric properties<sup>2,3</sup> or through depoling by shock stress.<sup>4-9</sup> In the latter case, piezoelectric charge generation is usually of secondary importance compared with the release of the surface charge that compensates the polarization.<sup>9</sup> Depending on the composition of the material, the mechanism of depoling may be either domain switching or a stress-induced phase transformation.<sup>10</sup> The electrical response of a ferroelectric ceramic to shock stress is influenced by the strong coupling between the electrical and mechanical properties, the conditions of stress loading, ceramic element geometry, electrical load, and dielectric breakdown in the material,<sup>1,4,11-19</sup> and is perhaps more complicated than any other shock-related phenomenon.<sup>9</sup>

PZT materials are usually depoled in either of two modes: normal or axial. The shock wave propagates through the PZT material in a direction either perpendicular or parallel to the PZT remanent polarization vector for normal- or axial-mode depoling, respectively. Normal-mode depoling is usually preferred for high-voltage applications, since for axial-mode depoling, time-dependent electric fields much larger than the dielectric breakdown strength of the PZT material can be generated behind the shock-depoling wave.<sup>4</sup> Also, for normal-mode depoling, the maximum electric field can be maintained at an acceptable level by either allowing sufficient thickness of ferroelectric ceramic material between the bounding electrodes of the unit or by reducing the magnitude of the PZT remanent polarization vector. For these reasons, only normal-mode depoling was considered for this work.

The details of the PZT ferroelectric ceramic material used for this work are given in Section II. The procedures for assembling the PZT materials into experimental configurations for shock depoling are presented in Sections III and IV. Shock stress measurements for various stress attenuator systems are discussed in Section V.

The PZT shock depoling experiments are described in Section VI. A simplified model for the normal-mode shock depoling of a PZT unit with a capacitive load is presented in Section VII. Section VIII contains a discussion of the results of the depoling experiments. Section IX is the summary.

The Appendixes include further discussion on the analysis of a shock-depoled ferroelectric unit with a capacitive load (Appendix A), voltage and current oscilloscope records for the depoling experiments (Appendix B), Hugoniot data for the high-voltage encapsulant material for the PZT units (Appendix C), and a brief description of the blast confinement chamber used in the explosive experiments (Appendix D).

## II. FERROELECTRIC CERAMIC MATERIAL

The ferroelectric ceramic material used for the experiments described herein is PZT 56/44, a solid solution of 56 mole percent lead zirconate and 44 mole percent lead titanate, with the minor added constituents of lanthanum, niobium, and strontium.\* This composition lies near the tetragonal-rhombohedral phase boundary of the  $\text{PbZrO}_3 - \text{PbTiO}_3$  phase diagram.<sup>10</sup> The material was normal fired. The material was in the form of rectangular elements that have an average density of  $7.57 \text{ Mg/m}^3$ . Figure 1 is a schematic of a PZT element.

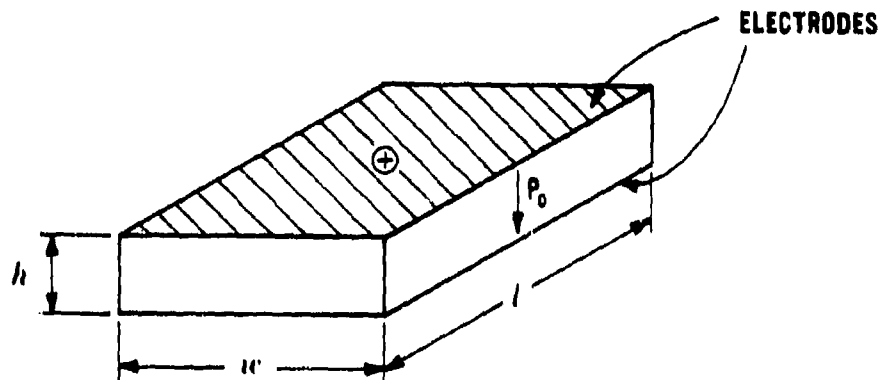


Figure 1. Schematic of PZT element with electrodes.  $h$  is the height,  $w$  is the width, and  $l$  is the length. The polarization vector has the remanent magnitude  $P_0$  and is directed from the positive to the negative electrode.

The rectangular elements were fully electroded on two sides and poled through the thickness to a remanent polarization of at least  $0.3 \mu\text{Coul/mm}^2$ . The elements had thickness tolerances of  $\pm 0.13 \text{ mm}$  and tolerances of  $\pm 0.25 \text{ mm}$  on the other dimensions. All pieces were free of cracks or chipped edges as determined by visual examination with the aid of a 10X magnifying lens. Penetration of the electroding material into the ceramic was specified to be no more than  $0.13 \text{ mm}$ . An inked (+) indicated the positive electrode. Remanent polarization, coercive field, and capacitance values were provided for each element; hysteresis loops were provided for selected elements.\*\*

For shock depoling, the PZT units were fabricated from multiple thin elements. A unit is a stack of rectangular elements with aligned polarities; the electrodes of the elements are bonded together with conductive epoxy. Thin elements can be produced more uniformly than thick elements, are less prone to cracking during fabrication, and require lower voltages to obtain the required

\* The PZT material was purchased from Gulton Industries, Inc., Fullerton, CA 92634.

\*\* These data were provided by Gulton Industries, Inc.

electric field for poling. The size and capacitance of a unit be readily selected by varying the number of elements in the unit. Four sizes of elements were used in this investigation. Representative properties of the elements are shown in Table 1.

**Table 1. Average properties of PZT elements used in depoling experiments.**

Nominal Dimensions (mm)	Total Number of Elements Used	Number of Shots	Average Remanent Polarization $P_O^a$ ( $\mu\text{C}/\text{mm}^2$ )	Average Low-Frequency Coercive Field $E_c^a$ (kV/mm)	Average Capacitance <sup>a</sup> (pF)	Average Density <sup>b</sup> (Mg/m <sup>3</sup> )
3 x 13 x 13	8	2	0.33	0.86	1210	7.56
3 x 13 x 25	80	7	0.35	0.81	2520	7.59
3 x 25 x 25	24	3	0.32	0.89	5370	7.58
6 x 25 x 51	8	1	0.40	0.82	4870	7.56

<sup>a</sup>These values are calculated from data provided for each element by Gulton Industries, Inc.

<sup>b</sup>Determined from measurements on eight elements selected at random from each nominal size group.

### III. PREPARATION AND ASSEMBLY OF PZT UNITS

The first step in PZT unit fabrication is the careful selection and preparation of the PZT elements. Each element must be free of chipped corners and edges. A chipped region will tend to fill with conductive epoxy when the pieces are assembled into a unit. These regions may serve as electrical stress concentrators and potential dielectric breakdown sites.

Figure 2 shows two brass electrodes and eight rectangular PZT elements prior to assembly. The holes in the top edges of the brass electrodes (the positive electrode has two holes and the negative electrode has one) have 0-80 UNF threads. Electrical connection to the unit is via 0-80 UNF stainless steel threaded rods. These rods also facilitate positioning of the unit during subsequent potting in an insulating epoxy. Prior to assembly of a unit, 9.5-mm-long, 0-80 UNF socket head cap screws are placed in the holes to prevent excess conductive epoxy from filling the holes. After the conductive epoxy has cured, the cap screws are removed and replaced by 1.6-mm-long socket set screws. The set screws are adjusted to be completely below the surface of the electrode edge, so as not to interfere with subsequent cleanup and lapping of the surfaces of the unit, while preventing the entry of debris into the holes.

Prior to assembly of the unit, the brass electrodes are lightly lapped with #1 grit emery paper and then cleaned with acetone. The electrode surfaces of each ceramic element are lightly lapped with #4/0 grit emery paper and then wiped with an acetone-soaked Kimwipe. The dimensions of each element are then determined with a micrometer.



**Figure 2. Eight rectangular PZT elements and two brass electrodes prior to assembly into a unit. The holes in the brass electrodes are for electrical connection to the unit via small threaded rods.**

A two-part, room-temperature-cure, silver-filled conductive epoxy paste\* (Dynaloy 326, 0.001  $\Omega\text{cm}$ ) is spread over each electrode surface. The unit is assembled by placing a PZT element against one of the brass electrodes and (observing polarities) adding elements one at a time, finishing with the other brass electrode. As each part is added, the electrode surfaces are carefully wrung together to ensure uniform epoxy coverage.

During the cure of the conductive epoxy, the unit is held in a toolmaker's clamp [Figure 3(a)]. The jaws of the clamp are lined with 0.8-mm-thick pieces of 30 durometer silicon rubber sheet. The clamp rests on a granite surface plate, and two 2.35-mm-diameter brass rods are placed between the jaws. The length of the rods is selected to be slightly shorter than the height of the PZT unit. The rods support the unit, while providing minimal contact area with any excess epoxy on the unit. As the clamp is slowly tightened on the unit, the parallelism of the jaws is monitored with a dial caliper. A machinist's rule is pressed against the elements to align their unclamped sides. After the excess epoxy has been squeezed from between the electrodes, two more brass rods are positioned on top of the unit, and a brass weight is added [Figure 3(b)]. This clamping arrangement maintains the alignment of the parts of the unit during epoxy cure. To minimize adherence of the excess epoxy, a thin film of fluorocarbon mold release agent\*\* is applied to the brass rods, clamp parts, and the granite surface plate prior to use.

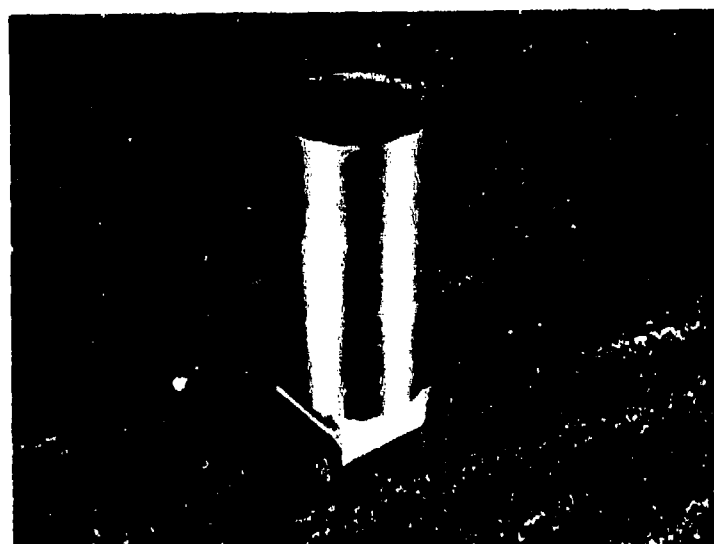
After the 24-hr cure time, the unit is removed from the clamp and the bulk excess epoxy is carefully removed with a knife. The remaining excess epoxy is removed by lapping the sides of the

\* Dynaloy, Inc., 7 Great Meadow Lane, Hanover, NJ 07936

\*\* Miller-Stephens, Inc., Route 7, Danbury, CT 06810



(a)



(b)

**Figure 3. Alignment of PZT elements and brass electrodes for assembly into a unit. (a) Alignment clamp showing jaws cushioned with rubber strips. The brass rods minimize contact of excess epoxy with the granite surface. (b) PZT elements secured by the clamp and a brass weight during cure of the conductive epoxy.**

unit with #1 grit emery paper on a granite surface plate. In the final stages of epoxy removal, it is important to lap parallel to the epoxy seams between the elements to minimize embedding of the conductive material into the ceramic surfaces. The final dimensions of the unit are then determined with a micrometer.

During and after unit assembly, all handling of the elements and unit is done with polyethylene gloves. This is to prevent contamination of the ceramic surfaces by moisture or oil from the skin. Surface contamination may degrade the adhesion of the high-voltage insulating compound and provide sites for electrical breakdown.

Capacitance measurements are performed on each unit over the frequency range 100 Hz to 100 KHz, using a General Radio Type 716C Capacitance Bridge and a Hewlett-Packard Model 4800A Vector Impedance Meter.

The finished unit is then stored in a dessicator to minimize the buildup of a moisture layer on the ceramic surfaces, pending encapsulation in the high-voltage insulating compound. Just prior to encapsulation, the surfaces of a unit are given a very light lapping with #1 grit emery paper to ensure a fresh surface for a good adherence to the insulating compound.

#### IV. ASSEMBLY OF EXPERIMENTAL CONFIGURATIONS

Two experimental configurations were used in this investigation: one designed for gas-gun impact or explosive loading with a 0.1-m-diameter plane wave system; the other designed for explosive loading with a 0.2-m-diameter plane wave system. Following a description of the potting compound, the features of the first (small) configuration will be outlined (the assembly of this configuration is described in Reference 1). The assembly of a typical large configuration will then be discussed in detail.

The high-voltage insulating compound used for encapsulating the PZT units is an aluminum oxide-filled epoxy. Castall 300 resin with RT 7 hardener.\* Aluminum oxide-filled epoxies are used in high-voltage applications because of their high dielectric strengths. The volume fraction of aluminum oxide particles in Castall 300-RT 7 is 0.37; the particles vary in size between 2 and 5  $\mu\text{m}$ , and the median size is about 8  $\mu\text{m}$ .\*\* The cured material has a density of 2.21  $\text{Mg}/\text{m}^3$ , linear shrinkage of 0.0015 cm/cm, and a volume resistivity of  $10^{16} \Omega \text{ cm}$ . The 100-KHz dielectric constant is 6.0, and the dissipation factor is 0.02. The dc short-term uniform field dielectric strength is specified to be  $1.56 \times 10^5 \text{ v/mm}$ . The 25°C cure time for Castall 300-RT 7 is 24 hr.\*

The configuration for use with a gas gun or 0.1-m-diameter explosive plane wave system consists of a special Lucite mold, a PZT unit encapsulated in Castall 300 epoxy, an instrumentation

\* Castall, Inc., East Weymouth, MA 02189

\*\* These data were provided by A. Alekna of Castall, Inc.



trigger pin, a 0.05- $\Omega$  current viewing resistor\* (CVR) and an RG-213/U output cable.\*\* For gas-gun impact, a contact closure pin is used for triggering. For explosive loading, a piezoelectric pin† is used.

Figure 4 shows a completed small experimental configuration. The diameter of the circular part of the impact side of the mold is 89 mm. The diameter of the epoxy encapsulation is 46 mm.

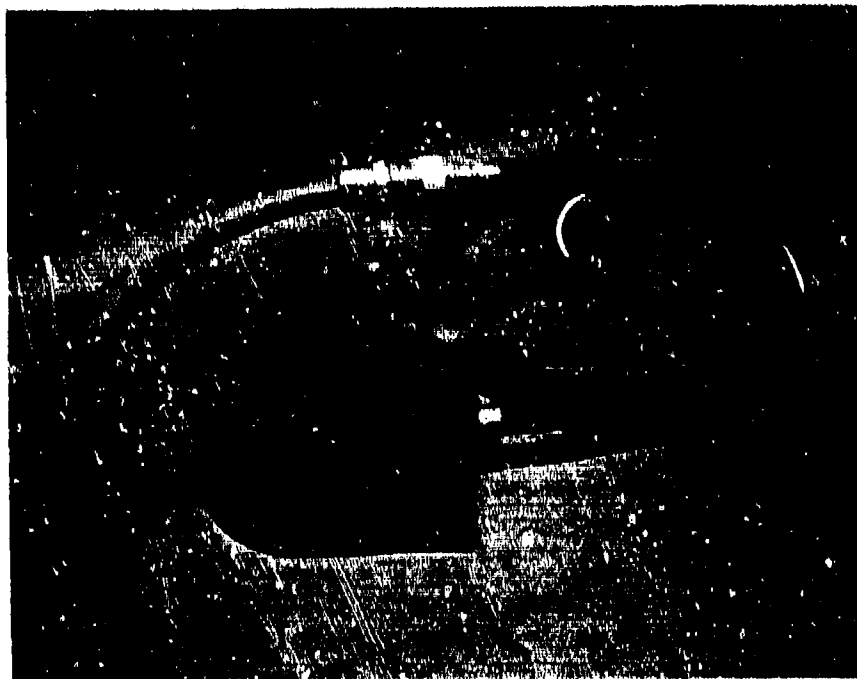


**Figure 4.** Completed small experimental configuration consisting of an epoxy-encapsulated PZT unit, CVR, trigger pin, and high-voltage output cable.

The configuration for use with a 0.2-m-diameter explosive plane wave system is based on a rectangular mold for the Castall 300 epoxy; the mold also supports a fixture for positioning single or multiple PZT units. The mold is constructed of 12.7-mm-thick Plexiglas plates and has internal dimensions of 254 x 254 x 152 mm. Each joint of the mold is held together with Homalite 1100 epoxy base adhesive†† and three ¼-20 UNC nylon screws. A granite surface plate forms the temporary base of the mold.

\* T&M Research Products, Inc., 129 Rhode Island, N.E., Albuquerque, NM 87108

\*\* Times Wire and Cable Co., 3586 Hall Avenue, Wallingford, CT 06492

† Valpey-Fisher Corporation, 75 South Street, Hopkinton, MA 01748

†† Homalite Corporation, 11 Brookside Drive, Wilmington, DE 19804

Figure 5(a) shows a Plexiglas mold, the aluminum positioning fixture, two PZT units, and two instrumentation trigger pins. The fixture has three cross pieces: one for the PZT units and two for instrumentation trigger pins. The PZT units are each suspended on three 0-80 UNF threaded rods. The trigger pins consist of piezoelectric shock-time-of-arrival pins (Valpey-Fisher Pinducers, Part No. VP-1093-1.5)\* that are encapsulated in Castall 300 epoxy to form a configuration called a spikeducer<sup>20</sup> to facilitate positioning in the rectangular mold.

The vertical positions of the PZT units and spikeducers are gauged, while the mold rests on a granite surface plate (the bottom edge of the mold has been lapped flat). Adjustable parallels (cleaned in acetone and dried thoroughly) are preset to the desired heights using a micrometer. The PZT units with threaded rods are allowed to rest on top of the parallels, then 0-80 UNF nuts are tightened on each side of the center horizontal strip of the fixture to secure the units in the desired position. The tips of the spikeducers are set a predetermined distance below the bottom of the PZT units, so that the shock wave reaches them prior to reaching the PZT. The recording oscilloscopes are thereby triggered a short time before the electrical output from the PZT occurs. After the spikeducers are positioned, they are secured by tightening the collet clamps on the aluminum fixture.

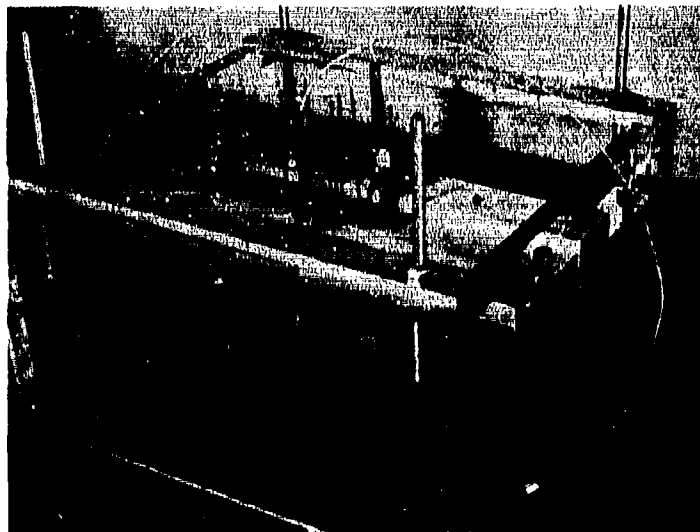
Fiducial marks are placed on the fixture and mold for repositioning reference, and the fixture with attached PZT units and spikeducers is transferred to another Plexiglas mold for support, pending encapsulation in the mold in which the units were gauged.

The encapsulation of the PZT units in the Castall 300 epoxy is accomplished in several steps. If more than a 200-gm mass of this material is cast at one time, the exothermic curing reaction can cause an excessive temperature rise, which results in nonuniform curing and significant thermo-mechanical stresses in the epoxy and the mold. Shrinkage of the epoxy upon completion of the cure and return to ambient temperature may also cause failure of the bond with the PZT surface.

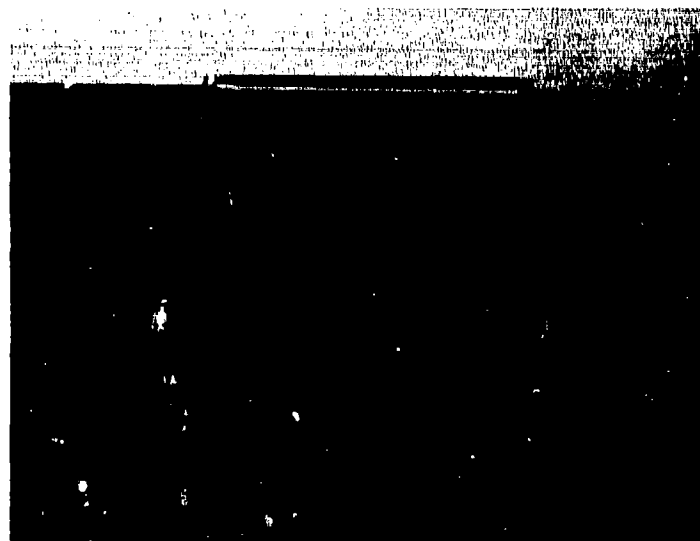
The first step is to coat the granite surface plate with a thin layer of fluorocarbon mold release agent. The lapped base of the mold is placed on the granite surface, and the mold is secured to the granite with duct tape. A narrow bead of silicone grease is placed around the inside edge of the base of the mold to ensure that no epoxy leaks under the Plexiglas. The excess grease is carefully removed with a Kimwipe.

A rectangular block of teflon (75 × 38 × 130 mm) is suspended from the aluminum fixture at the position of the PZT units. The distance from the granite surface to the bottom of the teflon block is approximately 4 mm less than the corresponding distance for the PZT units. Vacuum degassed (1 Pa, 10 min) epoxy is then poured into the mold to a level at least 4 mm above the height of the top of the PZT units. Additional vacuum processing (1 Pa, 15 min) removes any air entrained during pouring. After the epoxy has cured, the teflon block is easily removed, since the epoxy shrinks away from it slightly. A rectangular cavity remains for subsequent insertion of the PZT units. A carbide-tipped bit (15.8 mm diameter) is used to drill vertical holes near the cavity to accommodate the spikeducers.

\* Valpey-Fisher Corporation, 75 South Street, Hopkinton, MA 01748

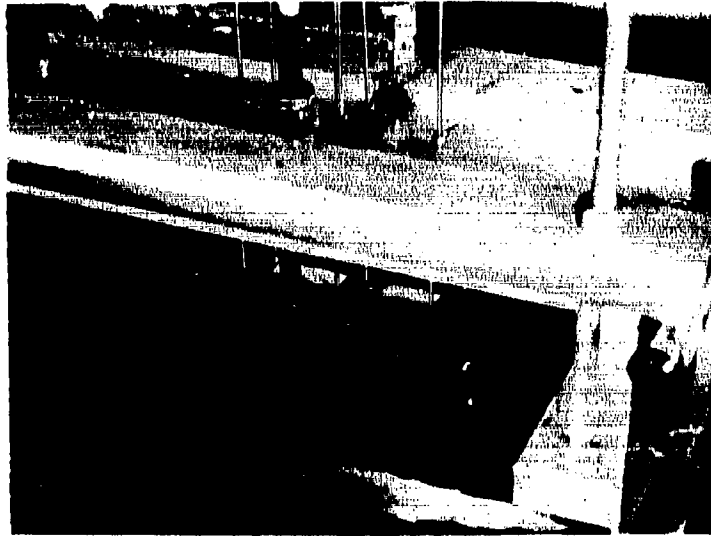


(a)



(b)

**Figure 5. Assembly of large experimental configuration. (a) Potting mold with positioning frame for PZT units and spikeducers. (b) Mold with preformed cavities in potting compound. (c) Positioning of PZT units and spikeducers during configuration assembly.**



(c)

Figure 5. Assembly of large experimental configuration. (Continued)

At this stage, the mold appears as shown in Figure 5(b). The sides of the mold and thickness of the epoxy at the base of the rectangular cavity are then measured with a vernier height gauge and extension probe. The partially filled mold is then removed from the granite surface plate by carefully driving razor blade wedges under the edges of the mold. The surface that was in contact with the granite is then lapped (Highland Park Manufacturing Model 27VL lapping machine)\* to remove any nonplanarity due to distortion during epoxy curing. The mold and epoxy are then gauged again so that the final height of the PZT units above the flat surface can be determined.

The aluminum fixture with the PZT units and spikeducers is then repositioned on the mold as shown in Figure 5(c). The side clearance between the PZT units and the cured compound is less than about 6 mm. Degassed epoxy is then added to a height of at least 4 mm above the top of the PZT units. Entrained air is removed by further vacuum processing.

The above approach to the encapsulation of the PZT units provides a large area of epoxy for plane wave shock loading, while minimizing the amount of epoxy that cures in contact with the PZT. Thermomechanical effects on the units are thereby minimized. After the epoxy has cured, capacitance measurements are performed on each encapsulated unit.

The next step is the electrical connection of the PZT units to a CVR and a high-voltage output cable. The units are connected together by wrapping #16 AWG tinned copper wire around the O-80

\* Highland Park Manufacturing Division, Musto Industries, Inc., 12600 Chadron Avenue, Hawthorne, CA 90250

UNF threaded rods. Heat sinks made of wet Kimwipes are placed around each rod between the wrapped wire and the surface of the epoxy. The wire and rods are then joined with low-temperature silver solder. This procedure prevents thermal damage to the epoxy or to the PZT units. The CVR (T&M Research Products SDN414-.05,  $0.05 \Omega$ )\* is then soldered to the negative terminal of the PZT units.

The connection of the end of the RG-220/U high-voltage output cable\*\* to the PZT units is accomplished as follows. About 0.3 m of the cable jacket is removed. The braided outer conductor is loosened and pulled back over itself to expose about 0.25 m of dielectric. The folded-back braid is then flared and tapered outward for a length of about 70 mm to help prevent an abrupt spatial change of the electric field in the dielectric. The dielectric is trimmed to expose the copper center conductor for about 12 mm beyond the dielectric.

The cable is then supported from above the power supply by a rigid frame. A 0.3-m length of 102-mm-O.D., 3.2-mm-wall-thickness Plexiglas tubing is slipped over the cable. The cable center conductor is then tied to the positive terminal of the PZT units with #16 AWG copper wire and is silver soldered. The CVR is connected to the braid of the RG-220/U cable via a short length of 13-mm-wide braided ground strap. The cable braid and the ground strap braid are placed together, wrapped tightly with #22 AWG tinned copper wire, and soldered. The bottom of the Plexiglas tube is placed against the top of the cured Castall 300 epoxy and sealed to it with fast-setting epoxy (Hardman Epoweld 8173).†

Degassed Castall 300 epoxy is poured into the Plexiglas tube to form an insulating support for the RG 220/U cable. Additional Castall 300 is poured outside the tube, inside the rectangular mold. Figure 6(a) shows a completed large PZT experimental configuration. The large cable at the top is the RG-220/U, and the smaller RG-188/U cables lead to the spikeducers and the CVR. In Figure 6(b), the configuration has been turned on its side to show the lapped epoxy surface that will be in contact with an explosive plane wave system.

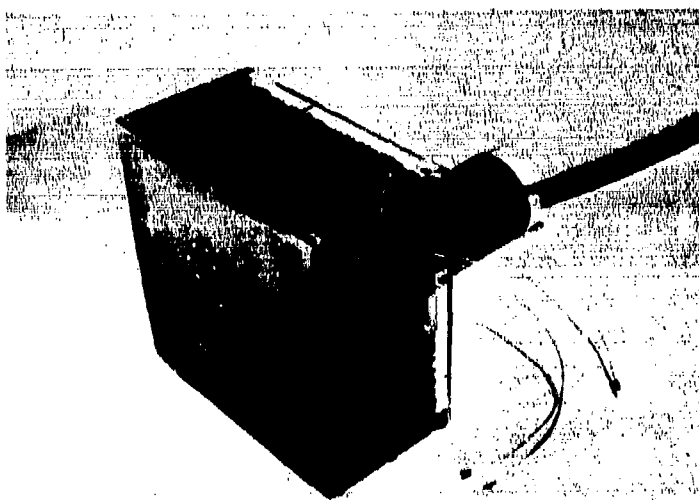
\* T&M Research Products, Inc., 129 Rhode Island, N.E., Albuquerque, NM 87108

\*\* Times Wire and Cable Co., 3586 Hall Avenue, Wallingford, CT 06492

† Hardman, Inc., Belleville, NJ 07109



(a)



(b)

**Figure 6. Completed large experimental configuration. (a) Side view. (b) View showing lapped bottom surface.**

## V. EXPLOSIVE SHOCK STRESS ATTENUATION MEASUREMENTS

Previous work on the shock depoling of ferroelectric ceramics has shown that the shock stress amplitudes of interest are in the range below about 10 GPa.<sup>1,4,5,7,9</sup> A comparison of the Hugoniot relations for a PZT ceramic<sup>21</sup> and for Castall 300 epoxy<sup>22</sup> with the reflection characteristics of representative common explosives<sup>23</sup> (Figure 7) shows that stress amplitudes below about 10 GPa are not attainable without some kind of shock attenuator system. For this reason, a series of explosive experiments using manganin stress gauges was performed to determine the stress amplitudes obtainable with various attenuators. Two attenuator systems were investigated: Plexiglas and aluminum, and Castall 300 epoxy.

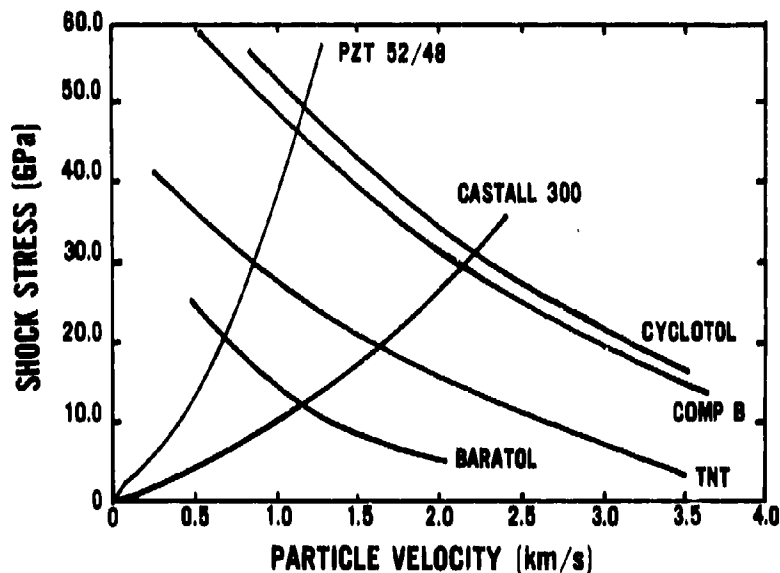


Figure 7. Stress-particle velocity curves for PZT 52/48 ceramic and Castall 300 epoxy. The intersections of these curves with the reflection characteristics for selected explosives give the particle velocities and stress amplitudes in the inert materials in contact with the explosives, for normally incident plane detonation waves. Data for PZT 52/48 are shown, since the Hugoniot for PZT 58/44 has not been determined.

The Plexiglas-aluminum attenuator system consisted of stacks of two 2024-T3 aluminum alloy plates with various numbers of Plexiglas plates. The plates each had the dimensions of 102 × 102 × 6.35 mm. The Plexiglas plates were hand lapped on a granite surface plate with #2/0 grit emery paper. The aluminum plates were milled flat and then hand lapped. The plates were coated with a thin film of silicone diffusion pump oil to minimize air gaps between the plates.

Figure 8 is a schematic of the mold for fabricating disks of Castall 300 epoxy. The thickness of a disk was determined by the height of a Plexiglas cylinder that formed the central part of the mold. Plexiglas disks formed the sides of the mold. A thin film of silicone vacuum grease sealed the disks to the cylinder. The inside of the mold was coated with a thin layer of fluorocarbon mold release. Vacuum-degassed (1 Pa, 10 min) Castall 300-RT 7 epoxy was poured into the mold through the fill hole. Entrained air was removed by additional vacuum processing (1 Pa, 10 min). Loss of epoxy due to bubbling was prevented by the reservoir. After a 24-hr room-temperature cure cycle, the epoxy plate was removed from the mold.

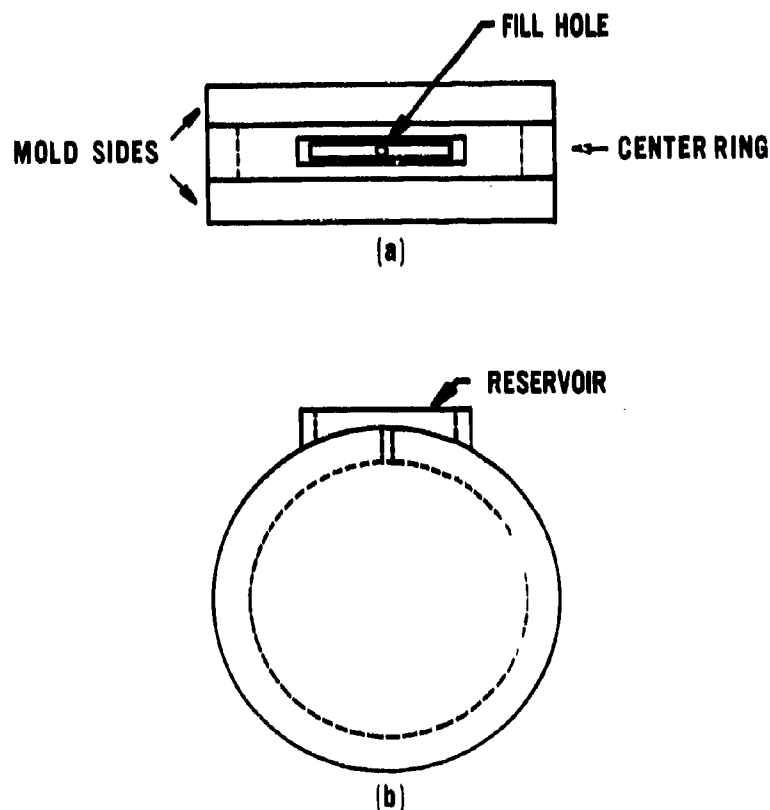


Figure 8. Mold for fabricating epoxy disks. (a) Top view. (b) Side view.



Figure 9 is a schematic of an attenuator experiment. The detonator initiates the explosive plane wave lens that produces a plane detonation wave in the explosive pad. When the detonation wave reaches the surface of the attenuator system, a nonuniform plane shock wave is transmitted into the attenuator. The stress-time history at the back surface of the attenuator system was monitored with a manganin gauge.

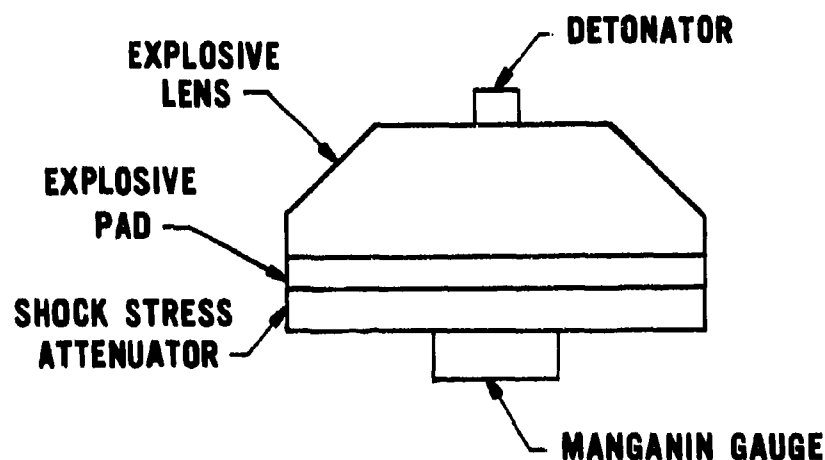


Figure 9. Schematic of experimental configuration for shock stress attenuation measurements.

Conventional high-explosive techniques were used in all the shock stress attenuation and shock depoling experiments. All the explosive plane wave lenses were purchased through ERDA.\* Both 102-mm-diameter (P-40) and 203-mm-diameter (P-80) lenses were used. For lenses of this type, there is a pressure gradient across the face of the lens, but the detonation front is planar to within 100-ns over the entire face.<sup>24</sup> All explosive pads used with the plane wave lenses were either cast or pressed Baratol and were fabricated by the Explosives Division of the Naval Surface Weapons Center (NSWC). A thickness tolerance of  $\pm 0.05$  mm was maintained on these pads. A single SE-1 detonator\*\* was used with each plane wave lens.

\* U.S. Energy Research and Development Administration (now U.S. Department of Energy), Albuquerque Operations Office, Special Programs Division, P.O. Box 5400, Albuquerque, NM 87115  
 \*\* Monsanto Research Corporation, Miamisburg, OH 45342

Pulsar Model 741M low-impedance manganin gauges\* were used to measure the shock stress at the back surface of the attenuator system. The vendor-supplied characteristics for these gauges are as follows:

Frequency Response = dc to 70 MHz

Electrical Impedance =  $< 1 \Omega$

Nominal Recording Duration = 6  $\mu$ s

Risetime (10 to 90 percent) = 60 ns

Resistance Sensitivity = +2.9 percent/GPa

Dimensions of Wire Sensor = 6.35 mm long  $\times$  0.076 mm diameter

Depth of Sensor in Epoxy = 0.51 mm

Overall Transducer Dimensions = 6.35 mm diameter  $\times$  31.8 mm thick

Epoxy Matrix = Armstrong C-7\*\*

Accuracy =  $\pm 3$  percent

Figure 10 shows end and side schematics of a low-impedance manganin gauge. Figure 11 shows a manganin gauge and alignment fixture for one of the Plexiglas-aluminum attenuation shots. A thin film of silicone vacuum grease was placed on the gauge surface to ensure good mechanical coupling to the aluminum.

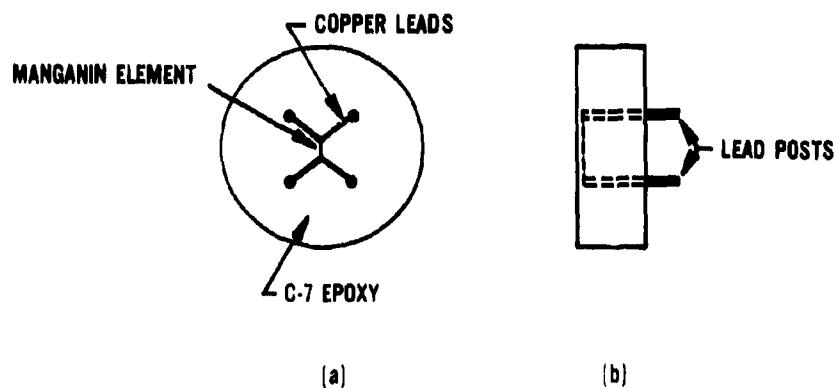
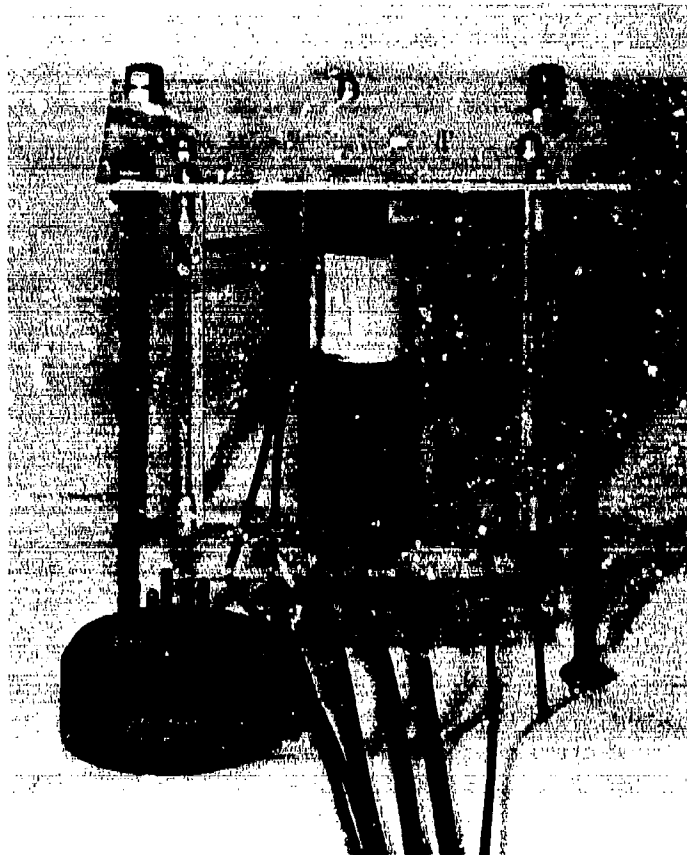


Figure 10. Schematic of epoxy-embedded low-impedance manganin gauge for shock stress measurements. (a) End view. (b) Side view.

\* Pulsar Instruments, Inc., 650 Vaqueros Avenue, Sunnyvale, CA 94086

\*\* Armstrong Products Co., Inc., Argonne Road, Warsaw, IN 46580



**Figure 11. Piezoelectric pins and epoxy-embedded manganin gauge mounted on an aluminum plate. The shock stress attenuator, explosive pad, and explosive plane wave lens are to be mounted on top of the plate. An unmounted epoxy-embedded manganin gauge is shown in the left foreground.**

Low-impedance manganin gauges are used with a constant current pulsed power supply as shown schematically in Figure 12. Current is supplied to the gauge a few tens of microseconds before the arrival of the shock front. Pulsed operation is necessary to minimize gauge heating and prevent loss of calibration. The 50- $\Omega$  ballast resistors shown in Figure 12 are housed in an adaptor that plugs into the back of the gauge (Figure 11). A Pulsar Model 301 pulsed power supply was used with the gauges. It has three independent output channels and three independent trigger channels. The output pulse widths are adjustable from approximately 10 to 100  $\mu$ s. Droop of the pulse amplitude is less than 2 percent. The threshold level for triggering is  $\pm 5$  v, and full-current turn-on follows in less than 1  $\mu$ s.

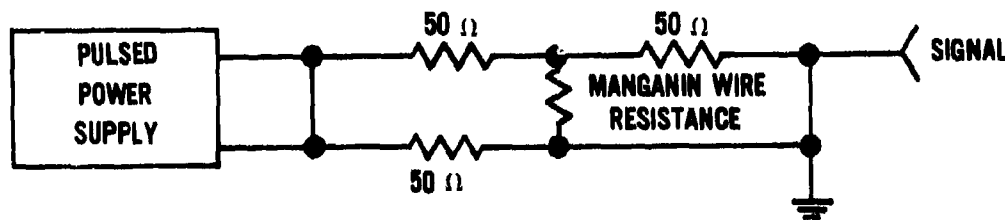


Figure 12. Circuit schematic of manganin gauge and power supply.

Valpey-Fisher Pinducers were used for triggering (several of the trigger pins are shown in Figure 11). Appropriate timing delays were obtained with a Cordin Model 416 six-channel digital delay generator.\* Delays are adjustable from 1 to 9999.9  $\mu\text{s}$  in increments of 100 ns. The accuracy is specified to be 100 ns or  $\pm 0.01$  percent, and the jitter is less than 30 ns.

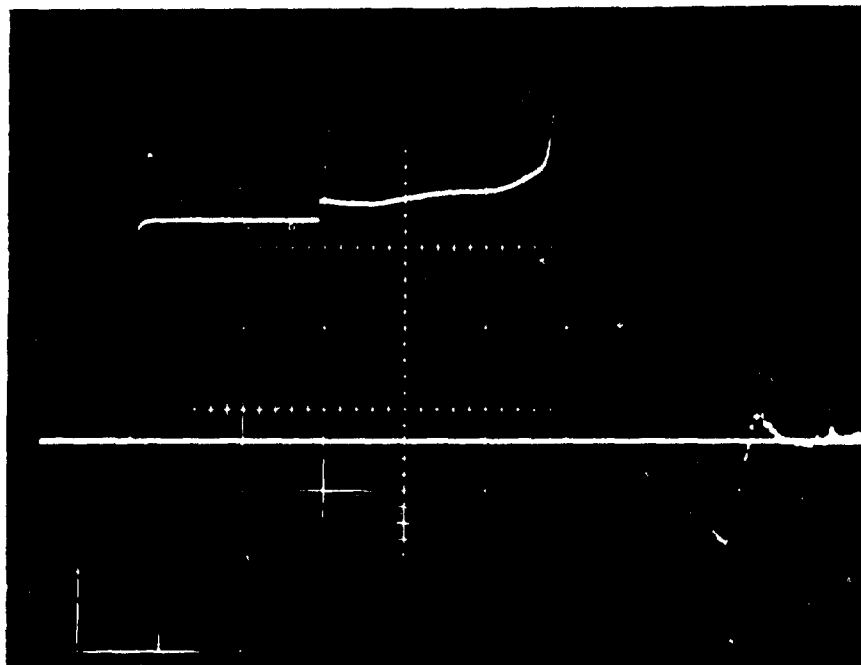
One of the delay generator channels was used to trigger a pulse switching unit that fired the electric detonator. All timing was referenced to the delay time of this firing channel, which was taken to be the zero of time.

The manganin gauge power supply was triggered by the delay generator approximately 10  $\mu\text{s}$  before the arrival of the shock front at the manganin element. This was accomplished by using the experimentally measured value of the breakout time at the face of the plane wave lens, the Baratol detonation velocity ( $\sim 4.9$  km/s), the thickness of the Baratol pad, and the known shock velocities and thicknesses for the attenuator materials.

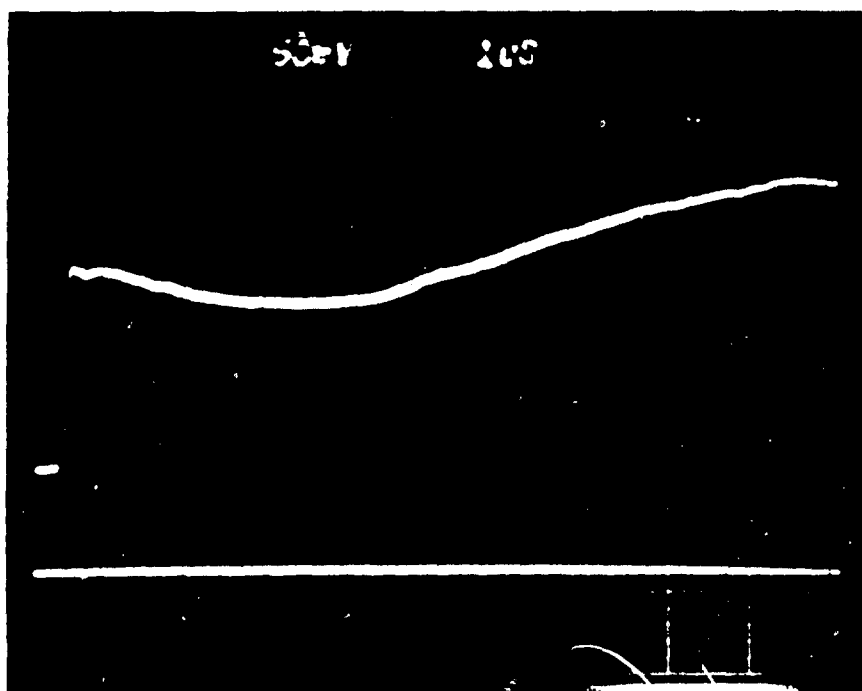
Pick-off probes (Tektronix VP-1/P6057, 100X) permitted the use of multiple oscilloscopes to monitor the voltage across the manganin gauge element. One of the scopes was always operated at a relatively large deflection factor (0.5 V/div) and slow sweep speed (5  $\mu\text{s}/\text{div}$ ). The other scopes were operated with smaller deflection factors and faster sweep speeds and were used to monitor only the change in voltage across the manganin element. These higher-resolution records were obtained by means of differential comparator plug-in amplifiers (Tektronix 7A13).

Figure 13 shows example oscilloscope records for a shock stress measurement. Figure 13(a) shows the overall manganin gauge record, which includes the initial voltage,  $V_0$ , and the change in voltage,  $\Delta V$ . Figure 13(b) is a more sensitive record of the voltage change; this type of record was used to obtain the voltage change value for each shot. Figure 13(c) is a record of the initial voltage across the manganin element. This record was obtained just prior to firing the shot.

\* Cordin, 2230 South 3270, West Salt Lake City, UT 84119

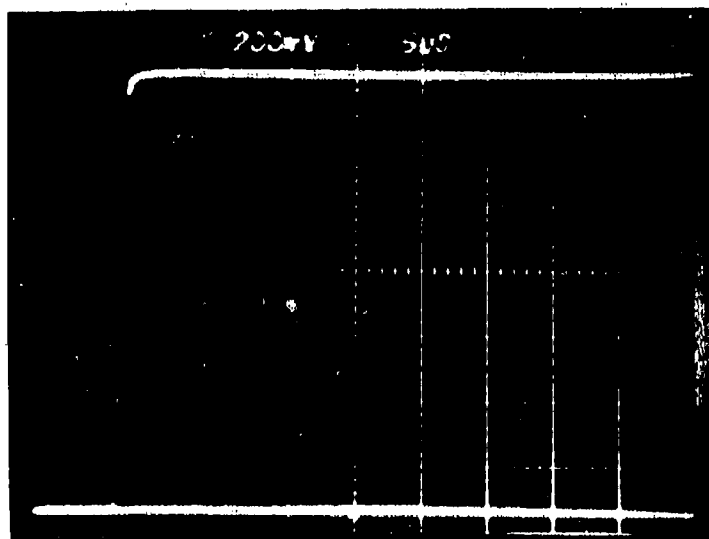


(a)



(b)

Figure 13. Manganin gauge oscilloscope records for a shock stress measurement. These records are from Shot 36. (a) Record showing initial voltage and change in voltage. The vertical scale is 0.5 V/div and the horizontal scale is 5  $\mu$ s/div. (b) More sensitive record of change in voltage across manganin element (obtained with differential amplifier oscilloscope plug-in unit). The vertical scale is 50 mV/div and the horizontal scale is 1  $\mu$ s/div. (c) Pre-shot calibration record showing pulsed initial voltage across manganin element. The vertical scale is 200 mV/div and the horizontal scale is 5  $\mu$ s/div.



(c)

Figure 13. Manganin gauge oscilloscope records for a shock stress measurement. (Continued)

The shock stress in the C-7 epoxy may be determined from the relation

$$\frac{\Delta R}{R_0} = \frac{\Delta V}{V_0} = \sigma_x K_D \quad (1)$$

where  $R_0$  is the initial resistance of the manganin element,  $\Delta R$  is the change in the resistance,  $\sigma_x$  is the shock stress, and  $K_D$  is the dynamic piezoresistance coefficient. The resistance of manganin has been reported to be a nonlinear function of shock stress in the 0.4- to 4.0-GPa range, but in the 4.0- to 9.4-GPa range the response is linear and  $K_D$  has the constant value  $2.9 \times 10^{-2} \Omega/\Omega/\text{GPa}$ .<sup>25</sup> Since the anticipated stress values were all in excess of 4.0 GPa, the constant value of  $K_D$  was used.

The values of  $\Delta V$  and  $V_0$  were obtained from the oscilloscope records with the aid of a tool-maker's microscope. The shock stress in C-7 epoxy was then calculated from Equation (1).

The shock stress amplitudes in the attenuator materials can be calculated by the impedance-match technique.<sup>24</sup> The measured stress in C-7 epoxy and the Hugoniot relations for C-7 epoxy<sup>25</sup> are used along with the Hugoniot relations for the attenuator materials.<sup>22, 26, 27</sup>

The experimental conditions and results of the present work on shock attenuation systems are presented in Tables 2 and 3. These tables include the details of the explosive plane wave lens, Baratol explosive pad, and attenuator material thicknesses and the shock stress, shock wave velocity, and particle velocity in the attenuator materials.

Figure 14 is a plot of the peak shock stress at the back surface of the 2024-T3 aluminum as a function of the thickness of the Plexiglas attenuator. The peak shock stress in the aluminum is seen to decrease linearly as the thickness of the Plexiglas increases. The straight line in the figure is a least-squares fit to the data. The equation of this line is

$$\sigma_x = 15.6 - 0.224x \quad (2)$$

where  $\sigma_x$  is the peak shock stress in GPa at the back surface of the aluminum and  $x$  is the thickness in mm of the Plexiglas.

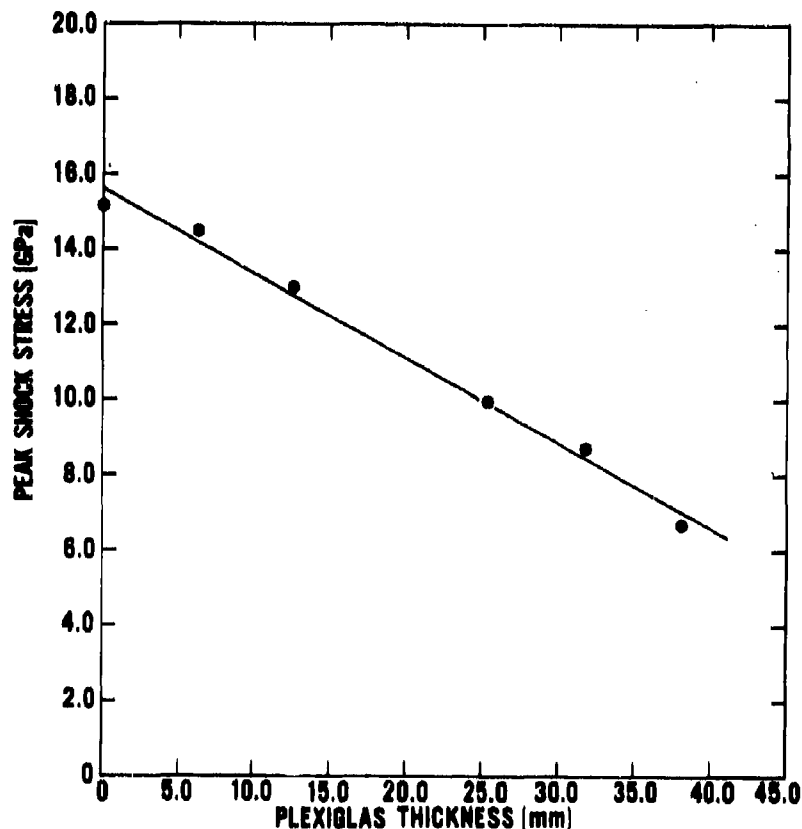


Figure 14. Peak shock stress (measured at the back of the aluminum plate) for various thicknesses of Plexiglas attenuator. Data are from Table 2. The straight line is a least-squares fit to the data.

Table 2. Summary of measurements with Plexiglas-aluminum shock attenuation systems.

Shot Number	Plane Wave Lens	Baratol Pad Diameter (mm)	Baratol Pad Thickness (mm)	Baratol Composition, Fabrication	Baratol Density (Mg/m <sup>3</sup> )	Plexiglas Thickness <sup>a</sup> (mm)	Aluminum Thickness <sup>b</sup> (mm)	Shock Velocity in C-7 Epoxy (km/s)	Particle Velocity in C-7 Epoxy (km/s)	Shock Stress in C-7 Epoxy (GPa)	Shock Velocity in Aluminum (km/s)	Particle Velocity in Aluminum (km/s)	Shock Stress in Aluminum (GPa)
11	P-40	102	50.8	73/27, <sup>c</sup> cast	2.45	31.8	12.7	3.85	0.802	3.66	6.02	0.518	8.6
13	P-40	102	50.8	73/27, cast	2.48	38.1	12.7	3.64	0.643	2.78	5.88	0.411	6.7
17	P-40	102	50.8	73/27, cast	2.40	25.4	12.7	3.99	0.905	4.28	6.12	0.588	10.0
18	P-40	102	50.8	73/27, cast	2.39	0	12.7	4.50	1.27	6.78	6.45	0.842	15.0
19	P-40	102	50.8	73/27, cast	2.37	6.40	12.7	4.43	1.22	6.44	6.41	0.809	14.4
20	P-40	102	50.8	75/25, <sup>d</sup> pressed	2.46	12.7	12.7	4.30	1.13	5.72	6.32	0.740	13.0

<sup>a</sup>Single or stacked Plexiglas plates were used; each plate had a nominal thickness of 6.35 mm.

<sup>b</sup>Two stacked 6.35-mm-thick 2024-T3 aluminum plates were used for each shot.

<sup>c</sup>73% barium nitrate, 27% TNT

<sup>d</sup>75% barium nitrate, 25% TNT



Table 3. Summary of measurements with Castall 300 epoxy shock attenuation systems.

Shot Number	Plane Wave Lens	Baratol Pad Diameter (mm)	Baratol Pad Thickness (mm)	Baratol Composition, Fabrication	Baratol Density (Mg/m <sup>3</sup> )	Castall 300 Epoxy Thickness (mm)	Shock Velocity C-7 Epoxy (km/s)	Particle Velocity in C-7 Epoxy (km/s)	Shock Stress in C-7 Epoxy (GPa)	Shock Velocity in Castall 300 Epoxy (km/s)	Particle Velocity in Castall 300 Epoxy (km/s)	Shock Stress in Castall 300 Epoxy (GPa)	Nominal Thickness of Plane Wave Lens <sup>d</sup> (mm)	Nominal Total Thickness of Explosive <sup>e</sup> (mm)	Nominal $\lambda/\lambda_0$ Ratio <sup>f</sup>
21	P-40	102	50.8	75/25, <sup>a</sup> pressed	2.46	1.59	4.51	1.28	6.84	4.44	1.02	10.0	45	96	0.017
31	P-40	102	25.4	76/24, <sup>b</sup> pressed	2.69	25.4	3.92	0.86	4.01	3.89	0.68	5.9	45	70	0.36
32	P-40	102	25.4	76/24, <sup>b</sup> pressed	2.33	6.20	4.27	1.11	5.64	4.23	0.89	8.3	45	70	0.089
33	P-40	102	50.8	76/24, <sup>b</sup> pressed	2.30	25.4	3.87	0.82	3.79	3.84	0.653	5.6	45	96	0.27
34	P-40	102	25.4	76/24, <sup>b</sup> pressed	2.33	18.5	4.06	0.96	4.61	4.02	0.76	6.8	45	70	0.26
35	P-40	102	50.8	76/24, <sup>b</sup> pressed	2.30	13.2	4.20	1.06	5.25	4.15	0.840	7.7	45	96	0.14
36	P-40	102	50.8	76/24, <sup>b</sup> pressed	2.30	31.2	3.74	0.72	3.18	3.70	0.57	4.6	45	96	0.33
45	P-80	203	25.4	76/24, <sup>b</sup> pressed	2.51	45.7	4.06	0.96	4.65	4.03	0.77	6.8	102	127	0.36
46	P-80	203	25.4	76/24, <sup>b</sup> pressed	2.52	45.7	3.98	0.90	4.24	3.94	0.713	6.2	102	127	0.36
57	P-80	203	25.4	76/24, <sup>b</sup> pressed	2.50	3.18	3.64	0.677	2.96	2.83	0.690	4.3	102	127	g

<sup>a</sup>25% barium nitrate, 25% TNT

<sup>b</sup>6% barium nitrate, 24% TNT

<sup>c</sup>Plexiglas-copper-Castall 300 epoxy attenuation system; two stacked 6.35-mm-thick Plexiglas layers and two stacked 6.35-mm-thick copper layers were between the Baratol pad and the epoxy. The Plexiglas was in contact with the Baratol pad.

<sup>d</sup>Largest dimension normal to plane wave surface.

<sup>e</sup>Sum of plane wave lens thickness and Baratol pad thickness.

<sup>f</sup>Ratio of attenuator thickness  $\lambda$  to total explosive thickness  $\lambda_0$ .

<sup>g</sup>Not applicable for inhomogeneous attenuator.

The shock stress in Castall 300 epoxy was found to decrease linearly with the propagation distance in the material for those shots with 102-mm-diameter (P-40) explosive plane wave lenses. This behavior is shown in Figure 15. The straight line in the figure is a least-squares fit to the data and has the equation

$$\sigma_x = 9.85 - 0.166x \quad (3)$$

where  $\sigma_x$  is the stress in GPa and  $x$  is the Castall 300 thickness in mm.

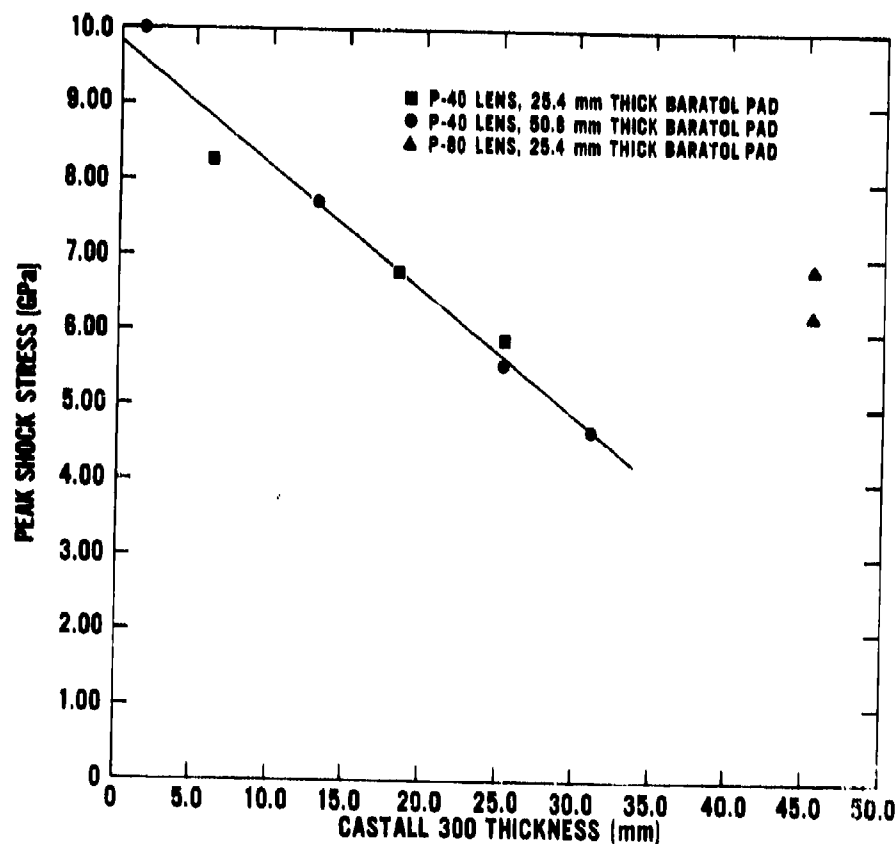


Figure 15. Peak shock stress in Castall 300 epoxy for various epoxy thicknesses and explosive plane wave systems. Data are from Table 3. The straight line is a least-squares fit, excluding the points for the experiments using P-80 lenses.

Equation (3) is not valid for the shots with 203-mm-diameter (P-80) explosive plane wave lenses and pads. For  $x \approx 46$  mm, the measured stress is approximately a factor of three greater than would be predicted by Equation (3). An approximate analytical expression for the peak shock stress in the Castall 300 as a function of propagation distance may be obtained for the 203-mm-diameter plane wave lenses and Baratol pads used in this work in the following manner. First, the two experimentally measured stresses at 26 mm into the Castall 300 are averaged. Then, using the fact that the shock stress generated in a given substance due to in-contact explosive detonation depends only on the characteristics of the explosive, from Equation (3), the shock stress in the Castall 300 at the explosive-Castall 300 interface is 9.85 GPa. The equation of the line through the two data points at 46 mm and the 9.85 GPa value for  $x = 0$  gives

$$\sigma_x = 9.85 - 0.073x \quad (4)$$

where again  $\sigma_x$  is in GPa and  $x$  is in mm.

A traditional method of presenting explosive shock wave attenuation data is to plot the peak shock stress as a function of the dimensionless quantity  $(x/x_0)$  where  $x$  is the distance into the attenuator material and  $x_0$  is the explosive slab thickness.<sup>23</sup> However, this procedure is not strictly correct in these experiments because the plane wave lens is also an explosive and contributes to the effective explosive thickness.<sup>28</sup> Figure 16 shows the peak shock stress plotted as a function of  $x/x_0$  where  $x$  is the distance into the Castall 300 epoxy from the Baratol-epoxy interface and  $x_0$  is the sum of the Baratol pad thickness and the height of the explosive plane wave lens (the data for this figure are given in Table 3). The straight line is a least-squares fit to the data points, excluding the points for Shots 33 and 36, having shock stress values of 4.6 and 5.6 GPa, respectively. These two stress values are considerably lower than the trend of the other data points; this is probably due to relief waves from the boundaries of the explosive or to relief waves from the sides of the (102-mm-diameter) Castall 300 disks that reduce the peak stress at the manganin gauge. This effect was probably important only in these two shots because of the more favorable diameter-to-thickness ratios for the Castall 300 disks used in the other shots. The least-squares fit gives

$$\sigma_x = 9.48 - 9.25 (x/x_0) \quad (5)$$

where  $\sigma_x$  is in GPa and  $x$  and  $x_0$  are in mm.

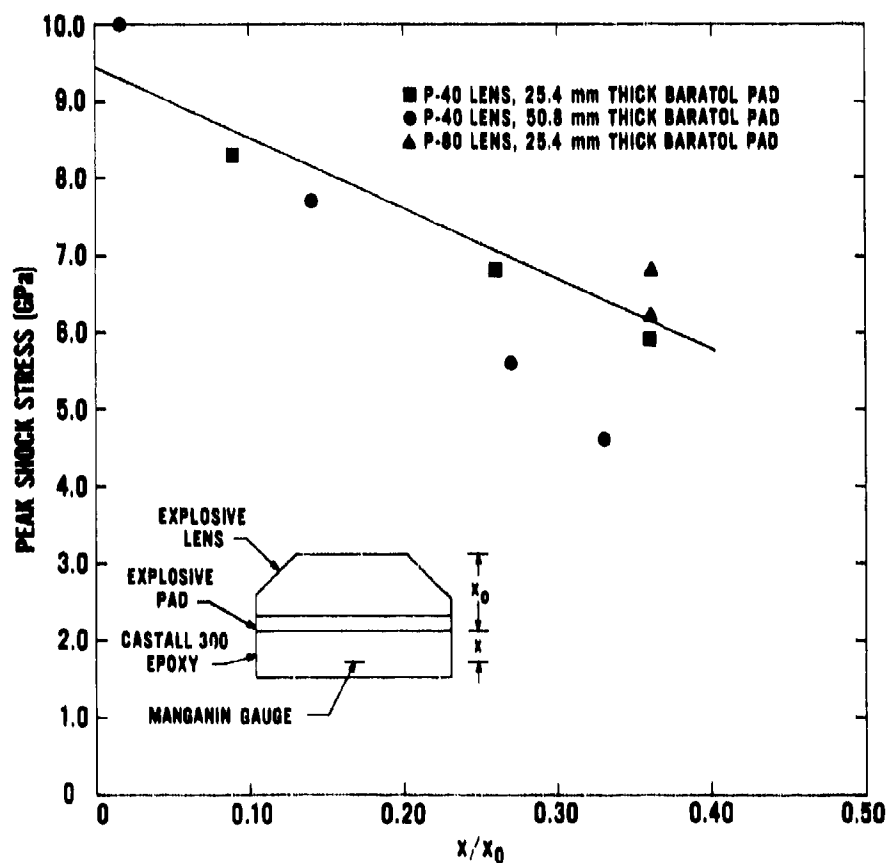


Figure 16. Peak shock stress in Castall 300 epoxy for various values of  $x/x_0$ .  $x_0$  is the sum of the explosive pad thickness and the height of the explosive plane wave lens;  $x$  is the distance into the epoxy from the explosive-epoxy interface (see inset). Data are from Table 3. The straight line is a least-squares fit, excluding the points having stress values of 4.6 and 5.8 GPa. These two points have stress values lower than the trend of the other data, probably due to the larger thickness-to-diameter ratios for the epoxy disks; relief waves from the sides of a disk could reduce the stress at the manganin gauge.

## VI. EXPLOSIVE SHOCK DEPOLING EXPERIMENTS

A series of 13 PZT 56/44 explosive shock depoling experiments was performed. These experiments includes six different PZT unit configurations; the unit capacitances ranged from 121 to 538 pF, and the load capacitances ranged from 260 to 1713 pF. The details of the PZT/epoxy experimental configurations are given in Table 4. Table 5 gives the remanent polarization, coercive field, charge available for release, capacitance, and dielectric constant data for each PZT unit.

The electrical circuits differed for some of the experiments; the circuit schematics are shown in Figure 17. In each experiment a coaxial cable (either RG-213/U or RG-220/U) was connected to the PZT unit and was part of the capacitive load. For Shots 12 through 41, the outer braid at the other end of the cable was connected to a metal box filled with transformer oil. Approximately 0.25 m of dielectric and center conductor extended inside the box, beneath surface of the oil. Aluminum spheres (25 mm diameter) were used at high-potential locations in the box to minimize corona.

In three of the experiments (Shots 38, 39, and 40) an additional load capacitor was placed in the box and connected in parallel with the capacitance of the cable. This paper/oil capacitor\* (High Energy, Inc., Type CP320/41430, 100-kV peak voltage,  $1100 \pm 5$  pF capacitance at 1 kHz, with polypropylene case dimensions of 83 x 89 x 203 mm) had an average capacitance of  $1097 \pm 15$  pF for frequencies between 100 Hz and 100 kHz after it was placed in the box. All the high-voltage components in the box were attached to a Plexiglas sheet that was hung from the lid with four nylon threaded rods.

In one of the experiments (Shot 16), two series-connected high-voltage diodes\*\* (Semtech Part No. SA5608, 250-ns recovery time, 100-kV peak inverse voltage, 1-pF capacitance, 222 mm long x 25 mm diameter) were placed in series with the high-voltage cable. This was done to determine how effectively a charged load capacitance could be isolated from the depoled PZT unit. In the shots without diodes, during and after the passage of the shock wave through the PZT units, the combination of shock and relief waves with the large generated electric fields caused the load voltage to decrease. The two diodes were contained in an oil-filled Plexiglas tube and were connected to the PZT experimental configuration by 1.2 m of RG-213/U cable. Braided tubular grounding strap was slipped over the outside of the Plexiglas tube and circumferentially soldered to the cable braid at each end of the tube to form a continuous coaxial unit. The cable dielectric extended approximately 0.25 m into each end of the tube and was sealed to the tube ends by Plexiglas bushings and epoxy. The diodes were protected from the explosive blast by slipping the Plexiglas tube inside the electrical feedthrough pipe that passed through the wall of the blast confinement chamber.

\* High Energy, Inc., Malvern Industrial Park, Malvern, PA 19355

\*\* Semtech Corporation, 1081 Bristol Road, Mountainside, NJ 07092

Table 4. PZT/epoxy experimental configuration details.

Shot Number	Number of Elements	Unit Height h <sup>a</sup> (mm)	Unit Width w <sup>a</sup> (mm)	Unit Length l <sup>a</sup> (mm)	Electroded Area (mm <sup>2</sup> )	Unit Volume (cm <sup>3</sup> )	Configuration Type <sup>d</sup>	Insulation Thickness <sup>e</sup> (mm)
12	4	12.87	12.42	12.57	156	2.01	A	3.38
15	4	12.87	12.42	12.45	155	1.99	A	3.40
16	8	51.63	49.94	24.64	1230	63.53	A	12.7
38	8	25.62	24.91	24.78	617	15.81	B	31.9
39	8	25.58	25.02	25.01	626	16.01	B	25.4
40	8	25.58	25.00	24.88	622	15.91	B	12.7
41	8	25.58	25.22	12.50	315	8.06	B	25.4
42	8	25.57	25.25	12.50	316	8.07	B	41.6
43	8	25.53	25.01	12.24	306	7.82	B	34.8
44	16 <sup>f</sup>	51.10	25.27	12.57	318	16.23	B	35.6
47	16	51.06	25.06	12.52	314	16.02	B	45.7
58	8	25.48	24.77	12.44	308	7.85	B	3.18
59	16	50.90	25.19	12.59	317	16.14	B	3.18

<sup>a</sup>Dimension normal to the shock wave propagation direction and to the planes of the electrodes; does not include thickness of the conductive epoxy between the elements.  
To calculate unit height including the epoxy layers, add 0.05 mm per layer.

<sup>b</sup>Dimension normal to the shock wave propagation direction and parallel to the planes of the electrodes.

<sup>c</sup>Dimension along the shock wave propagation direction.

<sup>d</sup>Type A used the cylindrical mold of Reference 1, except for Shot 16, which used a Plexiglas tube mold. Type B used a rectangular mold.

<sup>e</sup>Distance of PZT unit from lapped flat surface of the Castall 300 epoxy. The shock wave will propagate this distance in the epoxy before reaching the PZT unit.

<sup>f</sup>Two units of eight elements each, connected in series, positioned so that the shock front traverses both units simultaneously.

Table 5. Electrical properties of PZT units.

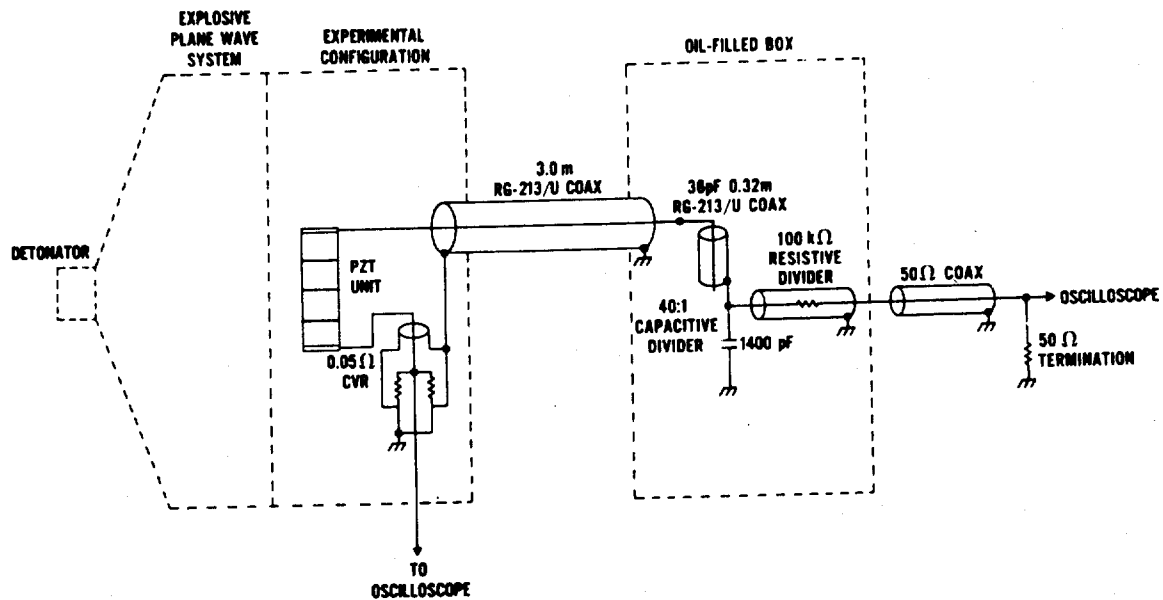
Shot Number	Remanent Polarization $P_r^a$ ( $\mu\text{C}/\text{mm}^2$ )	Low Frequency Coercive Field $E_c^a$ (kV/mm)	Charge Available for Release ( $\mu\text{C}$ )	Capacitance Before Epoxy Encapsulation <sup>b</sup> (pF)	Capacitance After Epoxy Encapsulation <sup>b</sup> (pF)	Relative Dielectric Constant $K_r$ After Epoxy Encapsulation <sup>c</sup>
12	0.33	0.86	51	263	217	2460
15	0.33	0.86	51	256	229	2420
16	0.40	0.82	489	523	482	2320
38	0.32	0.88	196	602	538	2600
39	0.32	0.89	199	614	536	2520
40	0.32	0.88	199	552	503	2400
41	0.35	0.79	110	299	244	2260
42	0.35	0.78	111	293	240	2240
43	0.35	0.78	107	276	230	2210
44	0.35	0.81	111	148	126	2320
47	0.35	0.79	110	154	121	2260
58	0.35	0.78	107	d	250	2390
59	0.34	0.90	109	156	129	2100

<sup>a</sup>These values are calculated for each unit from 60-s hysteresis loop data provided for each element by Gulton Industries, Inc., and are averages of the values for the individual elements.

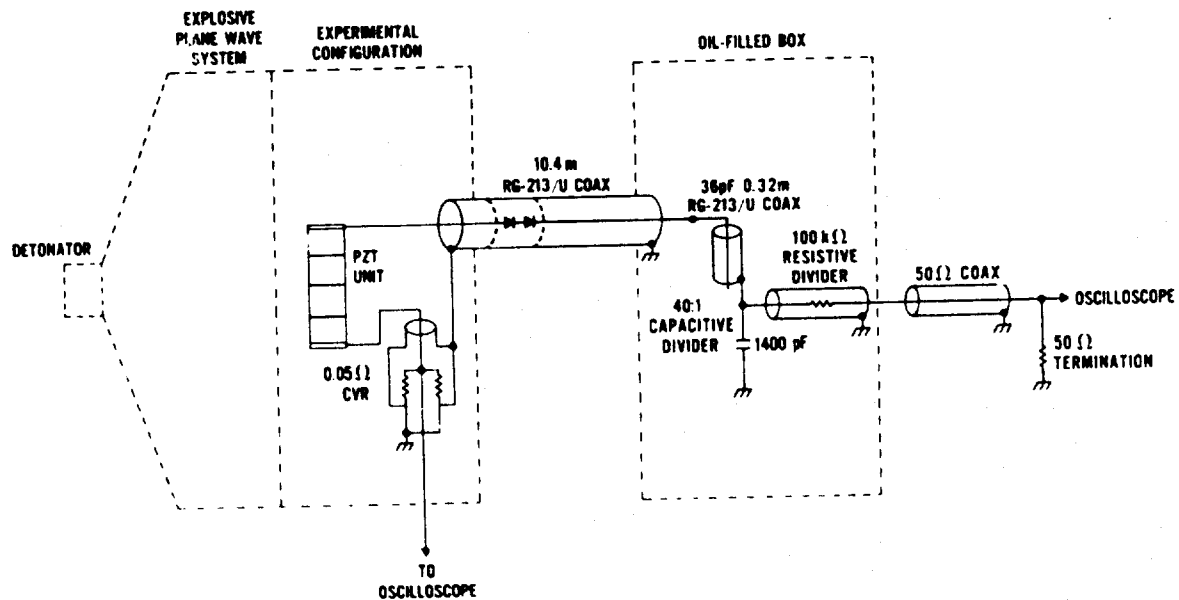
<sup>b</sup>Measured values at 1 kHz.

<sup>c</sup> $K_r$  is the low-frequency dielectric constant in the polarization direction.

<sup>d</sup>No measurement.



(a)



(b)

Figure 17. Schematics of shock depoling experiments. CVRs and voltage dividers were used for electrical pulse diagnostics. (a) Shots 12 and 15. (b) Shot 16 (note diodes). (c) Shots 38, 39, and 40. (d) Shot 41. (e) Shots 42, 43, 44, 47, 58, and 59.



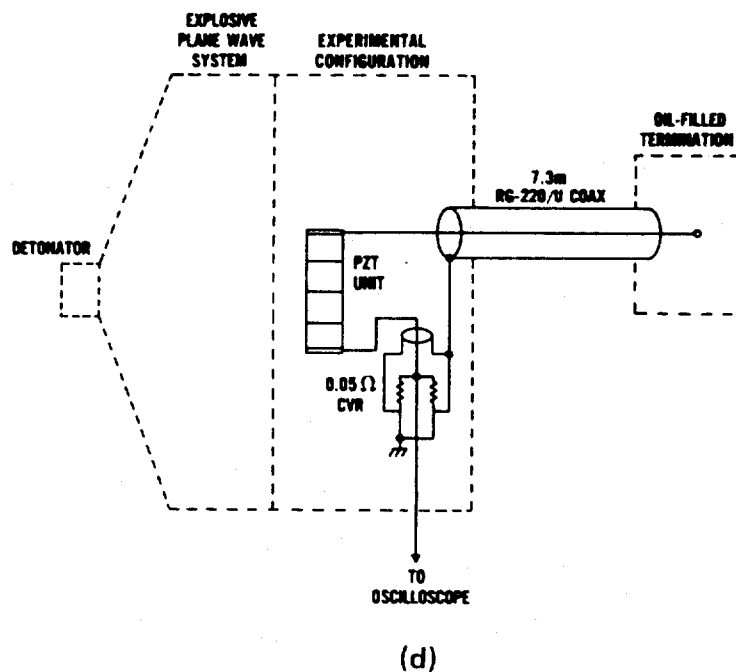
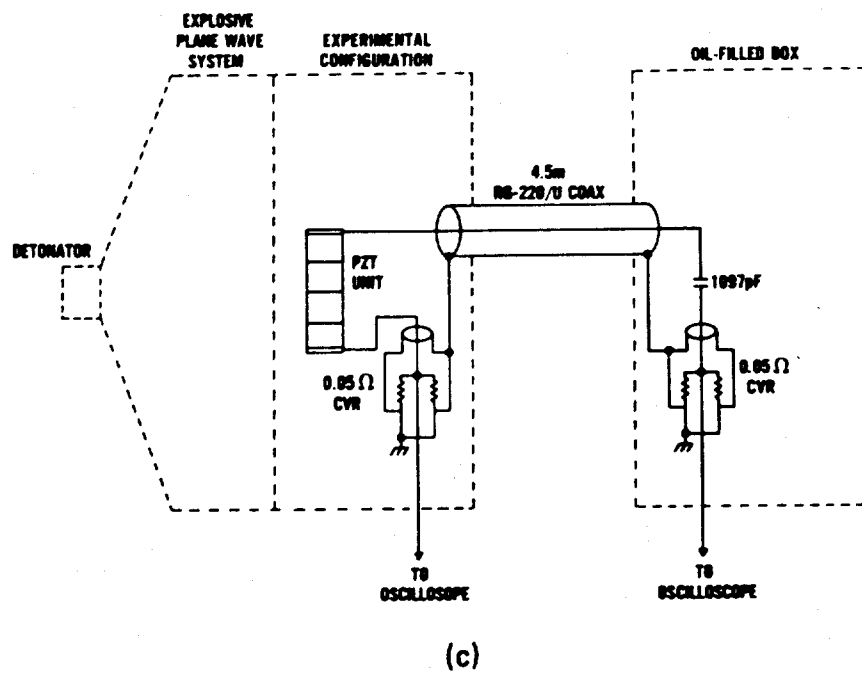
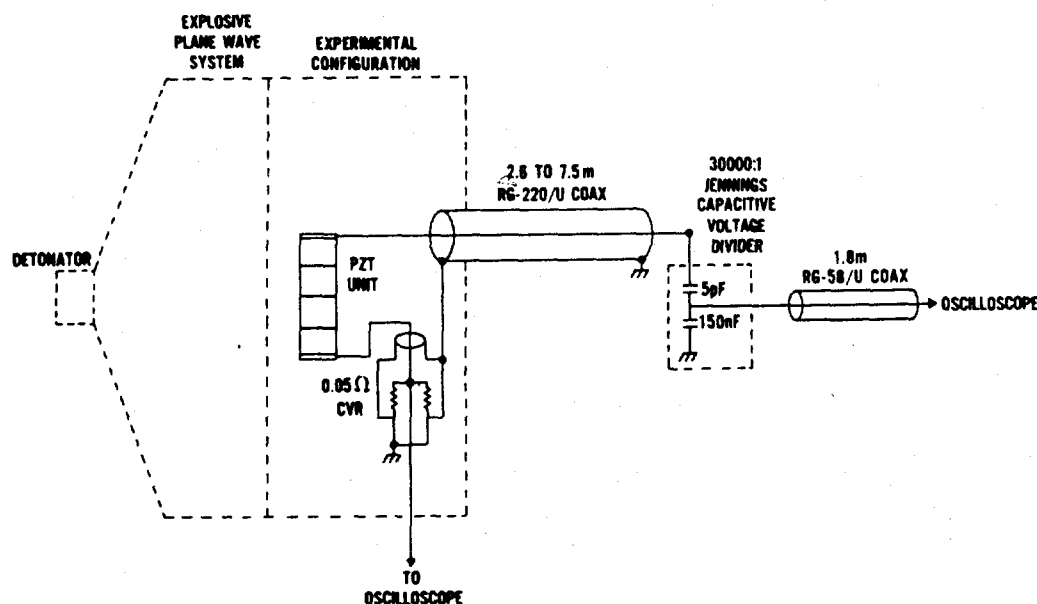


Figure 17. Schematics of shock depoling experiments. (Continued)



(e)

Figure 17. Schematics of shock depoling experiments. (Continued)

For Shots 42 through 59, the RG-220/U cable passed through the wall of the chamber and into an adjacent camera room for connection to a capacitive voltage divider.\* The combined PZT and cable capacitance was measured prior to connection of the cable to the voltage divider.

The details of the pulse diagnostics for all the shock depoling experiments are given in Table 6. The information includes the division ratios of the voltage probes and the resistance values of the coaxial current viewing resistors.

In a depoling experiment (Figure 17), the detonator initiates the plane wave lens, and the planar shock front from the lens initiates the Baratol pad. The shock front from the pad traverses first an attenuator and then the PZT unit.

The details of the explosive plane wave systems used for these experiments are given in Table 7. This table includes the plane wave lens type, the dimensions, composition, fabrication method, and density of the Baratol pads, the details of the shock attenuator, and the peak shock stress in the Castall 300 epoxy and in the PZT ceramic.

\* ITT Jennings, 970 McLaughlin Avenue, San Jose, CA 95116

Table 6. Electrical pulse diagnostics for shock depoling experiments.

Shot Number	Division Ratio of Voltage Probe	Resistance of Current Probe in Experimental Configuration <sup>a</sup> (ohms)	Resistance of Current Probe in High-Voltage Box <sup>d</sup> (ohms)
12	74200:1 <sup>a</sup>	0.05066	No Probe
15	72500:1 <sup>a</sup>	0.05000	No Probe
16	71700:1 <sup>a</sup>	0.05066	No Probe
38	No Probe	0.05015	0.04916
39	No Probe	0.05031	0.04916
40	No Probe	0.05050	0.04916
41	No Probe	0.05068	No Probe
42	30000:1 <sup>b</sup>	0.05083	No Probe
43	30000:1 <sup>b</sup>	0.05160	No Probe
44	30000:1 <sup>b</sup>	0.05106	No Probe
47	30000:1 <sup>b</sup>	0.05100	No Probe
58	30000:1 <sup>b</sup>	0.04930	No Probe
59	30000:1 <sup>b</sup>	0.05130	No Probe

<sup>a</sup> Combination capacitive and resistive divider; 35-pF input capacitance and 100-kV maximum. (The capacitance of 0.32 m of RG-213/U cable in series with a 1400-pF paper/oil capacitor, with a T&M Research Products 100-k $\Omega$ , 100-kV resistive divider on the output of the capacitive divider.) The resistive divider was calibrated by the National Bureau of Standards, Washington, D.C. The operation of the resistive divider requires a coaxial 50- $\Omega$  output cable and a 50- $\Omega$  termination at the recording oscilloscope. The circuit layout in the oil-filled box was modified between Shots 12, 15, and 16, which results in different division ratios for the combination divider.

<sup>b</sup> ITT Jennings Capacitive Divider; 5-pF input capacitance, 10-MHz bandpass, and 200-kV maximum. (Four No. JCD-605 vacuum capacitors connected in series with a No. 13200 divider.) This divider was calibrated by the ITT Jennings standards laboratory and was used at NSWC under similar minimum-stray-capacitance-to-ground conditions. The operation of this divider requires that no 50- $\Omega$  termination be used with the coaxial output cable; the output cable is to be loaded only by the oscilloscope  $\sim$ 2-M $\Omega$  input impedance.

<sup>c</sup> T&M Research Products current viewing resistor; SDN-414-05, 1000-MHz bandpass, 0.36-ns risetime, 2-J maximum energy per pulse, and 2-W continuous rating.

<sup>d</sup> T&M Research Products current viewing resistor; SBNC-1-05, 700-MHz bandpass, 0.52-ns risetime, 20-J maximum energy per pulse, and 5-W continuous rating.

Table 7. Explosive plane wave systems for shock depoling experiments.

Shot Number	Plane Wave Lens	Baratol Pad Diameter (mm)	Baratol Pad Thickness (mm)	Baratol Composition, Fabrication	Baratol Density (Mg/m <sup>3</sup> )	Shock Attenuator External to PZT-Epoxy Configuration <sup>a</sup>	Insulation Thickness <sup>b</sup> (mm)	Stress in Castall 300 <sup>c,e</sup> (GPa)	Stress in PZT <sup>d,e</sup> (GPa)
12	P-40	102	50.8	73/27 <sup>g</sup> cast	2.40	5 Plexiglass, 2 Aluminum	3.38	4.4	7.1
15	P-40	102	50.8	73/27, Cast	2.46	6 Plexiglass, 2 Aluminum	3.40	4.4	7.1
16	P-40	102	50.8	73/27, cast	2.50	5 Plexiglass, 2 Aluminum	12.7	4.3	7.0
38 <sup>f</sup>	P-80	—	—	—	—	None	31.9	7.5	12.6
39	P-40	102	50.8	76/24 <sup>h</sup> pressed	2.51	None	25.4	5.6	9.2
40	P-40	102	50.8	76/24, pressed	2.52	None	12.7	7.8	13.1
41	P-40	102	50.8	76/24, pressed	2.52	None	25.4	5.6	9.2
42	P-40	102	76.2	76/24, pressed	2.22	None	41.6	2.9	4.6
43	P-40	102	76.2	76/24, pressed	2.53	None	34.8	4.1	6.6
44	P-80	203	25.4	76/24, pressed	2.52	None	35.6	7.3	12.2
47	P-80	203	25.4	76/24, pressed	2.52	None	45.7	6.5	10.8
58	P-80	203	25.4	76/24, pressed	2.52	2 Plexiglass, 2 Copper	3.18	4.3	7.0
59	P-80	203	25.4	76/24, pressed	2.52	2 Copper, 2 Plexiglas	3.18	4.3	7.0

<sup>a</sup> Number of 6.35-mm-thick layers of attenuator materials. Material listed first is in contact with the explosive pad.

<sup>b</sup> Distance of PZT unit from lapped flat surface of the Castall 300 epoxy. The shock wave will propagate this distance in the epoxy before reaching the PZT unit.

<sup>c</sup> Stress value just before the shock wave enters the PZT material. Value includes the attenuation due to the traversal of the epoxy insulation layer.

<sup>d</sup> Stress value as shock wave first enters PZT unit.

<sup>e</sup> Estimated uncertainty for the stress values is  $\pm 0.5$  GPa.

<sup>f</sup> No Baratol pad used for this shot.

<sup>g</sup> 73% barium nitrate, 27% TNT

<sup>h</sup> 76% barium nitrate, 24% TNT

The peak shock stresses were determined from the shock properties of the explosive, attenuator materials, and PZT ceramic and from the shock stress measurements with various attenuators (Section V). Since the Hugoniot relations for the PZT 56/44 material have not been measured, Hugoniot data for PZT 52/48<sup>21</sup> (density 7.58 Mg/m<sup>3</sup>) was used in the calculations. (PZT 52/48 is a solid solution containing 52 mole percent lead zirconate and 48 mole percent lead titanate, with niobium as a minor added constituent.) The Hugoniot relations for the PZT encapsulating material have been previously determined for the stress range below 3.7 GPa.<sup>22</sup> As part of the present work, an explosive experiment was performed that provided data for this material at 12.2 GPa (Appendix C). This data agrees well with an extrapolation of the data for the lower stresses. The calculated peak shock stresses for the encapsulated PZT units ranged from 4.6 to 13.1 GPa.

Figure 18 shows a PZT experimental configuration, P-80 plane wave lens, and Baratol pad inside the blast confinement chamber. (For the experimental configuration shown in Figure 18, the RG-220/U cable was attached parallel to the lapped epoxy surface.) Figure 19 shows the Jennings high-voltage capacitive divider in the camera room adjacent to the blast confinement chamber.

## VII. SIMPLIFIED MODEL

A simplified model for the voltage and current pulses obtained from the normal-mode shock depoling of a PZT unit was presented in Reference 1 and will also be presented here for completeness. The model may be less appropriate for the somewhat triangular stress-time profiles<sup>23</sup> of explosive generated shock waves than for the more rectangular profiles of gas-gun impact generated shock waves of Reference 1, but can nevertheless be useful as a guide for interpreting the experimental results in terms of the material and circuit parameters.

A schematic of the shock depoling of a PZT unit is shown in Figure 20. The electric displacement vector, electric field, polarization vector, and permittivity are given by  $D(t)$ ,  $E(t)$ ,  $P(t)$ , and  $\epsilon$ , respectively. As the shock wave passes through the unit, the remanent polarization vector,  $P_0$ , is reduced in magnitude behind the shock front. For complete depoling,  $P_0$  is reduced to zero. The electric fields  $E_1(t)$  and  $E_2(t)$  are equal in magnitude and increase with time. The assumptions for the simplified model are as follows: (1) the wave front moves with a single steady wave velocity  $U$ , (2) all the bound surface charge is released instantaneously at the shock front (no charge release kinetics involved), (3) the permittivities  $\epsilon_1$  and  $\epsilon_2$  are equal and constant, (4) no electrical breakdown or conduction occurs in the unit, (5) the strain behind the shock front is negligible, and (6) once the PZT material comes under shock compression, it remains in that stress state (i.e., relief waves are not considered).

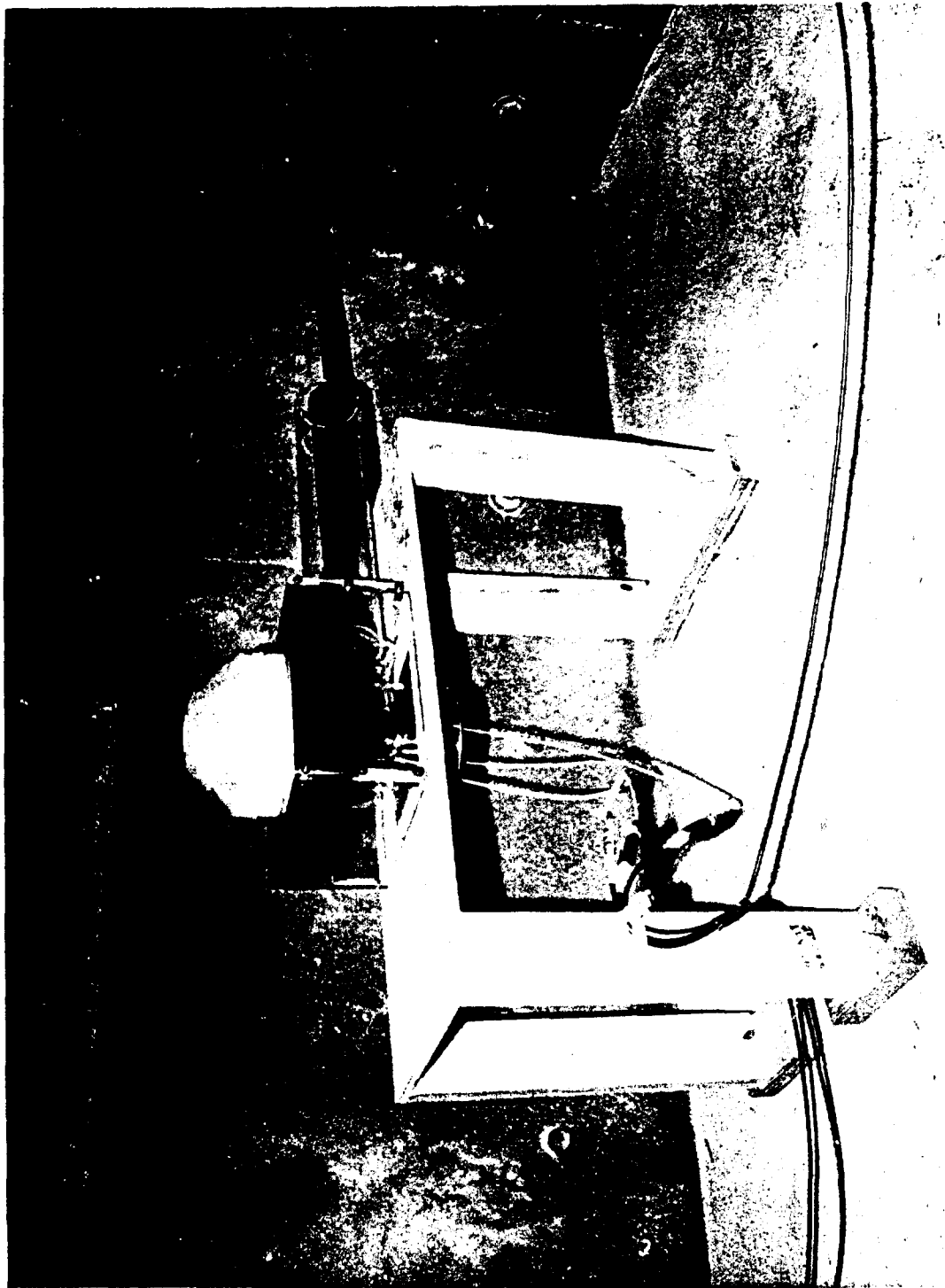


Figure 18. PZT experimental configuration with a 203-mm-diameter explosive plane wave lens and a 25.4-mm-thick Baratol explosive pad inside the blast confinement chamber, prior to the attachment of an SE-1 detonator to the top of the plane wave lens. The RG-220/U high-voltage output cable exits the chamber via a feedthrough on the right. The smaller cables (RG-188/U and RG-58/U) are for oscilloscope triggering by the spikeducers and for the CVR output.

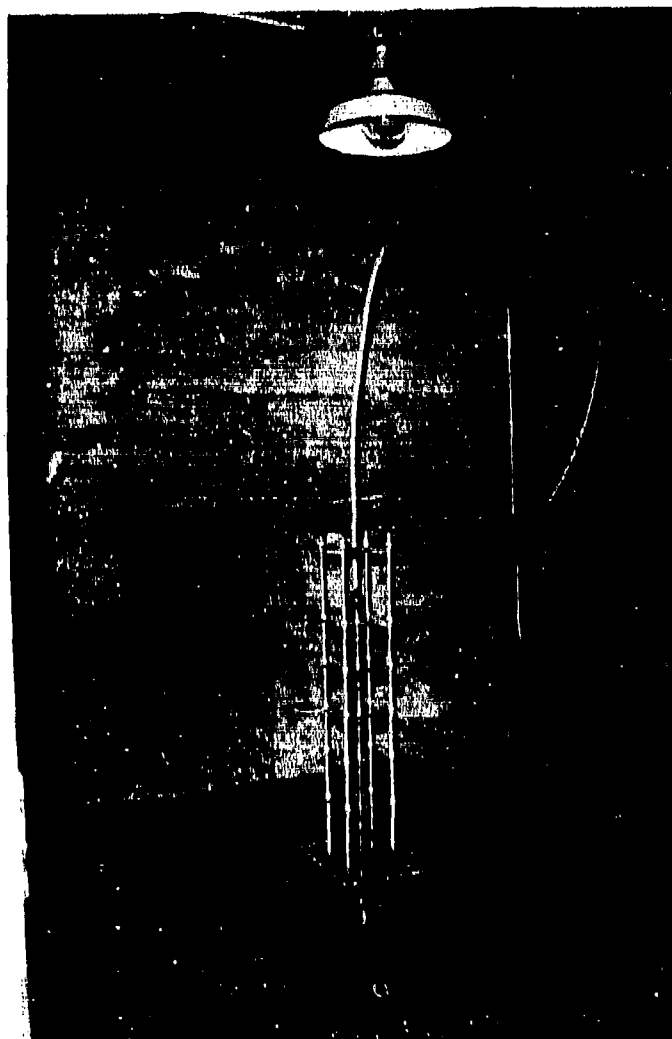


Figure 19. Jennings high-voltage capacitor divider in camera room adjacent to the blast confinement chamber. The RG-220/U high-voltage cable from the PZT experimental configuration enters the room via a feedthrough directly behind the capacitive divider. The outer conductor of the RG-220/U cable is connected via a braided strap to the large copper sheet beneath the voltage divider. The center conductor of the RG-200/U cable is connected to the corona sphere at the top of the divider; the cable is supported on strings from the ceiling. The smaller RG-58/U cable from the base of the divider is connected directly (no 50- $\Omega$  termination resistance) to the input of an oscilloscope out-of-view at the left. The square frame of the camera port (not used in these experiments) is seen behind the voltage divider.

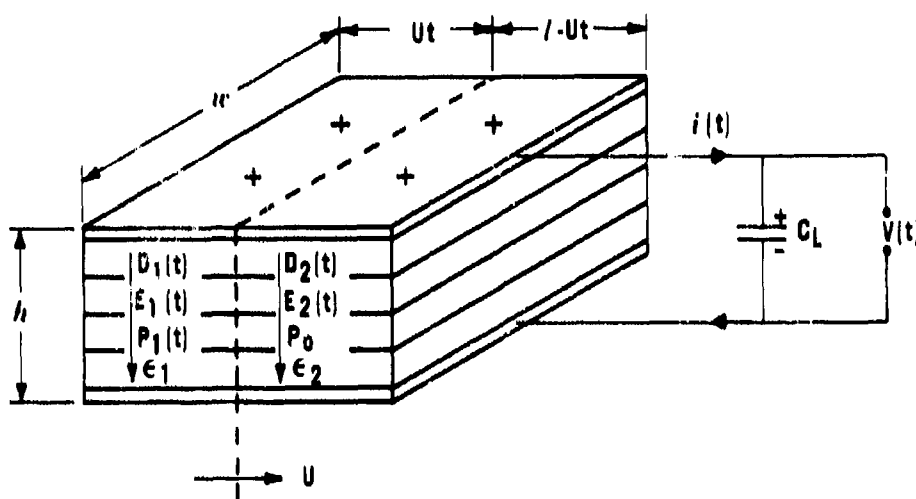


Figure 20. Schematic of the normal-voltage mode depoling of a PZT unit with a capacitive load.  $U$  is the shock velocity. At time  $t$ , the shock front is indicated by the dashed line. Regions 1 and 2 are behind and in front of the shock front, respectively. As the shock wave passes through and depoles the unit, bound surface charge behind the shock front is released. This released charge is distributed between the PZT unit and load capacitance  $C_L$ , charging them to a voltage  $V(t)$ .

At time,  $t$ , as the shock wave propagates through the PZT unit, the capacitances behind and ahead of the shock front are given, respectively, by

$$C_1(t) = \frac{wUt}{h} \epsilon, 0 \leq t \leq \tau \quad (6)$$

and

$$C_2(t) = \frac{w(l - Ut)}{h} \epsilon, 0 \leq t \leq \tau \quad (7)$$

where  $\tau = l/U$  is the shock transit time through the PZT unit and  $\epsilon = \epsilon_1 = \epsilon_2$ . The equivalent capacitance of the PZT unit is constant and given by

$$C = C_1(t) + C_2(t) = \frac{A}{h} \epsilon, t \geq 0 \quad (8)$$

where  $A = lw$ . The charge conservation equation is

$$Q(t) = q(t) + q_L(t), t \geq 0 \quad (9)$$

where  $Q(t)$  is the total charge released by the shock wave and  $q(t)$  and  $q_L(t)$  are the charges distributed on the source and load capacitances, respectively.



The voltage balance equation is

$$\frac{q(t)}{C} = \frac{q_L(t)}{C_L}, t \geq 0 \quad (10)$$

From Equations (9) and (10),

$$q(t) = \frac{C}{C+C_L} Q(t), t \geq 0 \quad (11)$$

and

$$q_L(t) = \frac{C_L}{C+C_L} Q(t), t \geq 0 \quad (12)$$

where  $C + C_L$  is the total circuit capacitance. The voltage on the PZT unit and load capacitance is then given by

$$V(t) = \frac{Q(t)}{C+C_L}, t \geq 0 \quad (13)$$

The current flowing to the load capacitor is

$$I(t) = \frac{dq_L(t)}{dt} = \frac{C_L}{C+C_L} \frac{dQ(t)}{dt}, t \geq 0 \quad (14)$$

The released charge is

$$Q(t) = \begin{cases} P_0 A \frac{t}{\tau}, & 0 \leq t \leq \tau, \\ P_0 A, & t > \tau \end{cases} \quad (15)$$

The equations for  $V(t)$  and  $I(t)$  then become, respectively,

$$V(t) = \begin{cases} \frac{P_0 A}{C+C_L} \frac{t}{\tau}, & 0 \leq t \leq \tau, \\ \frac{P_0 A}{C+C_L}, & t > \tau \end{cases} \quad (16)$$

and

$$I(t) = \begin{cases} \frac{C_L}{C+C_L} \frac{P_0 A}{\tau}, & 0 \leq t \leq \tau, \\ 0, & t > \tau \end{cases} \quad (17)$$

These equations are plotted in Figure 21(a). This type of response for a PZT unit will be called ideal.

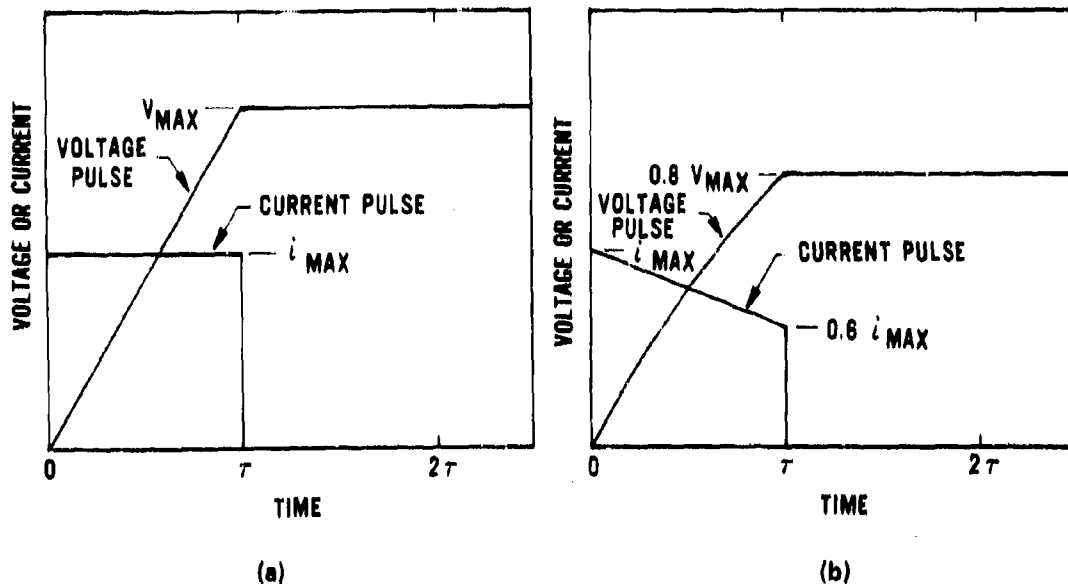


Figure 21. Schematic of voltage and current pulses for the normal mode depoling of a PZT unit. (a) Pulses for the ideal response of a PZT unit. The voltage pulse increased linearly to a maximum value of  $V_{max} = (P_0 A)/(C + C_L)$ . The current pulse has a constant maximum value of  $I_{max} = (C_L/(C + C_L)) (P_0 A/\tau)$  during shock transit time  $\tau$ . (b) Pulses for the nonideal response of a PZT unit. For  $\alpha = 0.2 P_0/\tau$ , the voltage pulse increases in a non-linear manner to a maximum value of  $0.8 V_{max}$ . The current pulse decreases linearly from  $I_{max}$  to  $0.6 I_{max}$  during shock transit time.

In the work of Reference 1, it was found that the shock compression of PZT 95/5 ferroelectric ceramic (a solid solution of 95 mole percent lead zirconate and 5 mole percent lead titanate, with niobium as a minor added constituent) with a capacitive load showed this ideal type of response. For the PZT 56/44 experiments of Reference 1 and for the present work, the units did not respond in an ideal manner, since the charge flowing from the units decreased in time as the shock wave propagated through them. Although the reason for the decreased charge release probably depends in a complicated manner on the shock conditions and the PZT material properties, this behavior can be represented in simple terms by the expression

$$Q(t) = \begin{cases} P_0 A \frac{t}{\tau} \left(1 - \frac{\alpha t}{P_0}\right), & 0 \leq t \leq \tau, \\ P_0 A \left(1 - \frac{\alpha \tau}{P_0}\right), & t > \tau \end{cases} \quad (18)$$

Here we have made the assumption of a linear decrease in the charge release. The constant parameter  $\alpha$  has the dimensions (charge area<sup>-1</sup> time<sup>-1</sup>). For shots in which depoling is initially incomplete,  $P_0$  could be replaced by a smaller value.

Substituting Equation (18) into Equations (13) and (14) gives, respectively,

$$V(t) = \begin{cases} \frac{P_0 A}{C + C_L} \frac{t}{\tau} \left(1 - \frac{\alpha t}{P_0}\right), & 0 \leq t \leq \tau, \\ \frac{P_0 A}{C + C_L} \left(1 - \frac{\alpha \tau}{P_0}\right), & t > \tau \end{cases} \quad (19)$$

and

$$i(t) = \begin{cases} \frac{C_L}{C + C_L} \frac{P_0 A}{\tau} \left(1 - 2 \frac{\alpha t}{P_0}\right), & 0 \leq t \leq \tau, \\ 0, & t > \tau \end{cases} \quad (20)$$

These equations are plotted in Figure 21(b) for a representative  $\alpha$  of  $0.2 (P_0/\tau)$ . For this value of  $\alpha$ ,  $Q(\tau) = 0.8 P_0 A$ ; i.e., the charge release is 80 percent. Note that the slopes of the voltage pulses for the ideal and nonideal responses are equal at  $t = 0$ . The value  $\alpha$  can be determined from the decrease in the current pulse amplitude with the equation

$$\alpha = \frac{P_0}{2\tau} \left( \frac{i_{\max} - i(\tau)}{i_{\max}} \right) \quad (21)$$

where  $i(\tau)$  is the value of the current at  $t = \tau$ .

The equations for the charge release, voltage, and current that have been derived for the ideal and nonideal responses of PZT units depend on the ratio of the load to source capacitances,  $C_L/C$ . Appendix A contains a discussion of these equations as a function of this ratio for the ideal response of a PZT unit.

## VIII. RESULTS AND DISCUSSION

Table 8 is a summary of the data for the 13 shock depoling experiments. The range of the maximum voltages was from 36 to 95 kV, and the range of the maximum currents was from 10.5 to 48.0 A. The maximum load energies ranged from 0.13 to 2.48 J, and the average power transferred to the load ranged from 0.17 to 1.24 MW.

Voltage and current pulses for the depoling experiments are shown in Figures 22 through 34; the current pulse in each of these figures is from the CVR in the PZT/epoxy experimental configuration. This CVR measures the total circuit current external to the PZT unit, which includes the charge transferred to the coaxial cable and, where appropriate, to a lumped load capacitor or voltage divider. Appendix B contains the oscilloscope records from which these pulses were obtained. The high-frequency oscillations that occurred on the initial part of some of the current and voltage pulses were removed by averaging the amplitude of these oscillations during the pulse digitization procedure. The transit time for the depoling stress wave in each experiment was estimated from the shape of the voltage and/or current pulses. The resulting depoling wave velocities ranged from 3.8 to 4.8 km/s, with an average value of 4.4 km/s.

Electrical breakdown or conduction (in either the PZT unit or the external circuit) occurred in all the shots, as evidenced by the shapes of the current and voltage pulses. Three types of breakdown or conduction were observed; these will be discussed in terms of the shapes of the current pulses.

The first type is characterized by a smooth decrease in the amplitude of the current (with increasing negative slope) from its maximum value near  $t = 0$  until the amplitude became zero at a time much less than the anticipated shock transit time for the PZT unit. The current then becomes more negative, followed by a return to near zero values, with one or more smaller negative excursions before approaching zero in an approximately asymptotic manner. This type of breakdown behavior may be due to localized or bulk conduction in the PZT material, caused by the combined effects of the shock stress and the high electric field from the released charge. This conduction has the effect of a decreasing charge release from the unit with increasing time. This conduction behavior was observed in Shots 12, 15, 38, 40, 41, 43, 44, and 47 and may also have occurred in Shot 39. (The ratios of the duration of the initial positive portion of the current pulse to the shock transit time for these shots ranged from about 0.3 to 0.7.)

The current pulses for Shot 40 (13.1 GPa stress) showed a positive current recovery region between about  $3.1 \mu\text{s}$  and the shock transit time of  $5.2 \mu\text{s}$ . The maximum current in this region was about 4.2 A for CVR 1. Similar recovery behavior was observed at 11.8 GPa in the gas-gun impact depoling experiments; the peaks of the recovery voltage and current pulses also occurred near the shock transit time.<sup>1</sup>

The second type of breakdown or conduction behavior was observed in Shot 42. The current amplitude decreased in an approximately linear manner from its maximum value until a time corresponding to the shock transit time anticipated from the data of Reference 21, then decreased more

Table 8. Data summary for shock depoling experiments.

Shot Number	Charge Available for Release (μC)	Calculated Peak Input Stress for PZT Unit <sup>a</sup> (GPa)	Load Capacitance <sup>b</sup> (pF)	Maximum Load Voltage (kV)	Time to Maximum Voltage (μs)	Maximum Electric Field in PZT Unit <sup>c</sup> (kV/mm)	Transit Time for Depoling Stress Wave <sup>d</sup> (μs)	Velocity of Depoling Stress Wave <sup>e</sup> (km/s)	Strain Due to Depoling Stress Wave <sup>f</sup> (μm/m)	Initial Slope of Voltage Pulse (kV/μs)	Maximum Current (A)	Current Pulse Duration <sup>g</sup> (μs)	Charge Released to Load <sup>h</sup> (μC)	Maximum Load Energy <sup>i</sup> (J)	Maximum Load Energy Density <sup>j</sup> (J/cm <sup>3</sup> )	Average Power Transferred to Load (MW)
12	51	7.1	360	36	1.4	2.8	2.9	4.4	0.014	34	10.5	1.4	14	0.23	0.11	0.17
15	51	7.1	360	47	1.7	3.7	3.0	4.2	0.014	32	11.3	1.4	15	0.40	0.20	0.23
16	489	7.0	1073	68	2.0	1.3	5.2	4.7	0.013	39	48.0	6.4	88	2.48	0.039	1.24
38	196	12.6	1550	(13)	—	(0.51)	5.2	4.8	0.013	—	20.0	1.5	20	(0.13)	(0.082)	(0.09)
39	199	9.2	1601	(34)	—	(1.3)	5.4	4.6	0.013	—	29.5	3.0	34	(0.91)	(0.057)	(0.30)
40	199	13.1	1713	(14)	—	(0.55)	5.2	4.8	0.013	—	25.0	1.5	24	(0.17)	(0.011)	(0.11)
41	110	9.2	742	(59)	—	(2.3)	3.1	4.0	0.015	—	32.7	1.8	44	(1.30)	(0.16)	(0.74)
42	111	4.6	760	63	2.8	2.5	2.7	4.6	0.013	32	29.0	3.2	48	1.50	0.19	0.34
43	107	6.6	761	69	2.3	2.7	3.2	3.8	0.016	33	28.0 <sup>k</sup>	3.3 <sup>k</sup>	52 <sup>k</sup>	1.80	0.23	0.76
44	111	12.2	380	60	1.1	1.2	2.7	4.7	0.013	75	32.1	1.2	29	0.48	0.042	0.62
47	110	10.8	389	69	1.1	1.4	2.8	4.5	0.013	75	—	1.2	27 <sup>m</sup>	0.93	0.058	0.85
58 <sup>n</sup>	107	7.0	260	50	1.7	2.0	3.0	4.3	0.014	30	11.0	4.6	17	0.33	0.042	0.19
59 <sup>o</sup>	109	7.0	395	(95)	—	(1.9)	3.1	4.1	0.015	—	36.3	4.0	38	(1.78)	(0.11)	(0.45)

<sup>a</sup> Stress calculation is based on Hugoniot data for PZT 52/48 and for Castall 300 epoxy (Reference 22), along with shock attenuation data for Castall 300. Estimated uncertainty for the stress values is ±0.5 GPa. Strain calculation is based on the ratio of the elastic wave particle velocity for PZT 52/48 to the velocity of the depoling stress wave.

<sup>b</sup> Includes the capacitance of the high-voltage cable and of the voltage probe if used.

<sup>c</sup> If electrical breakdown occurred, the value shown is the maximum positive value prior to breakdown.

<sup>d</sup> Estimated from the shape of either the voltage or current pulse.

<sup>e</sup> Time at which the amplitude of the initial positive portion of the current pulse became zero. For Shots 16, 43, 58, and 59, an abrupt positive excursion of the current pulse occurred prior to this time (at 2.6, 2.3, 1.7, and 1.2 μs, respectively) indicating electrical breakdown external to the PZT unit.

<sup>f</sup> Determined by integrating the initial positive portion of the current pulse from the CVR in the PZT epoxy experimental configuration.

<sup>g</sup> Calculated from  $0.5 C_L V^2$ , where  $C_L$  is the load capacitance and  $V$  is the maximum load voltage.

<sup>h</sup> Maximum load energy per cm<sup>3</sup> of PZT material.

<sup>i</sup> Calculated by dividing the maximum load energy by the time to the maximum of the voltage pulse, if no voltage pulse is available, the time is the duration of the initial positive portion of the current pulse.

<sup>j</sup> Pulse diagnostics for these shots were based on CVR's, with no voltage probes. Values shown in parentheses are calculated via current pulse data.

<sup>k</sup> Value determined from oscilloscope record; the actual value may be larger than indicated because possible late triggering of the oscilloscope may not have revealed the entire current pulse.

<sup>l</sup> CVR oscilloscope record did not show most of the initial positive portion of the current pulse.

<sup>m</sup> Calculated from the maximum voltage.

<sup>n</sup> PZT was subjected to two stress pulses: first from a detonator that did not detonate (only fractured) the explosive plane wave lens and Baratol pad, and then from the complete detonation of the replacement explosive system.

<sup>o</sup> Voltage probe oscilloscope record for this shot did not show data. Values in parentheses are calculated via current pulse data. Noise pulses on the CVR oscilloscope record obscured portions of the current pulse so that the maximum current value is uncertain. The value was taken to be 36 A.

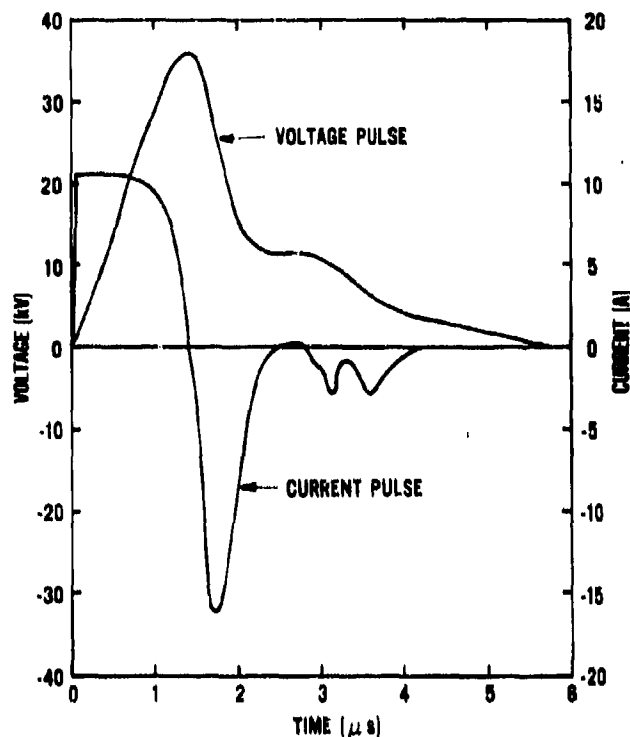


Figure 22. Voltage and current pulses for Shot 12. The PZT and load capacitances were 217 pF and 380 pF, respectively. The input shock stress to the PZT unit was 7.1 GPa. The transit time for the depoling stress wave was taken to be 2.9  $\mu$ s near the beginning of a significant decrease from the plateau that followed the main portion of the voltage pulse. The maxima were 36 kV and 10.5 A.

rapidly to zero with only a small negative excursion. This was the only shot for which the current and voltage pulses had shapes approximating those of Figure 21(b) and for which the durations of the initial positive portions of the current and voltage pulses corresponded approximately to the anticipated shock transit time. The value of the parameter  $\alpha$  was determined from Equation (21) to be  $0.3(P_0/\tau)$ . For this value of  $\alpha$ , the predicted charge release  $Q(\tau)$  is  $0.7 P_0 A$ , or 70 percent of the available charge. The measured charge release was  $0.57 P_0 A$ , or 57 percent of the available charge.

The third type of electrical breakdown or conduction behavior was observed in Shots 16, 43, 58, and 59 and was characterized by an abrupt increase in the current amplitude to a higher positive value. This behavior is indicative of localized breakdown in the circuit external to the PZT unit, probably at the coaxial cable terminations.

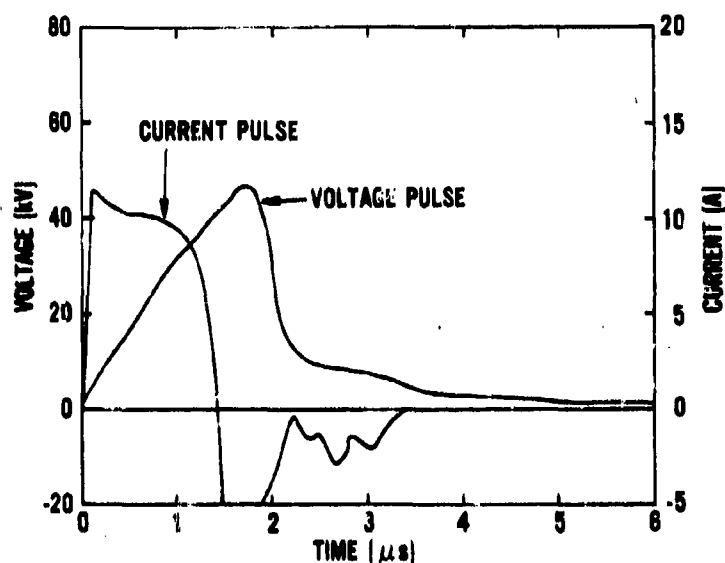


Figure 23. Voltage and current pulses for Shot 15. The PZT and load capacitances were 229 pF and 380 pF, respectively. The input shock stress to the PZT unit was 7.1 GPa. The transit time for depoling stress wave was taken to be 3.0  $\mu$ s near the beginning of a significant decrease from the plateau that followed the main portion of the voltage pulse. The maxima were 47 kV and 11.3 A.

In Shot 58, when the SE-1 detonator was fired, detonation did not occur in the P-80 explosive lens or in the Baratol pad. The lens and pad were fragmented, but not burned. There was no visible damage to the PZT/epoxy configuration. After the explosive material debris was removed from the blast chamber, another SE-1 detonator, P-80 lens, and Baratol pad were placed in contact with the PZT/epoxy configuration. The initiation circuits were rechecked and the shot was fired again. The shape of the resulting current pulse for this shot (prior to breakdown at 1.7  $\mu$ s) is similar to that for the depoling of an ideal PZT unit [Figure 21(a)]; however, the maximum current was 11.0 A instead of the 18.2 A that would be expected for ideal response. This behavior may be a result of partial depoling of the PZT unit by the stress wave from the detonator alone.

This stress wave may also have caused unseen fracturing of the Castall 300 epoxy or PZT or debonding of the epoxy in the region of the PZT or the coaxial cable terminations, which could lead to the electrical breakdown observed between 1.7 and 2.9  $\mu$ s.

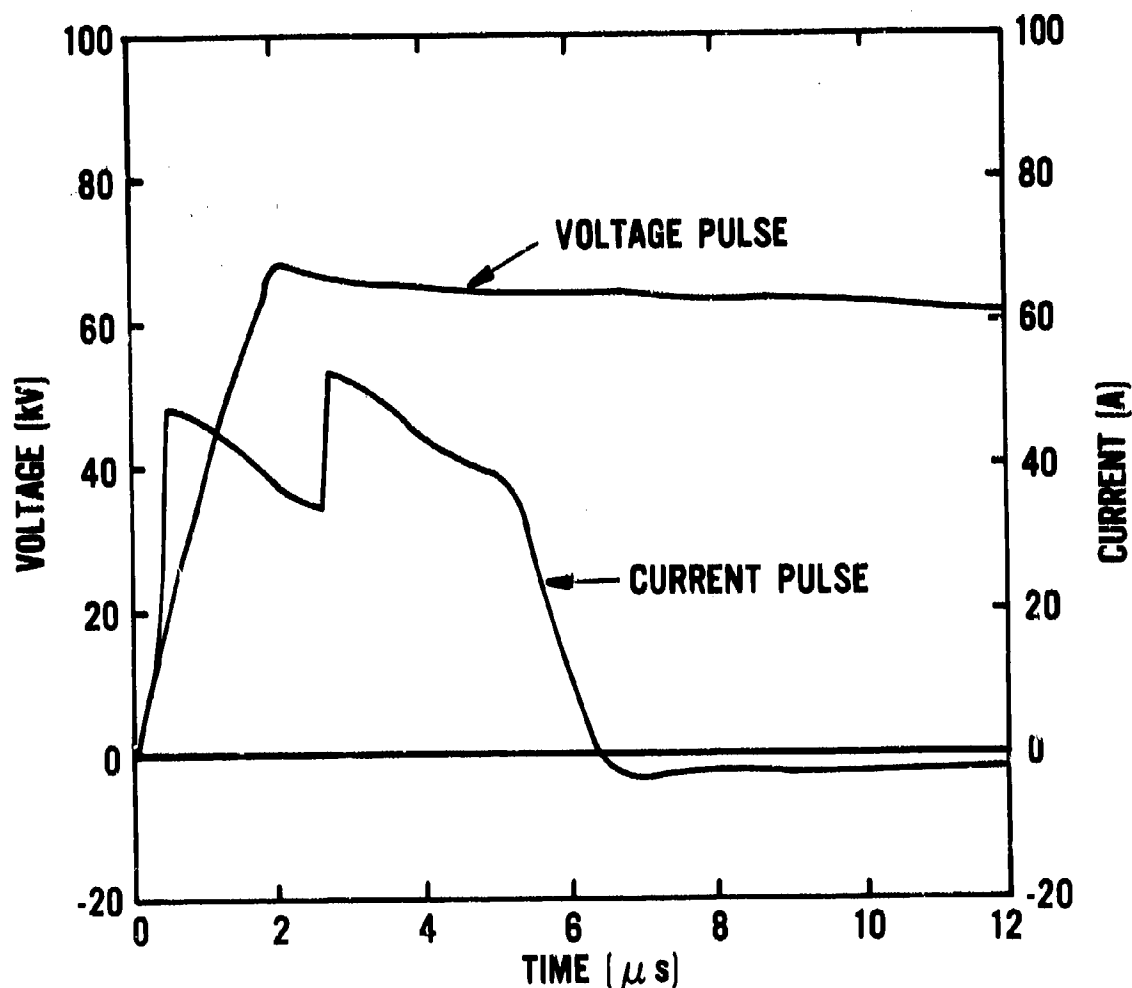


Figure 24. Voltage and current pulses for Shot 16. The PZT and load capacitances were 482 pF and 1073 pF, respectively. The input shock stress to the PZT unit was 7.0 GPa. The transit time for the depoling stress wave was taken to be 5.2  $\mu$ s near a significant change in the rate of decrease of the current. Electrical breakdown external to the PZT unit was evident from the abrupt increase in the current at 2.6  $\mu$ s. The diodes in the circuit prevented an accompanying abrupt decrease in the voltage. The maximum voltage was 68 kV, and the maximum current prior to breakdown was 48 A.



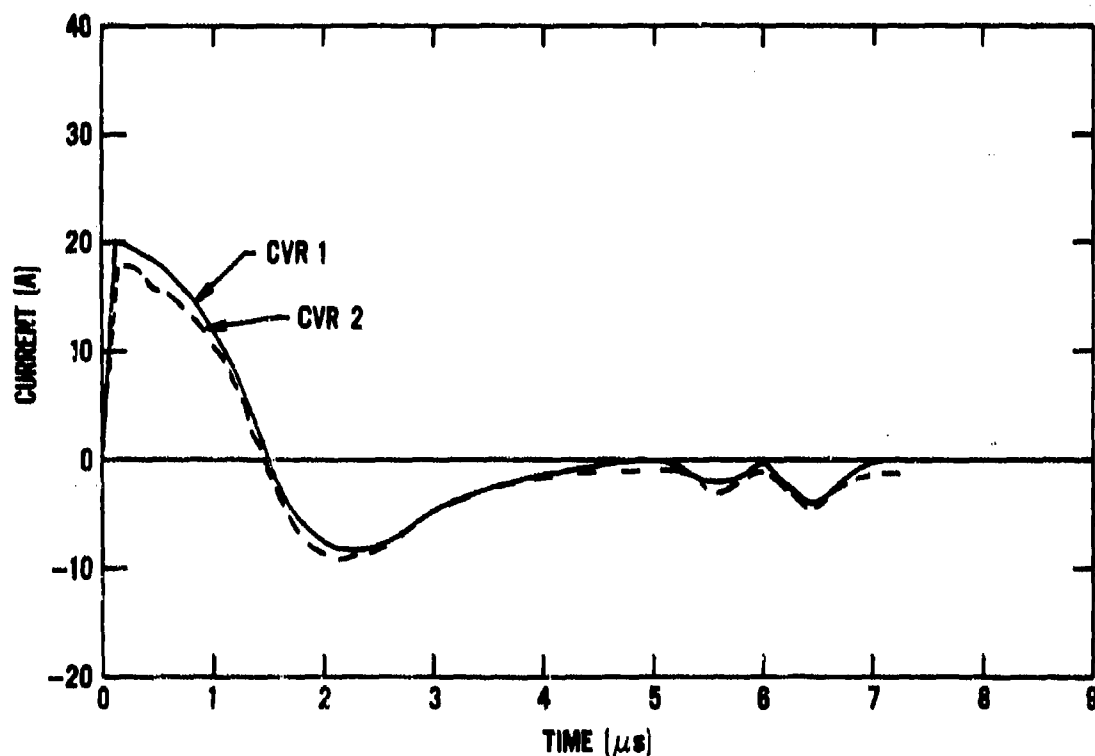


Figure 25. Current pulses for Shot 38. The PZT and load capacitances were 538 pF and 1550 pF, respectively. CVR1 was in the PZT/epoxy experimental configuration. CVR2 was in the oil-filled box and measured only the current to the 1097 pF capacitor. The input shock stress to the PZT unit was 12.6 GPa. The transit time for the depoling stress wave was taken to be 5.2  $\mu\text{s}$  near the beginning of the second negative increase of the CVR1 pulse. The maximum currents for CVR1 and CVR2 were 20.0 A and 18.0 A, respectively.

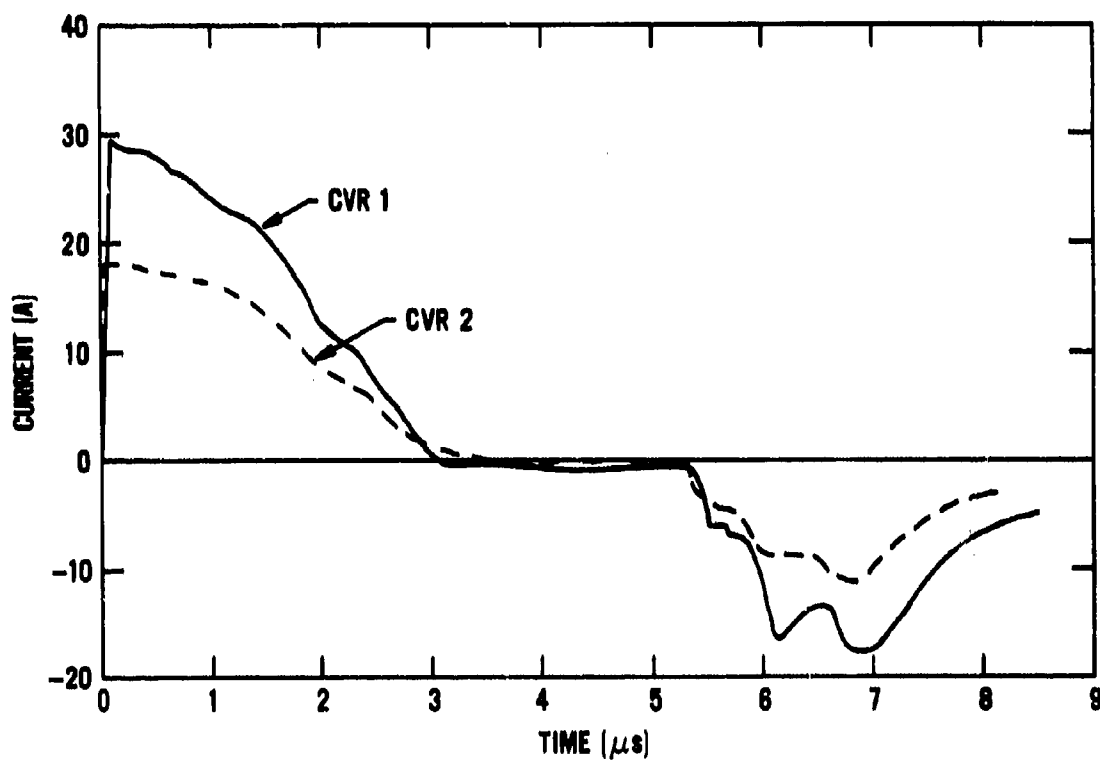


Figure 28. Current pulses for Shot 39. The PZT and load capacitances were 536 pF and 1601 pF, respectively. CVR1 was in the PZT/epoxy experimental configuration. CVR2 was in the oil-filled box and measured only the current to the 1097 pF capacitor. The input shock stress to the PZT unit was 9.2 GPa. The transit time for the depoling stress wave was taken to be 5.4  $\mu$ s near the beginning of the negative increase of the CVR1 pulse. The maximum currents for CVR1 and CVR2 were 29.5 A and 18.1 A, respectively.

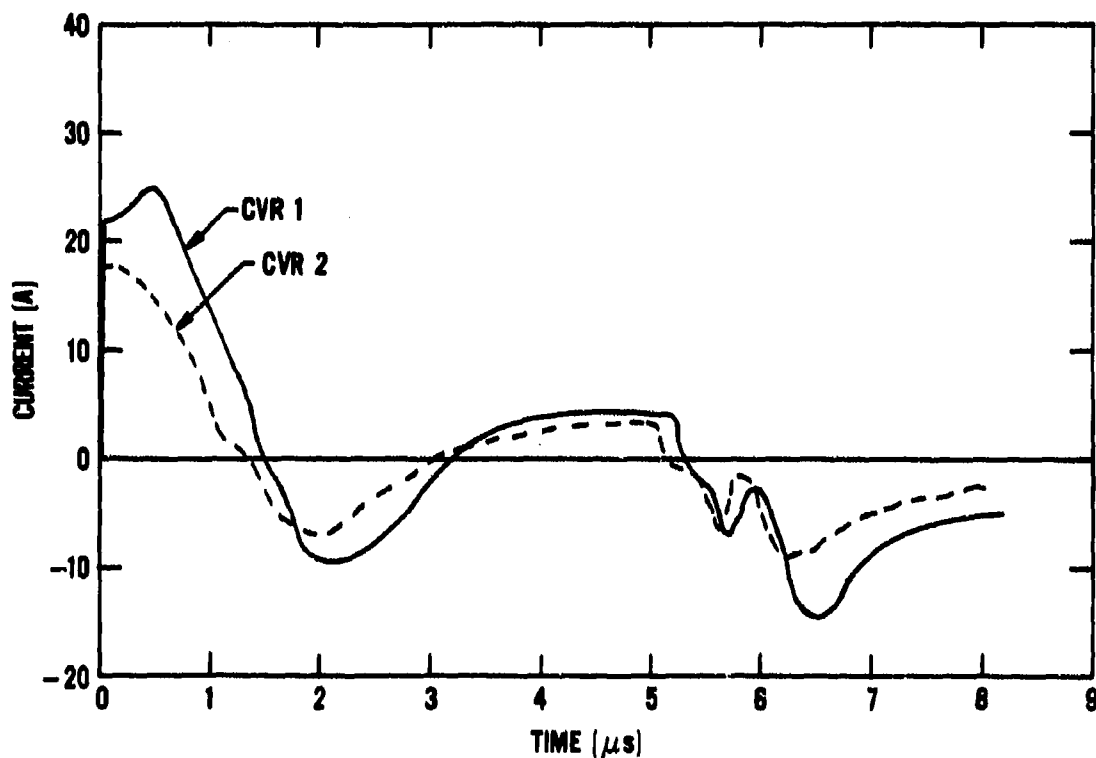


Figure 27. Current pulses for Shot 40. The PZT and load capacitances were 503 pF and 1713 pF, respectively. CVR1 was in the PZT/epoxy experimental configuration. CVR2 was in the oil-filled box and measured only the current to the 1097 pF capacitor. The input shock stress was 13.1 GPa. The transit time for the depoling stress wave was taken to be 5.2  $\mu$ s near the beginning of the second negative-going portion of the CVR1 pulse. The maximum currents for CVR1 and CVR2 were 25.0 A and 17.8 A, respectively.

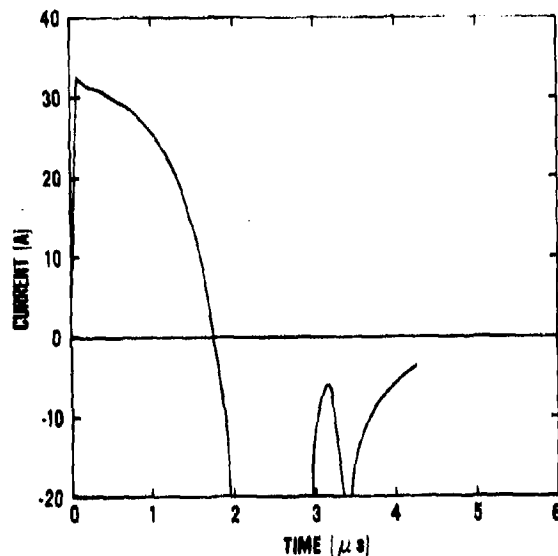


Figure 28. Current pulse for Shot 41. The PZT and load capacitances were 244 pF and 742 pF, respectively. The input shock stress to the PZT unit was 9.2 GPa. The transit time for the depoling stress wave was taken to be 3.1  $\mu$ s near the beginning of the second negative increase of the pulse. The maximum current was 32.7 A.

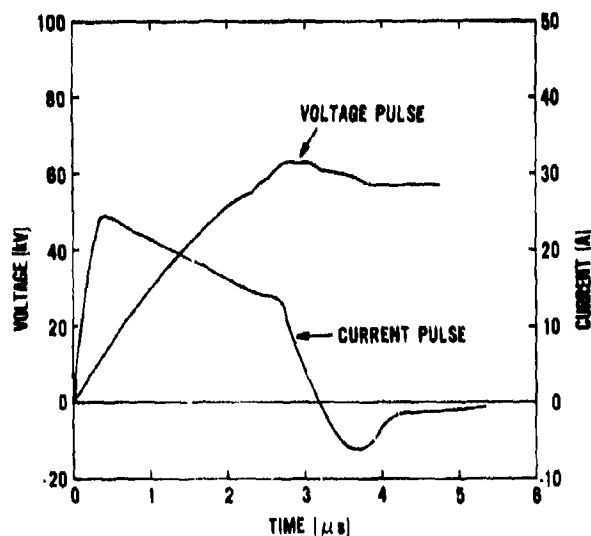


Figure 29. Voltage and current pulses for Shot 42. The PZT and load capacitances were 240 pF and 780 pF, respectively. The input shock stress to the PZT unit was 4.6 GPa. The transit time for the depoling stress wave was taken to be 2.7  $\mu$ s near a significant change in the rate of decrease of the current. The maxima were 63 kV and 29.0 A.

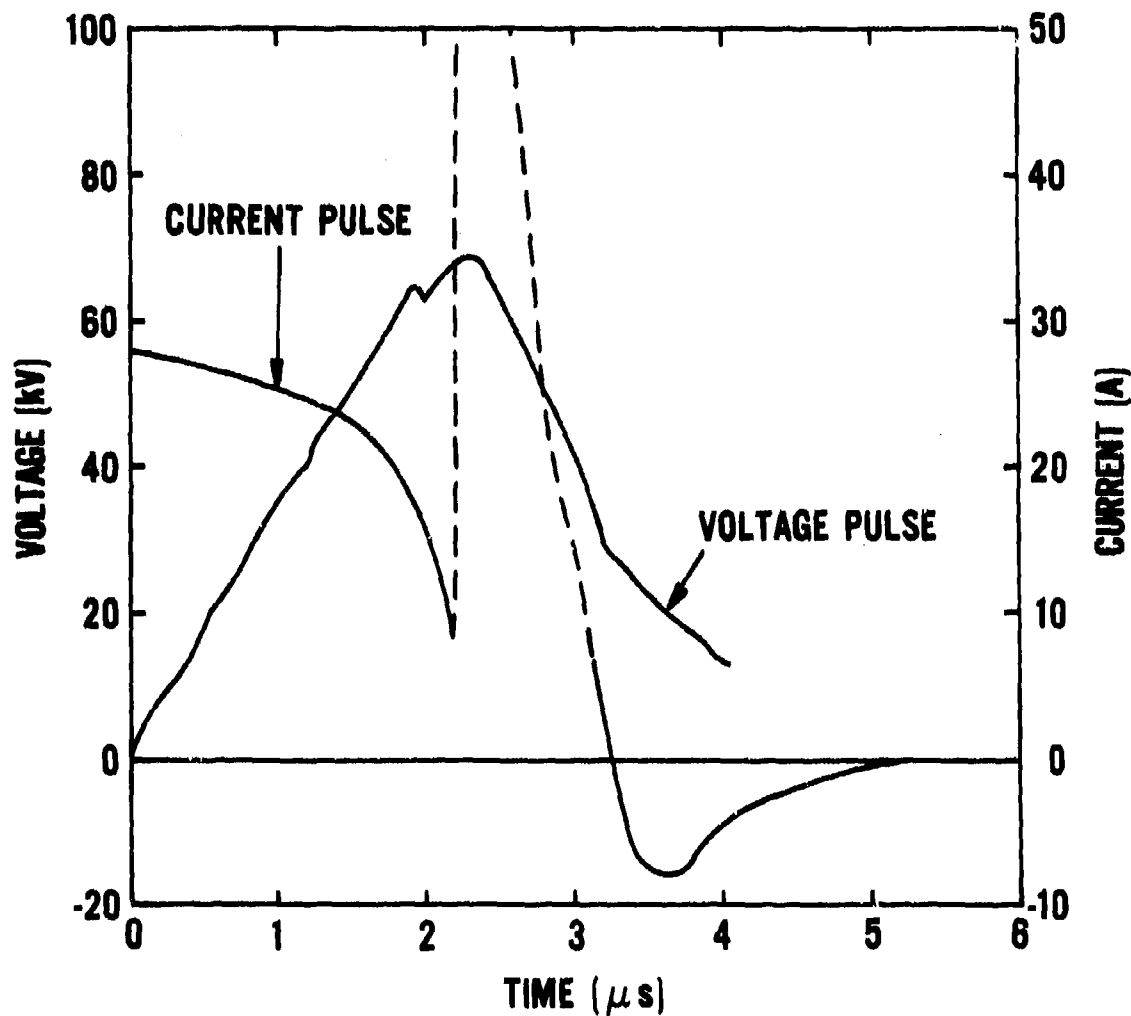


Figure 30. Voltage and current pulses for Shot 43. The PZT and load capacitances were 230 pF and 781 pF, respectively. The input shock stress to the PZT unit was 6.6 GPa. The transit time for the depoling stress wave was taken to be 3.2 μs at the beginning of the negative portion of the current pulse. Electrical breakdown external to the PZT unit was evident between 2.2 μs and 3.1 μs from the abrupt changes in the current. The maximum voltage was 69 kV, and the maximum current prior to breakdown was 28.0 A.

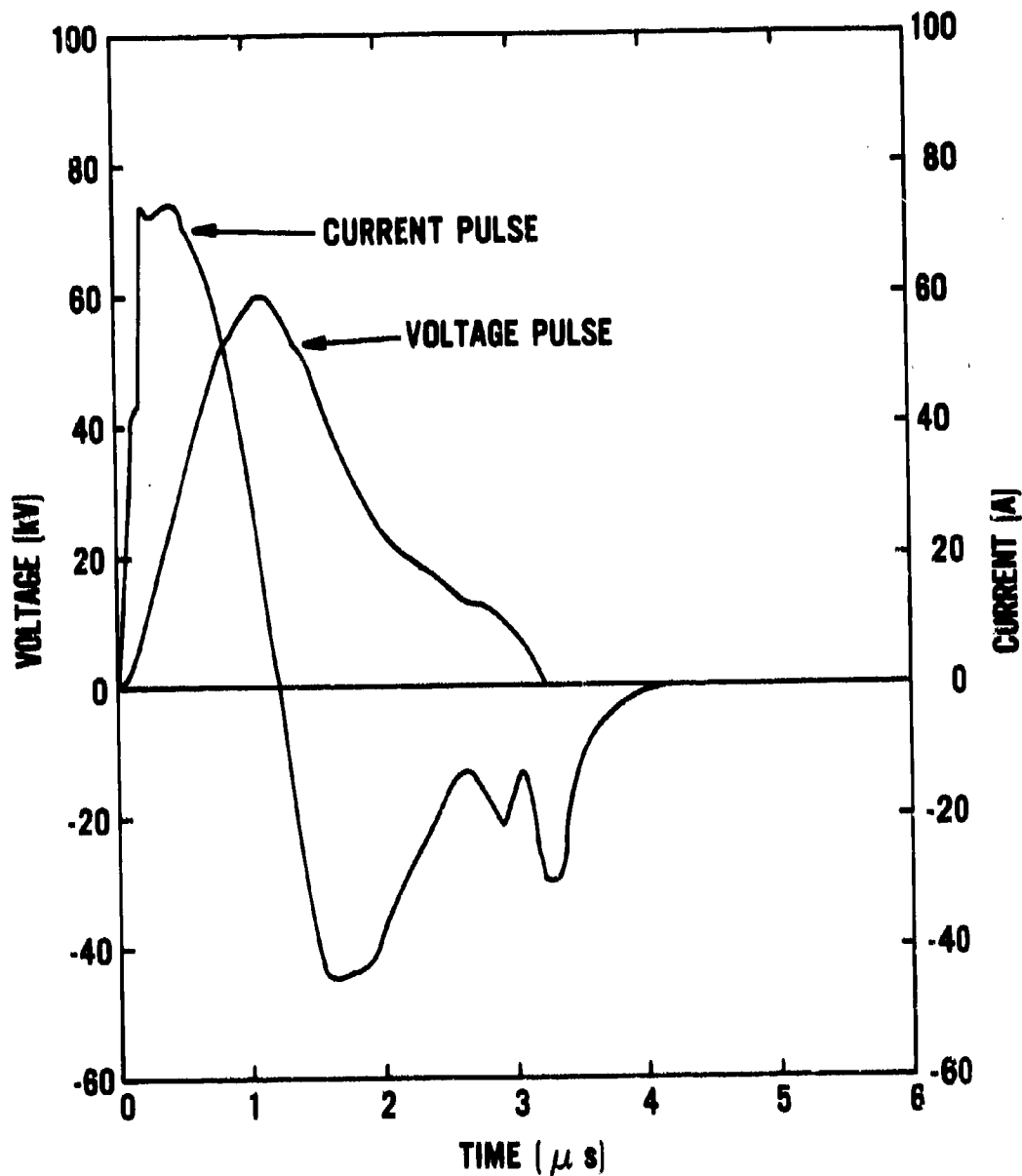


Figure 31. Voltage and current pulses for Shot 44. The PZT and load capacitances were 126 pF and 380 pF, respectively. The input shock stress to the PZT unit was 12.2 GPa. The transit time for the depoling stress wave was taken to be 2.7  $\mu s$  near the beginning of the second negative increase in the current. The maxima were 60 kV and 32.1 A.

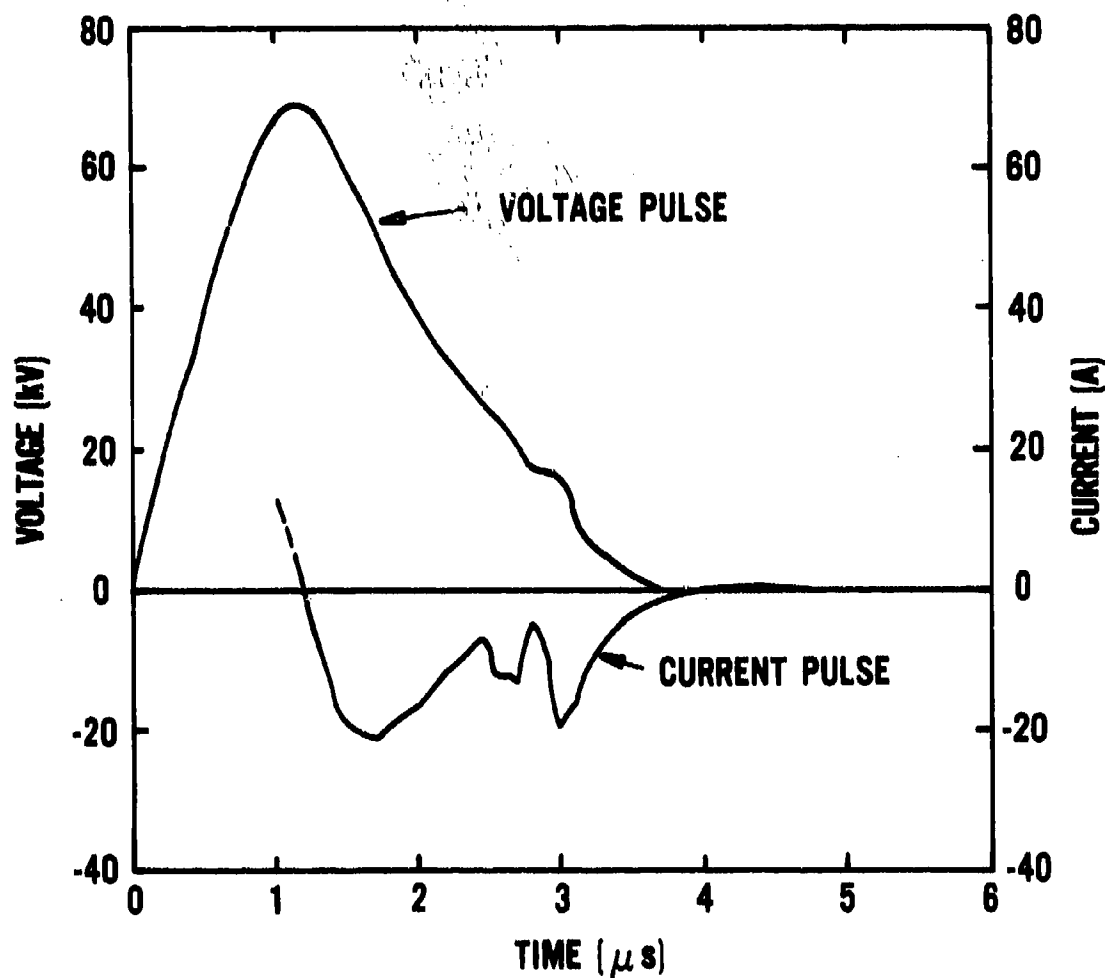


Figure 32. Voltage and current pulses for Shot 47. The PZT and load capacitances were 121 pF and 389 pF, respectively. The input shock stress to the PZT unit was 10.8 GPa. The transit time for the depoling stress wave was taken to be 2.8  $\mu$ s near the small plateau in the voltage pulse and the beginning of the third negative increase in the current pulse. Most of the positive portion of the current pulse was not recorded. The maximum voltage was 69 kV.

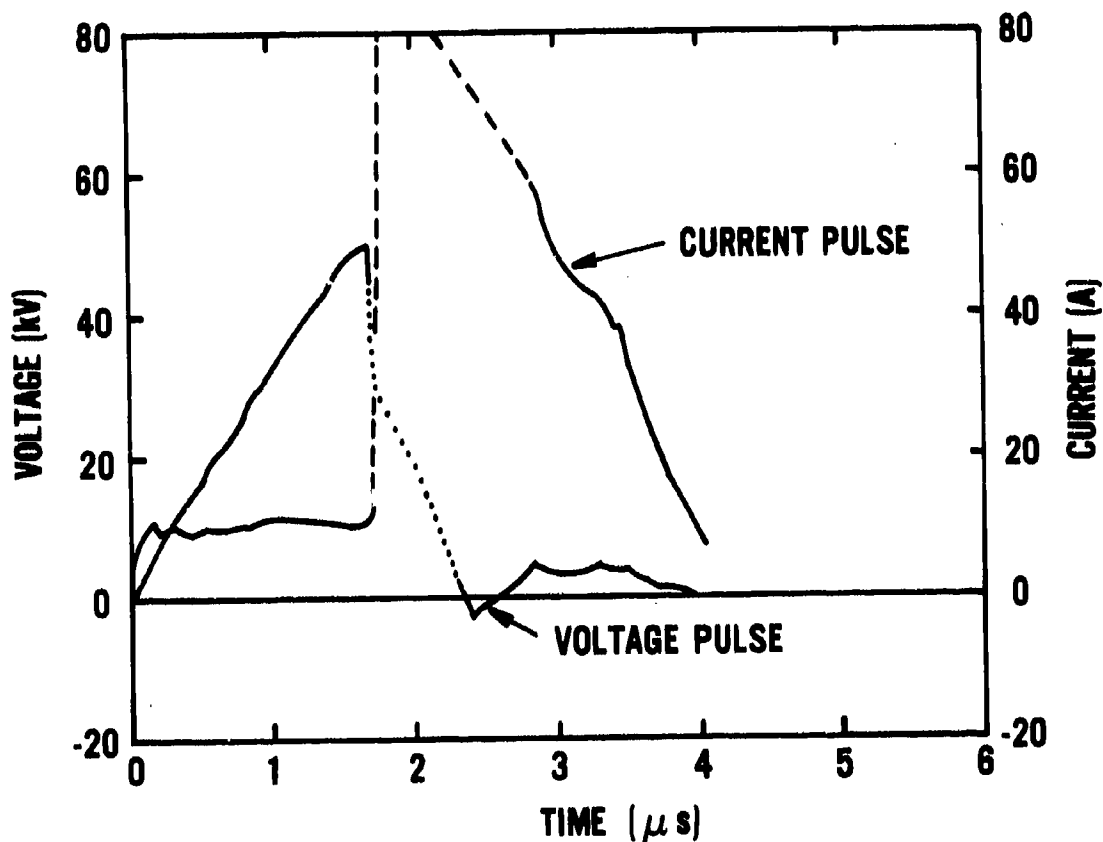


Figure 33. Voltage and current pulses for Shot 58. The PZT and load capacitances were 250 pF and 260 pF, respectively. The input shock stress to the PZT unit was 7.0 GPa. The transit time for the depoling stress wave was taken to be 3.0  $\mu\text{s}$  near the beginning of a peak in the current pulse. Electrical breakdown external to the PZT unit was evident between 1.7  $\mu\text{s}$  and 2.9  $\mu\text{s}$  from the abrupt changes in the current. The maximum voltage was 50 kV, and the maximum current prior to breakdown was 11.0 A.



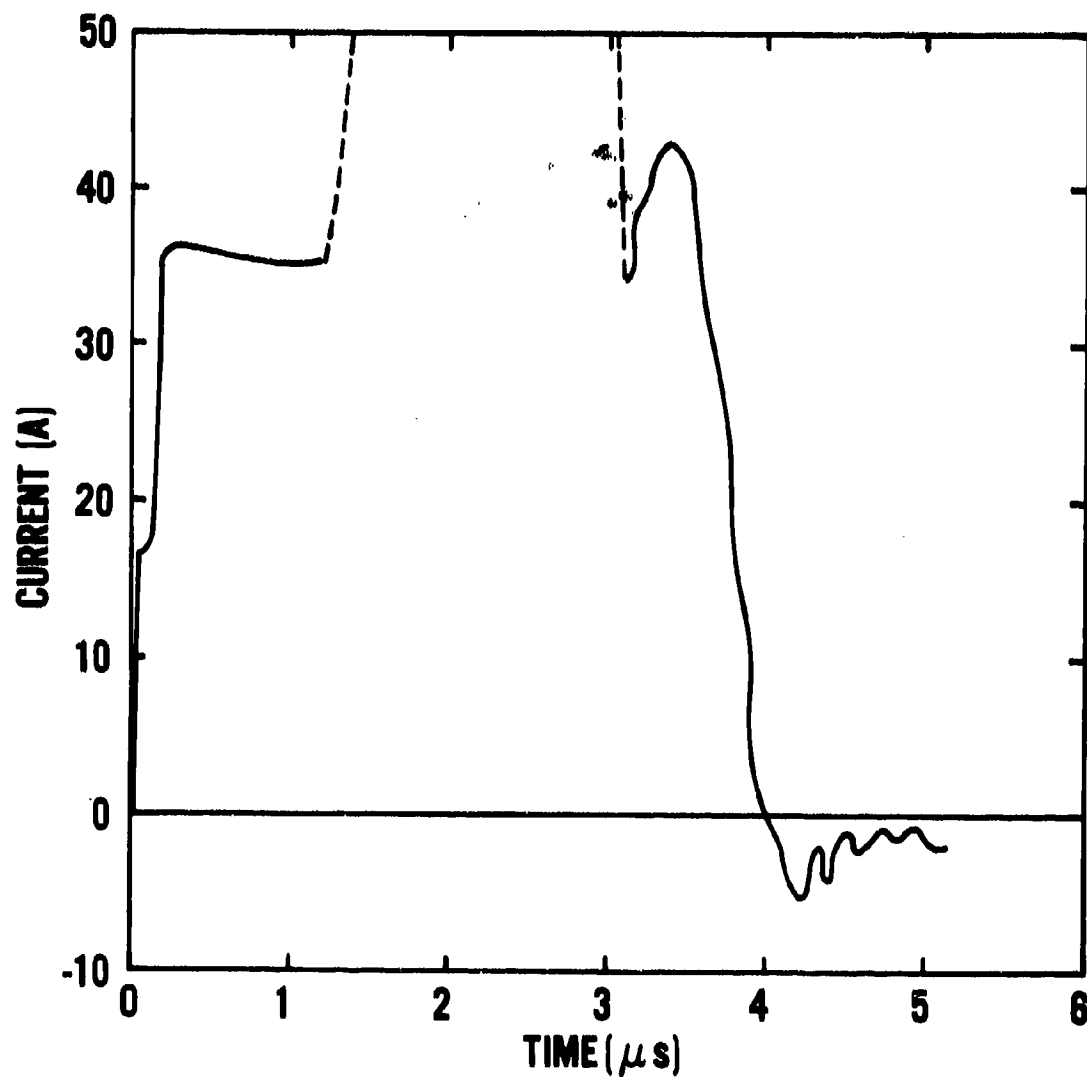


Figure 34. Current pulse for Shot 59. The PZT and load capacitances were 129 pF and 395 pF, respectively. The input shock stress to the PZT unit was 7.0 GPa. The transit time for the depoling stress wave was taken to be 3.1  $\mu$ s near the beginning of a peak in the pulse. Electrical breakdown external to the PZT unit was evident between 1.0  $\mu$ s and 2.7  $\mu$ s from the abrupt changes in the current. The maximum current prior to breakdown was taken to be 36 A. Noise pulses on the CVR oscilloscope record obscured portions of the current pulse, so that the maximum current value is uncertain.

Voltage and current pulses for the experiments with similar PZT units and load capacitances are compared as a function of shock stress in Figures 35 through 38.

The voltage and current pulses obtained for 7.1 GPa (Shots 12 and 15) are shown in Figure 35. The maximum voltage and current for Shot 15 are 30 and 7.6 percent higher, respectively, than the corresponding values for Shot 12, which shows significant shot-to-shot variation for the same input stress.

Figure 36 shows the current pulses for 9.2, 12.6, and 13.1 GPa (Shots 39, 38, and 40, respectively). (No voltage probes were used for these experiments.) The shapes of the initial positive portions of the pulses are similar except that the durations for 12.6 and 13.1 GPa are both about half that for 9.2 GPa. For 13.1 GPa, the maximum current occurs at about  $0.5 \mu\text{s}$  instead of near  $t = 0$ ; this may be an artifact of the pulse digitization procedure, resulting from the high-frequency oscillations at the beginning of the pulse. For 13.1 GPa, the charge associated with the positive recovery region between  $3.1 \mu\text{s}$  and  $5.2 \mu\text{s}$  is about  $7 \mu\text{C}$ , or 3.5 percent of the available charge. The measured fraction of the available charge released was 0.36 for 9.2 GPa, decreasing to 0.14 and 0.16 for 12.6 and 13.1 GPa, respectively. Prior to shock transit time at  $5.2 \mu\text{s}$ , the pulse for 9.2 GPa did not show the significant negative portions observed for the other two pulses during this time. This suggests that the decreasing amplitude of the initial positive portion of the current pulse for 9.2 GPa may be due to a decreasing charge release associated with effects other than breakdown (e.g., stress attenuation, stress relief, or repoling behind the shock front).

Voltage and current pulses for 4.6, 6.6, and 9.2 GPa (Shots 42, 43, and 41, respectively) are compared in Figure 37. (No voltage probe was used in Shot 41.) As noted earlier, the pulses for 4.6 GPa approximate those of Figure 21(b). The voltage pulse for 6.6 GPa shows a more linear rise to its maximum value than does the voltage pulse for 4.6 GPa, but the voltage for 6.6 GPa decreases rapidly after its 9.5-percent higher maximum voltage is attained. From the shape of the current pulse for 6.6 GPa, there appears to be an onset of the first type of breakdown at about  $1.7 \mu\text{s}$ , followed by the onset of the third type of breakdown at about  $2.2 \mu\text{s}$ . The negative portions of the current pulses for 4.6 and 6.6 GPa are similar. The current pulse for 9.2 GPa has a shape evident of the first type of breakdown. The duration of the initial positive portion of this pulse is about 56 percent of that for the other two current pulses. The measured fraction of the available charge released was about the same for 4.6 and 9.2 GPa (0.57 and 0.53, respectively) and increased to 0.64 and 6.6 GPa.

Figure 38 shows voltage and current pulses for 7.0, 10.8, and 12.2 GPa (Shots 59, 47, and 44, respectively). (No voltage pulse is available for Shot 59.) The voltage pulses for 10.8 and 12.2 GPa are similar in shape, with a 15-percent higher maximum voltage for 10.8 GPa. The current pulses for these two stress levels are similar and show the first type of breakdown behavior. The current pulse durations were about 30 percent of that for the 7.0 GPa shot. The measured fraction of the available charge released decreased from 0.46 at 7.0 GPa to 0.27 at 12.2 GPa.

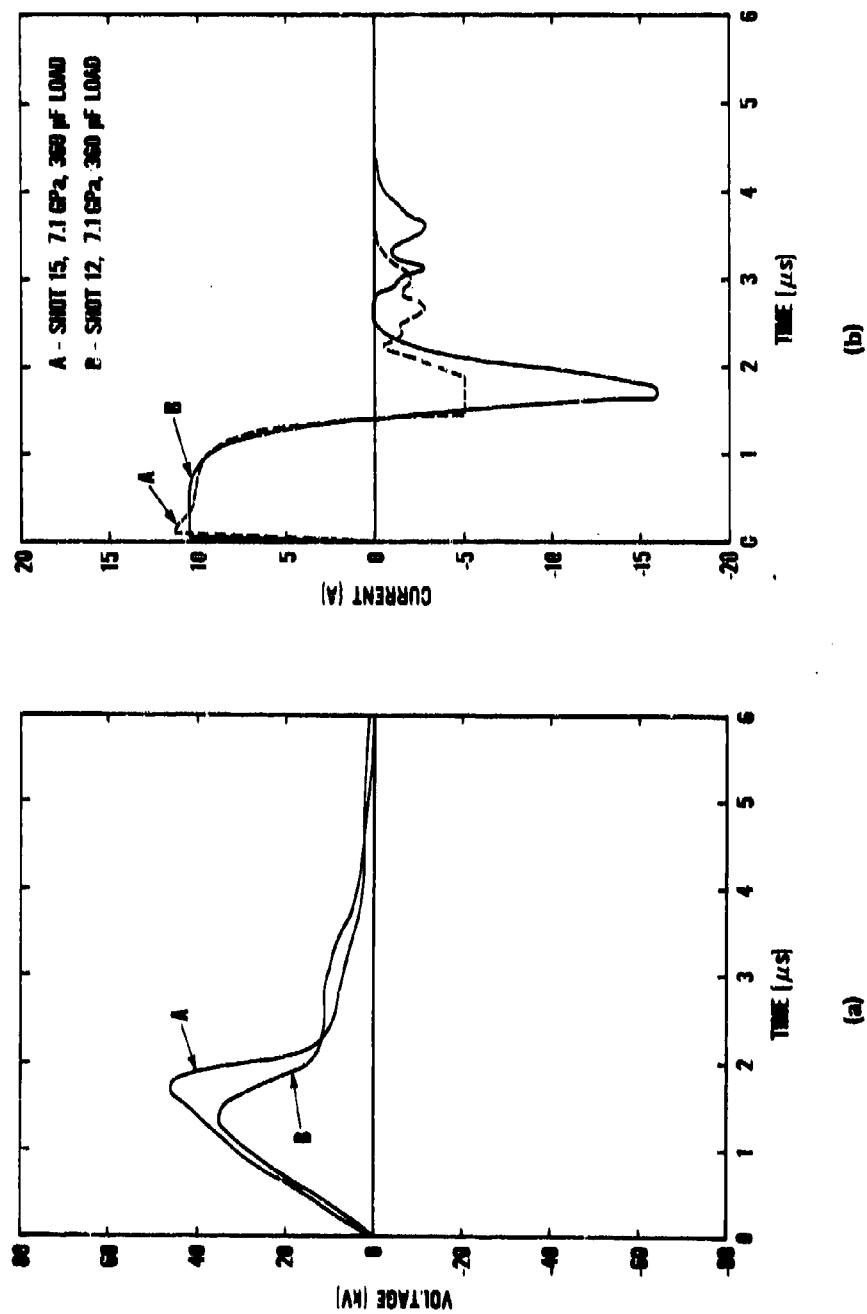


Figure 35. Voltage and current pulses as a function of shock stress (Shots 12 and 15). (a) Voltage pulses. (b) Current pulses. The PZT units had the same nominal dimensions; h, w, and  $\ell$  had average values of 12.9 mm, 12.4 mm, and 12.5 mm, respectively.

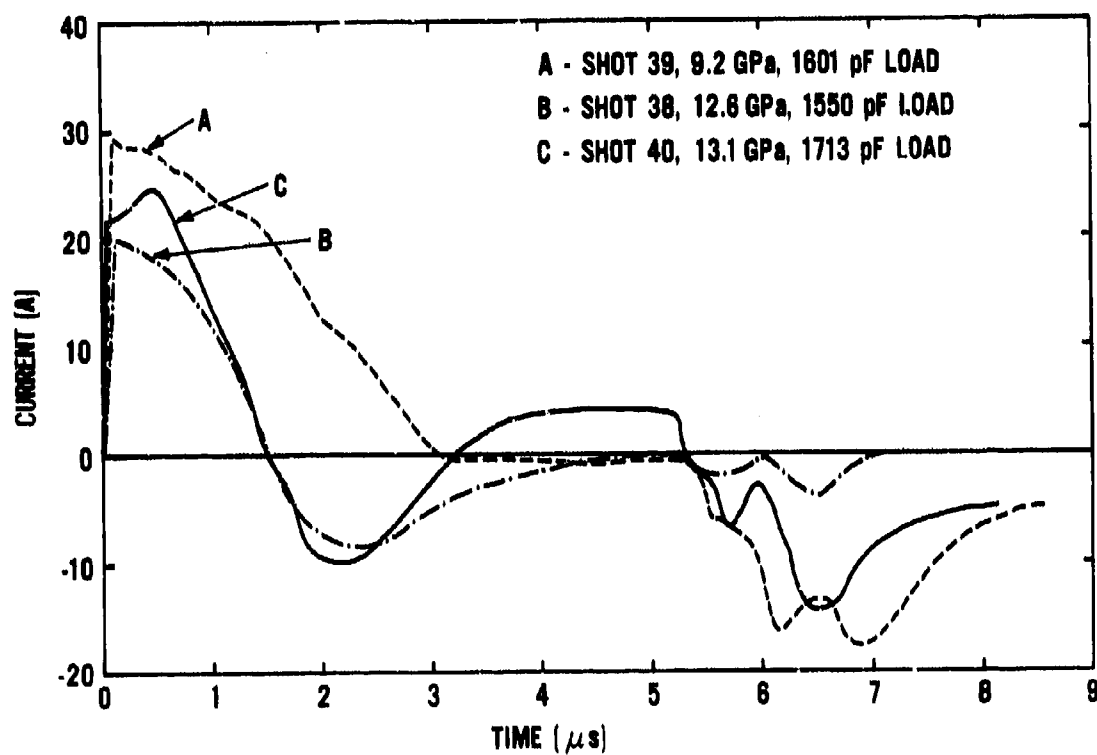


Figure 36. Current pulses as a function of shock stress (Shots 38, 39, and 40). For each shot, the pulse is from the CVR in the PZT/epoxy experimental configuration. The PZT units had the same nominal dimensions;  $h$ ,  $w$ , and  $l$  had average values of 25.6 mm, 25.0 mm, and 24.9 mm, respectively.

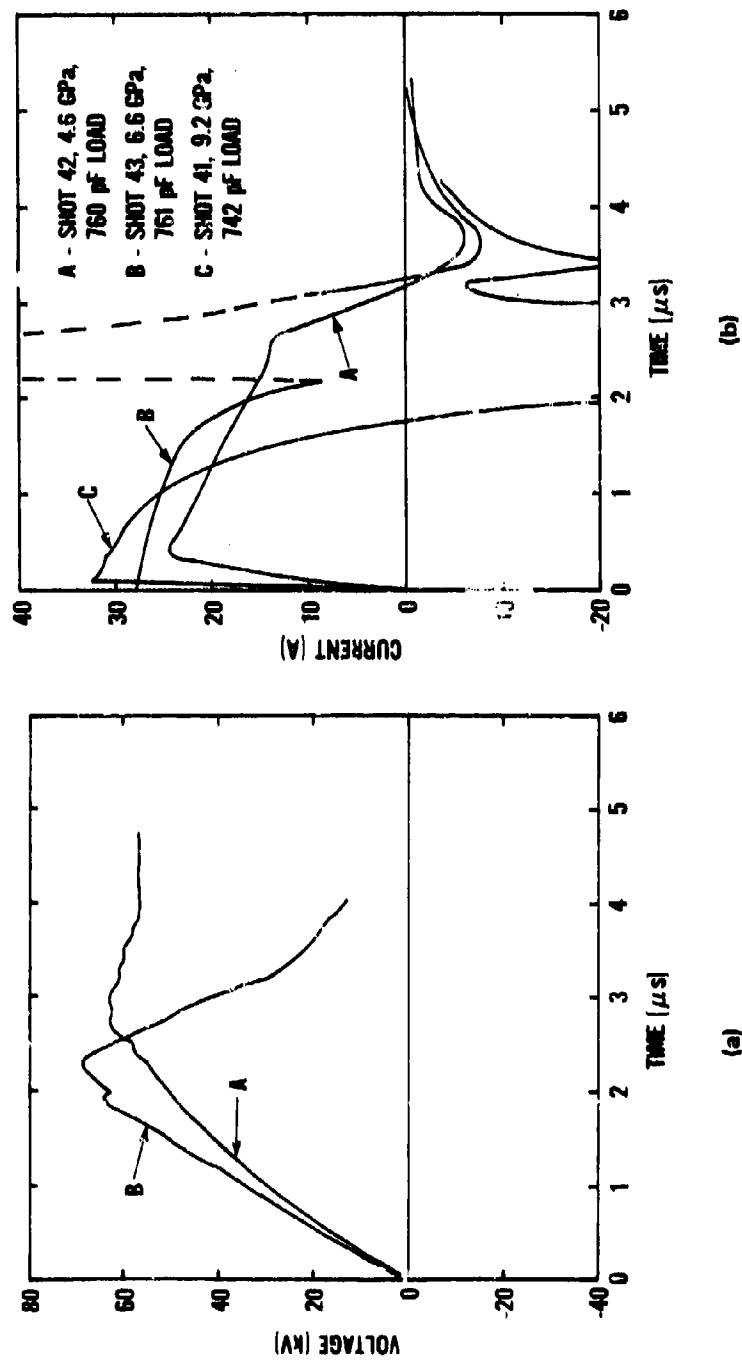


Figure 37. Voltage and current pulses as a function of shock stress (Shots 41, 42, and 43). (a) Voltage pulses. (No voltage probe was used in Shot 41.) (b) Current pulses. The PZT units had the same nominal dimensions;  $h$ ,  $w$ , and  $l$  had average values of 25.6 mm, 25.2 mm, and 12.4 mm, respectively.

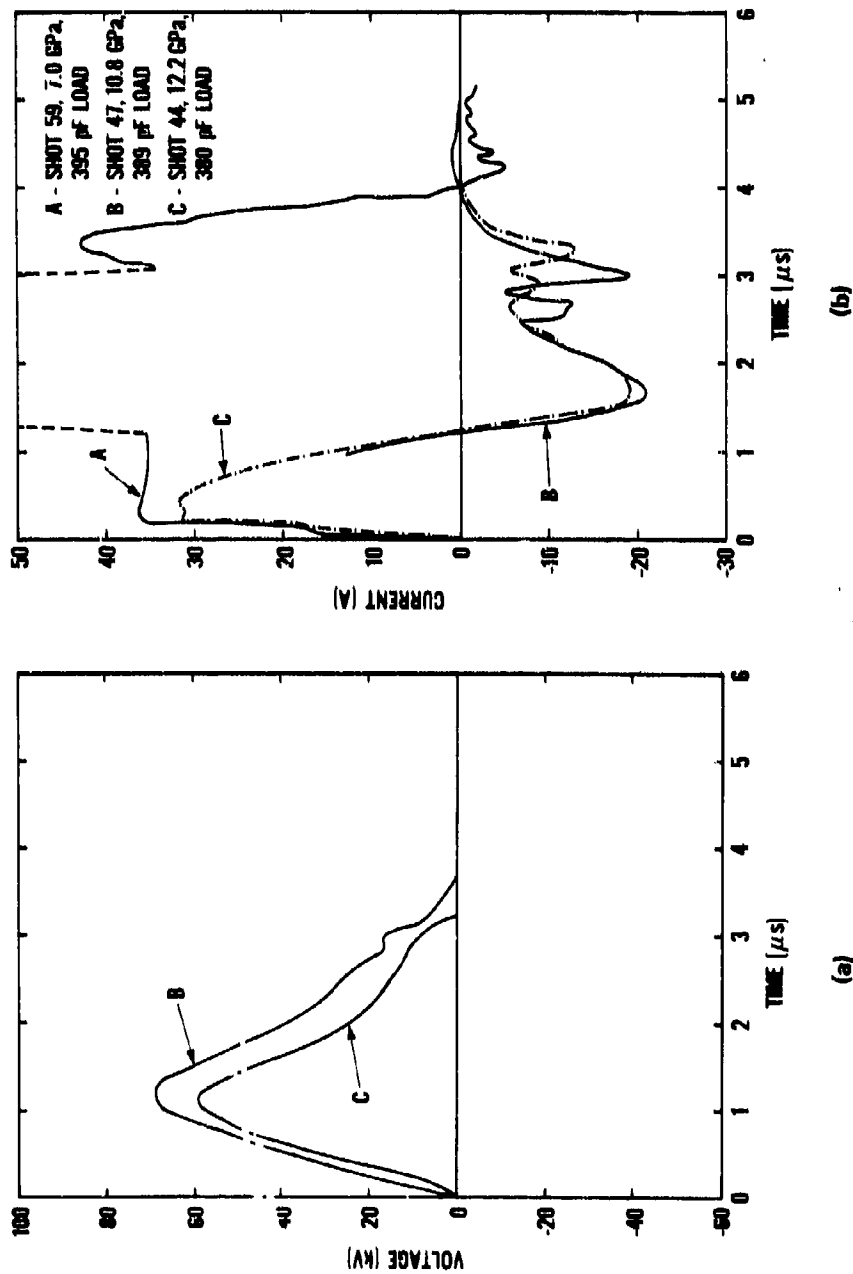


Figure 38. Voltage and current pulses as a function of shock stress (Shots 44, 47, and 59). (a) Voltage pulses. (No voltage pulse recorded for Shot 59.) (b) Current pulses. The PZT units had the same nominal dimensions; h, w, and  $\ell$  had average values of 51.0 mm, 25.2 mm, and 12.6 mm, respectively.

In Figures 39 through 47, selected electrical parameter results for all the shock depoling experiments are presented together for comparison. Data points for experiments with similar PZT unit dimensions and load capacitances are connected by lines, and the shot number is provided at each data point. An inset table in each figure gives the PZT unit dimensions and capacitance, and the load capacitance. When points are connected by lines, the table values are averages.

The maximum voltage, maximum current, fraction of available charge released, maximum electric field in the PZT unit, maximum load energy, and the average power transferred to the load are presented as a function of the peak input shock stress to the PZT unit. Also included are the fraction of the available charge released as (1) a function of the ratio of the load capacitance to the PZT capacitance,  $C_L/C$  (Figure 42) and (2) as a function of the Castall 300 epoxy thickness (Figure 43), and the measured charge release vs the theoretical charge release (Figure 44).

In Figures 39 through 42 and in Figure 46, it can be seen that the maximum voltage, maximum electric field in the PZT, maximum current, fraction of available charge released, and maximum load energy, respectively, all increase with increasing stress up to 6.6 GPa and then decrease for all higher stress values. Similar results were obtained in the gas-gun impact depoling experiments<sup>1</sup> in which the above experimental parameters increased with stress up to 7.8 GPa and then decreased for all higher stress values.

In Figure 44, the line passing through the origin indicates equality of the measured and theoretical values. All the measured charge release values are less than the theoretical values, and the deviation from the theoretical value increases with increasing shock stress. The differences in the measured and theoretical values do not appear to be correlated with shock stress.

Since Shot 42 showed a linear decrease in charge release with increasing time (in agreement with the simplified model), and since the voltage on the PZT unit increased with time, the observed linear decrease in charge release may be due to increased difficulty in releasing charge from a PZT material subjected to an external electric field. Note that the shock stress in the PZT material for Shot 42 (4.6 GPa) was the lowest for the series of depoling experiments. Note also that the charge release for all the shots showing the first type of breakdown decreased faster than a linear rate. This suggests that the stress of 4.6 GPa may be near a threshold value above which shock-induced conduction in the PZT causes a more rapid decrease in charge release with increasing time.

In Table 9, measured results for the depoling experiments are compared with calculated values based on the theoretical maximum voltage assuming ideal PZT units. Electrical breakdown prevented most of the voltage pulses from increasing to maximum values at the shock transit times; extrapolations of the initial regions of the voltage pulses were made to obtain values at the transit times for comparison with the theoretical values. The measured, extrapolated, and theoretical values are given for the maximum load voltage, charge transferred to the load, fraction of available charge transferred to load, total charge released, and fraction of available charge released.

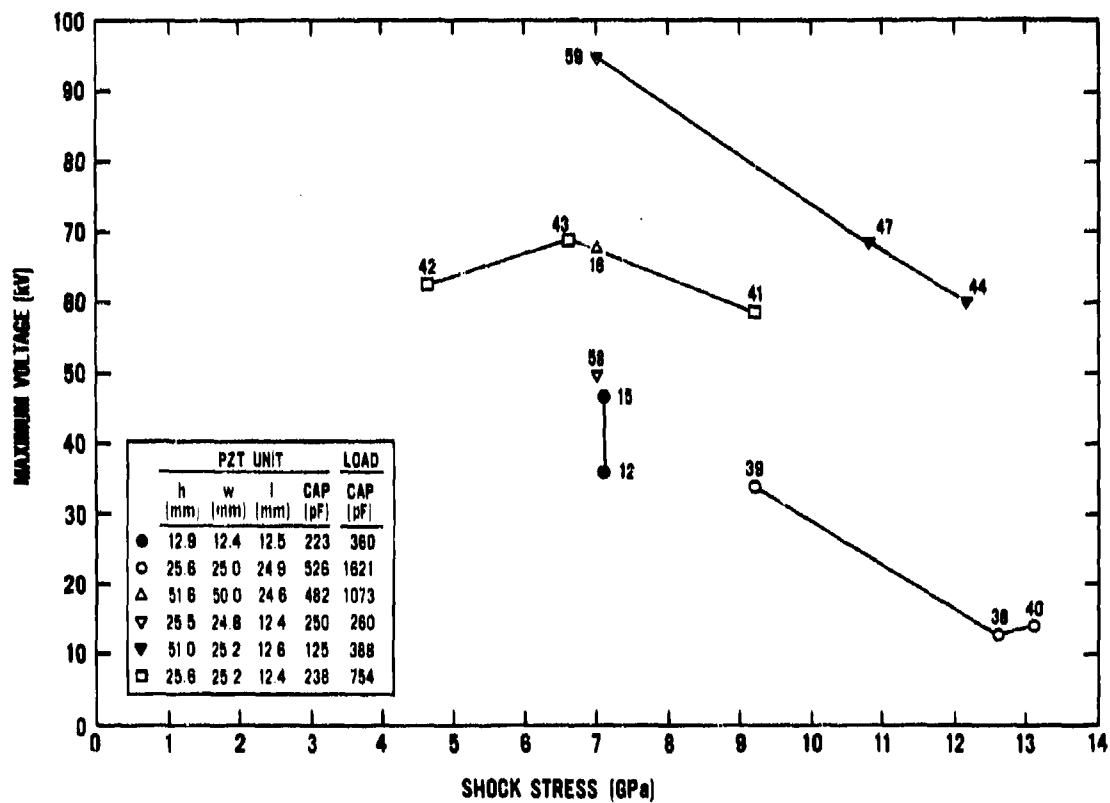


Figure 39. Maximum voltage as a function of shock stress. The lines connect points that correspond to experiments with similar PZT units and load capacitances. Shot numbers are shown at the data points. The inset table shows the unit dimensions, unit capacitance, and load capacitance. When points are connected by lines, the table values are averages.



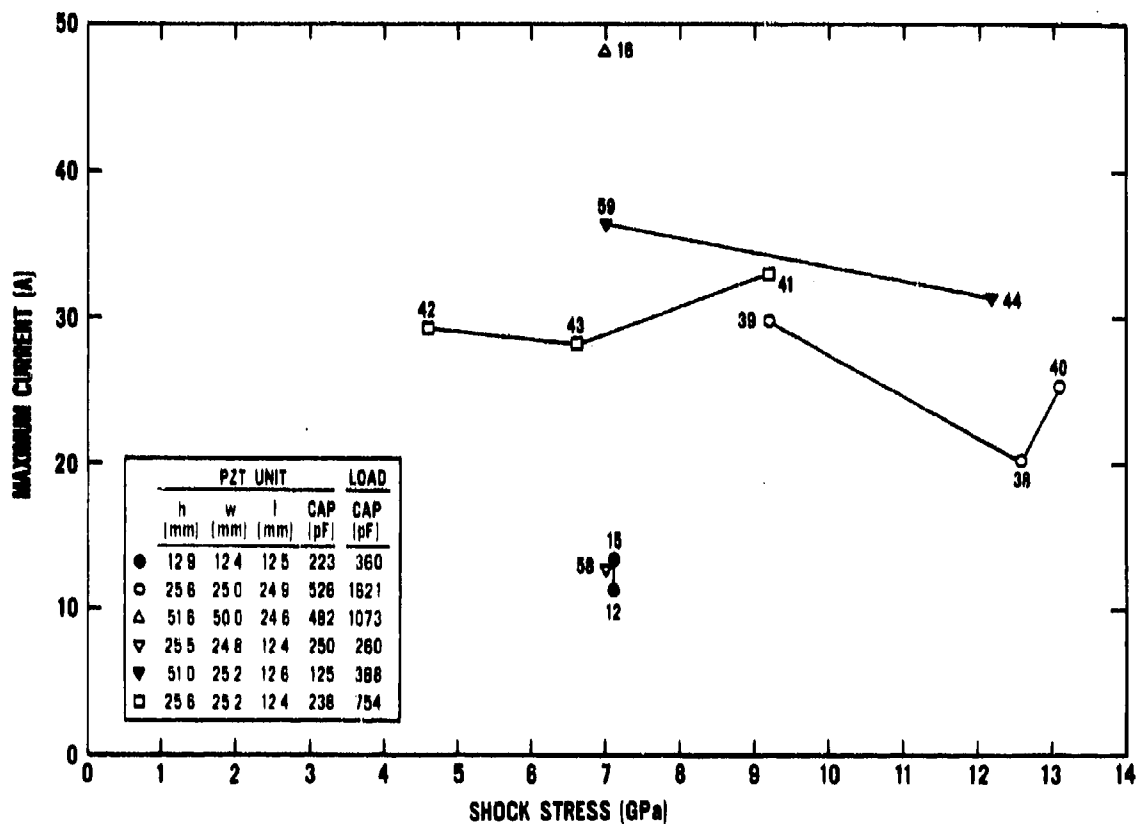


Figure 40. Maximum current in the PZT unit as a function of shock stress. The lines connect points that correspond to experiments with similar PZT units and load capacitances. Shot numbers are shown at the data points. The inset table shows the unit dimensions, unit capacitance, and load capacitance. When points are connected by lines, the table values are averages.

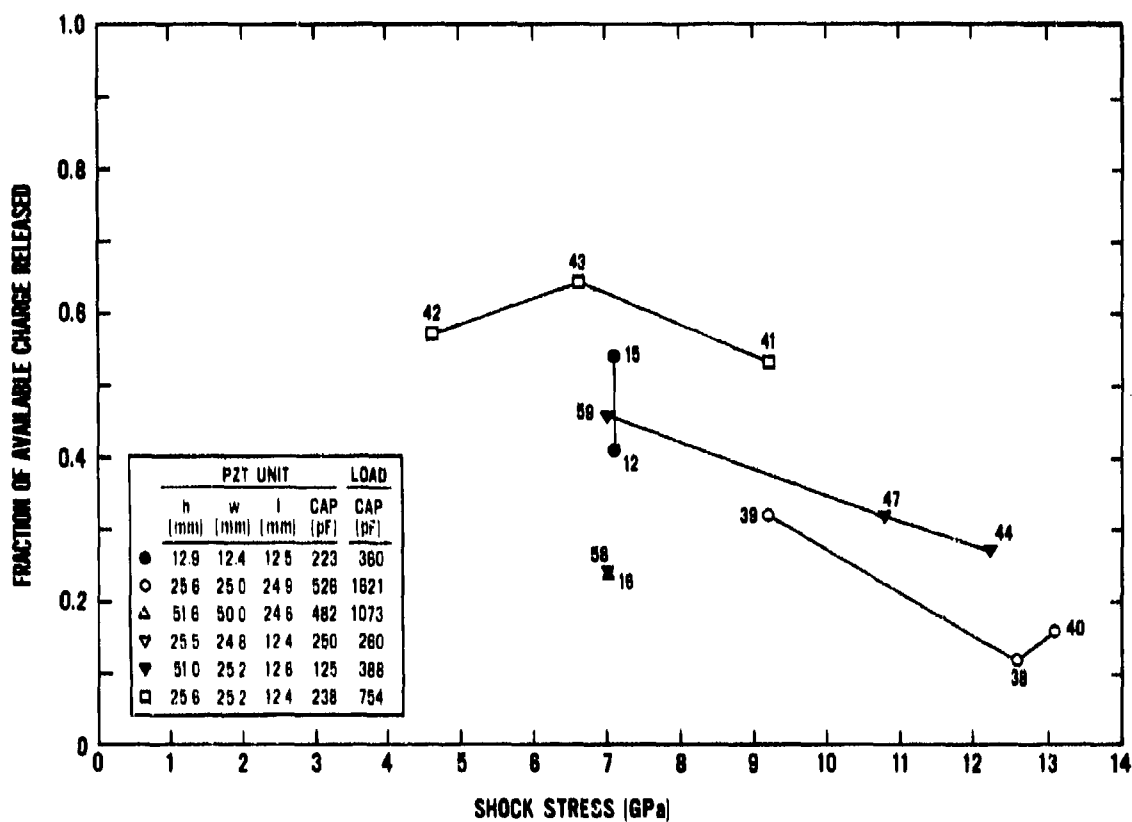
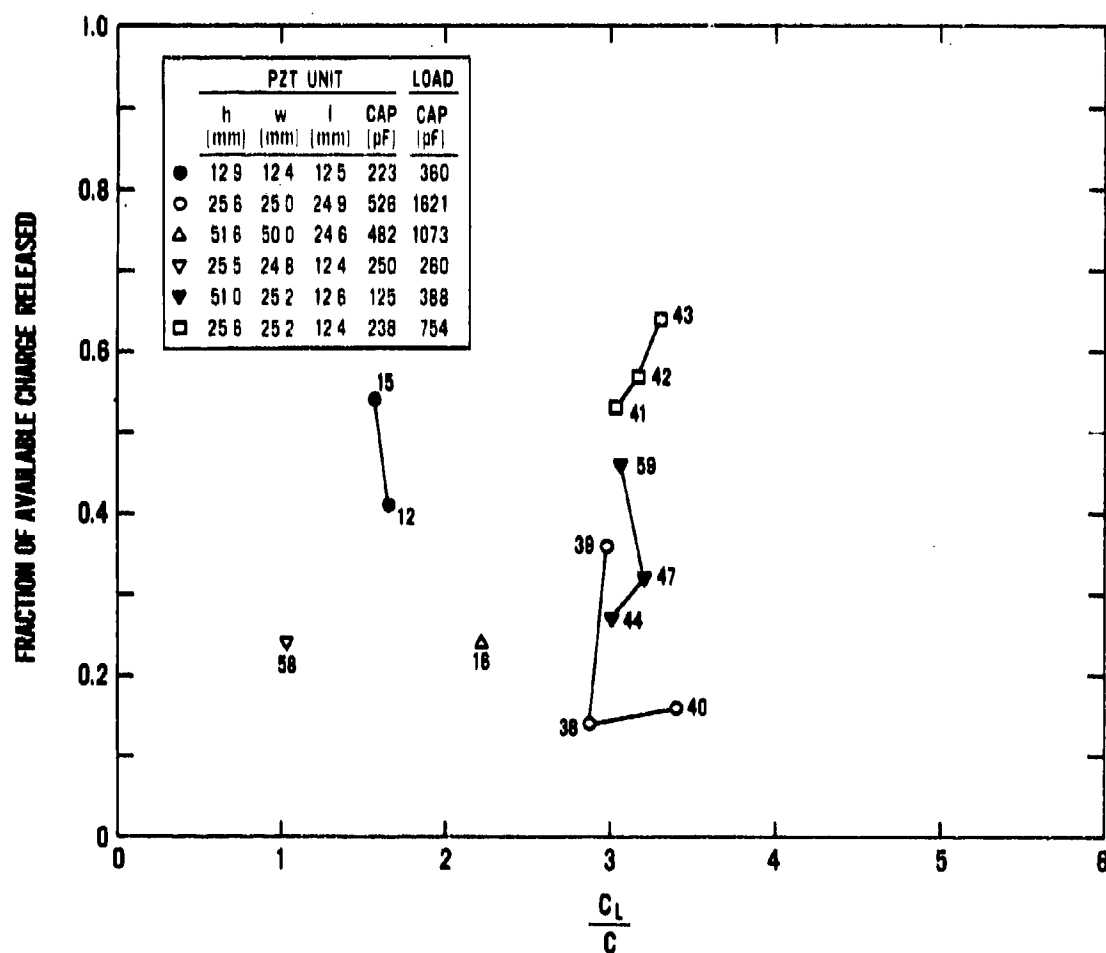


Figure 41. Fraction of available charge released as a function of shock stress. The lines connect points that correspond to experiments with similar PZT units and load capacitances. Shot numbers are shown at the data points. The inset table shows the unit dimensions, unit capacitance, and load capacitance. When points are connected by lines, the table values are averages.



**Figure 42.** Fraction of available charge released as a function of  $C_L/C$ . The lines connect points that correspond to experiments with similar PZT units and load capacitances. Shot numbers are shown at the data points. The inset table shows the unit dimensions, unit capacitance, and load capacitance. When points are connected by lines, the table values are averages.

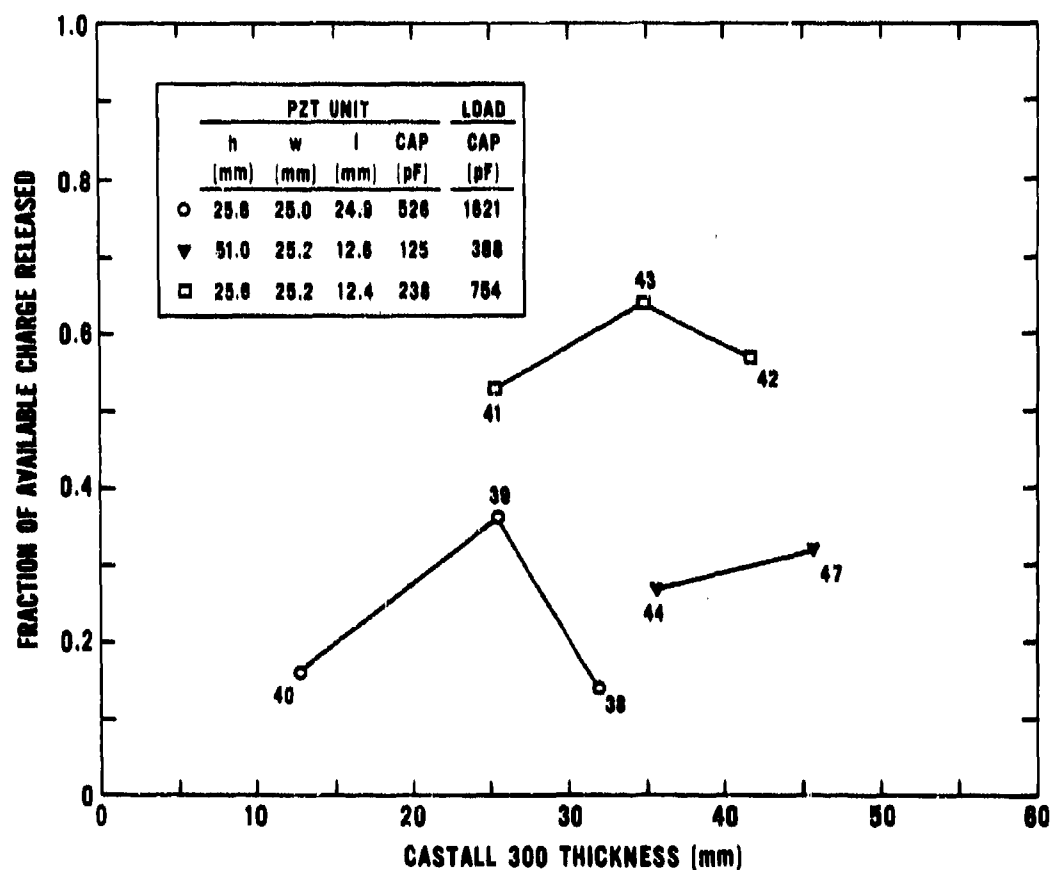


Figure 43. Fraction of available charge released as a function of Castall 300 epoxy thickness for those experiments in which Castall 300 epoxy was the only shock stress attenuator material. The lines connect points that correspond to experiments with similar PZT units and load capacitances. Shot numbers are shown at the data points. The inset table shows the unit dimensions, unit capacitance, and load capacitance. When points are connected by lines, the table values are averages.

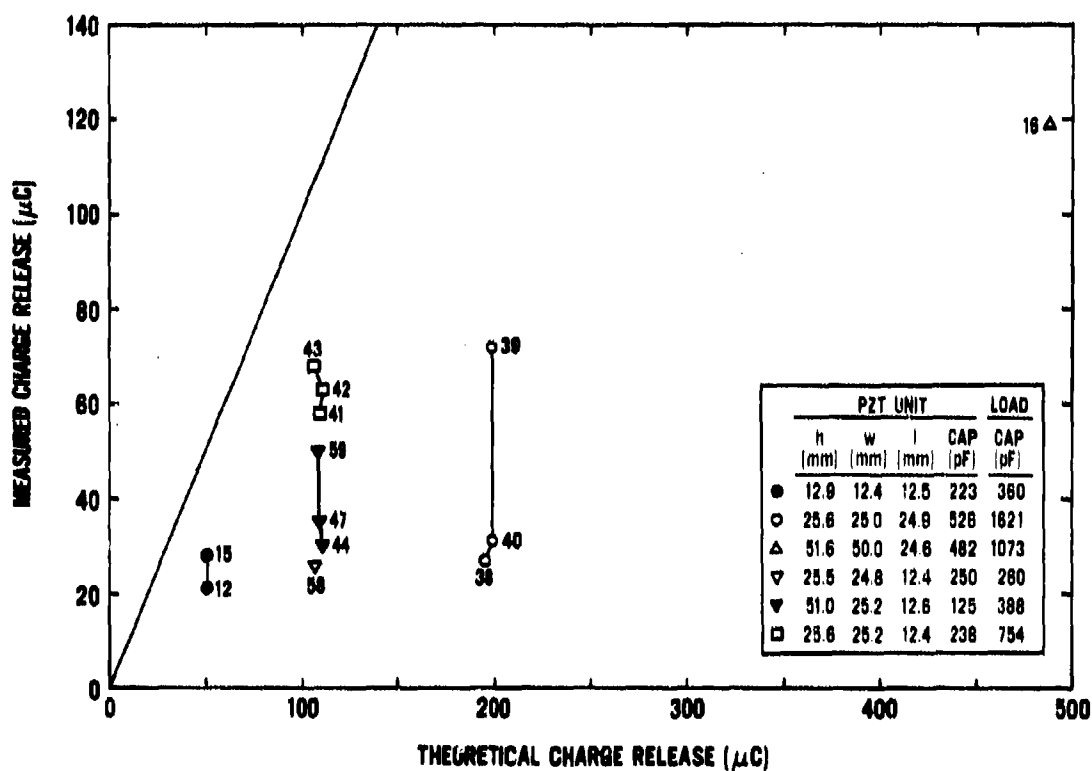


Figure 44. Measured charge release compared with theoretical charge release. The line that passes through the origin indicates equality of measured and theoretical charge release. The other lines connect points that correspond to experiments with similar PZT units and load capacitances. Shot numbers are shown at the data points. The inset table shows the unit dimensions, unit capacitance, and load capacitance. When points are connected by lines, the table values are averages.

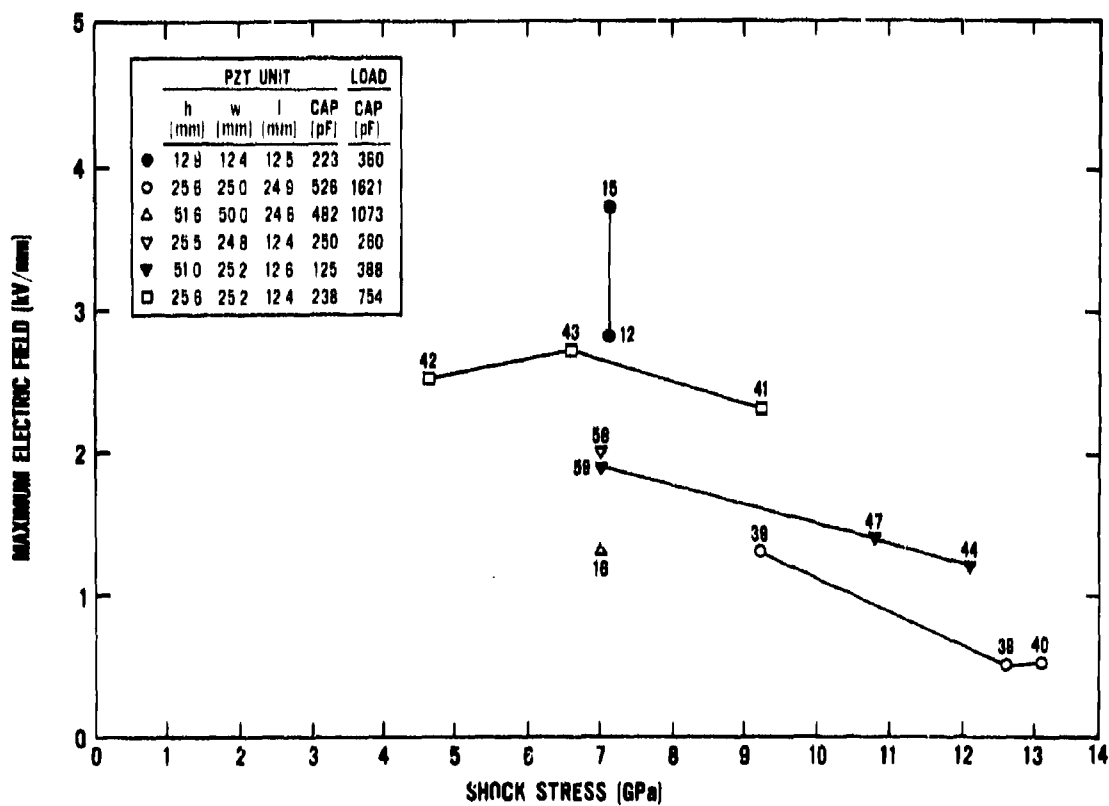


Figure 45. Maximum electric field as a function of shock stress. The lines connect points that correspond to experiments with similar PZT units and load capacitances. Shot numbers are shown at the data points. The inset table shows the unit dimensions, unit capacitance, and load capacitance. When points are connected by lines, the table values are averages.

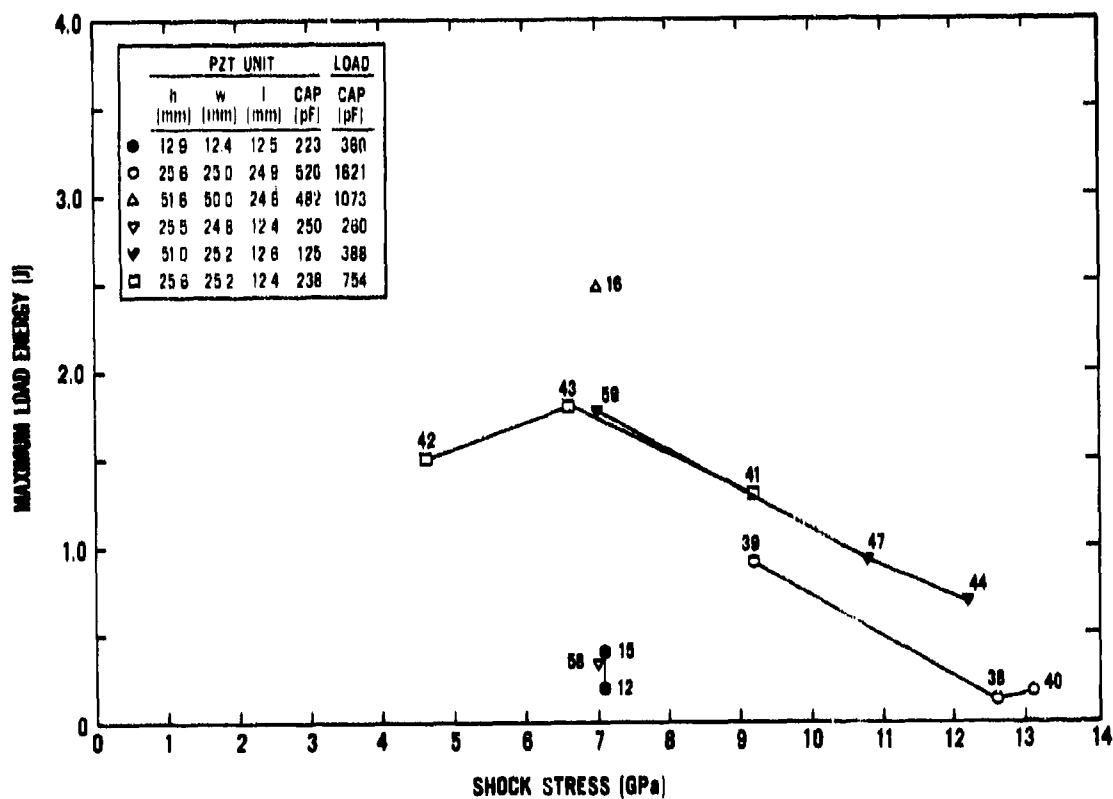


Figure 46. Maximum load energy as a function of shock stress. The lines connect points that correspond to experiments with similar PZT units and load capacitances. Shot numbers are shown at the data points. The inset table shows the unit dimensions, unit capacitance, and load capacitance. When points are connected by lines, the table values are averages.

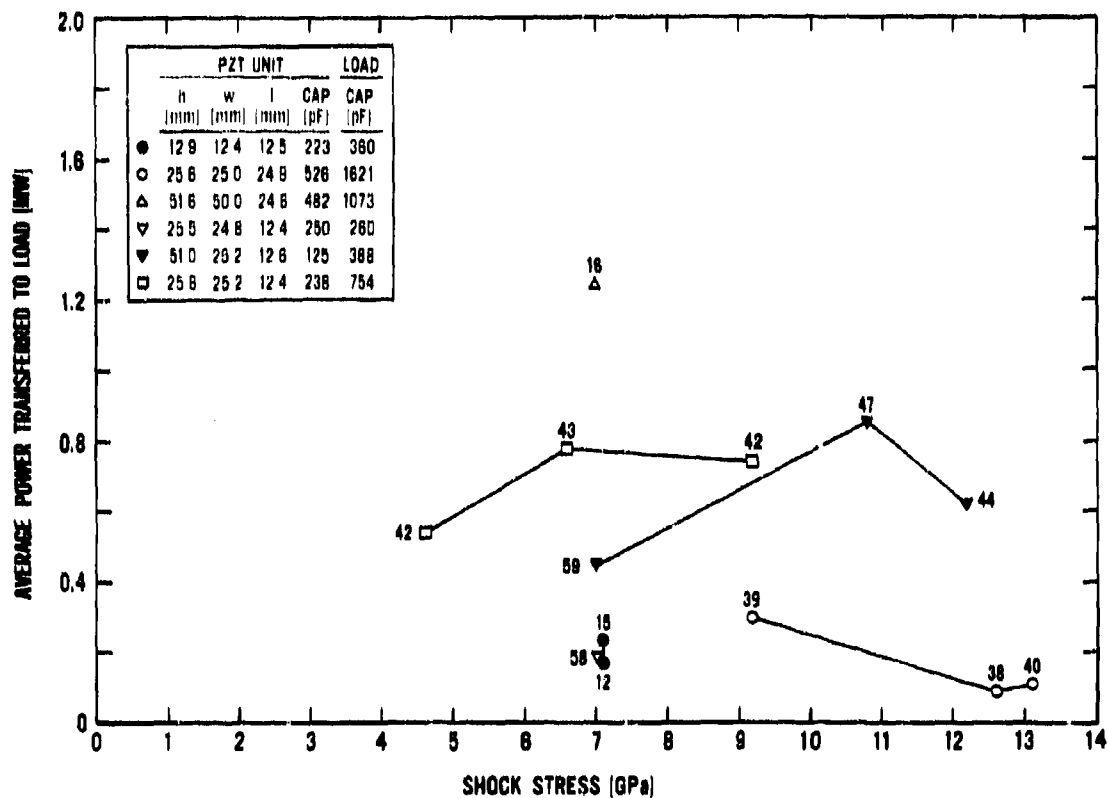


Figure 47. Average power transferred to load as a function of shock stress. The lines connect points that correspond to experiments with similar PZT units and load capacitances. Shot numbers are shown at the data points. The inset table shows the unit dimensions, unit capacitance, and load capacitance. When points are connected by lines, the table values are averages.



Table 9. Comparison of voltage results for the shock-depoled PZT units with calculations based on the theoretical maximum voltage assuming ideal units.

Shot Number	Maximum Load Voltage (kV)			Charge Transferred to Load (μC)			Fraction of Available Charge Transferred to Load			Total Charge Released <sup>d</sup> (μC)			Fraction of Available Charge Released		
	Measured	Extrapolated <sup>a</sup>	Theoretical <sup>b</sup>	Measured <sup>c</sup>	Extrapolated <sup>c</sup>	Theoretical	Measured	Extrapolated	Theoretical	Measured	Extrapolated	Theoretical	Measured	Extrapolated	Theoretical
12	36	86	89	14	31	32	0.27	0.61	0.62	21	49	51	0.41	0.97	1.0
15	47	96	87	15	35 <sup>e</sup>	31	0.29	0.69 <sup>g</sup>	0.61	28	57 <sup>h</sup>	51	0.54	1.11 <sup>i</sup>	1.0
16	68	204	278	88	260	355	0.18	0.53	0.73	119	358	489	0.24	0.73	1.0
38 <sup>j</sup>	(13)	—	94	20	—	146	0.10	—	0.74	27	—	196	0.14	—	1.0
39 <sup>j</sup>	(34)	—	93	54	—	149	0.27	—	0.75	72	—	199	0.36	—	1.0
40 <sup>j</sup>	(14)	—	90	24	—	154	0.12	—	0.77	31	—	199	0.16	—	1.0
41 <sup>j</sup>	(59)	—	112	44	—	83	0.4	—	0.75	58	—	110	0.33	—	1.0
42	63	86	111	48	65	84	0.43	0.59	0.76	63	86	111	0.37	0.77	1.0
43	69	106	108	52	81	82	0.49	0.76	0.76	68	105	107	0.64	0.98	1.0
44	50	208	219	29	79	83	0.26	0.71	0.75	30	105	111	0.27	0.95	1.0
47 <sup>a</sup>	69	225 <sup>c</sup>	216	27 <sup>j</sup>	88 <sup>g</sup>	84	0.24	0.8	0.76	35	114 <sup>h</sup>	110	0.32	1.04 <sup>i</sup>	1.0
58	60	92	210	17	24	55	0.15	0.22	0.51	26	47	107	0.24	0.44	1.0
59 <sup>j</sup>	(95)	—	198	38	—	83	0.35	—	0.77	50	—	109	0.46	—	1.0

<sup>a</sup> Obtained from extrapolation of the initial slope of the measured voltage to a value corresponding to the estimated transit time for the depoling stress wave.  
<sup>b</sup> Calculated by dividing the available charge by the total circuit capacitance.  
<sup>c</sup> It is assumed that the capacitance of the PZT does not change during shock compression.  
<sup>d</sup> If electrical breakdown occurs, the value shown is the charge transferred prior to breakdown.  
<sup>e</sup> Sum of charge released to load and charge remaining on PZT. Calculated by dividing the maximum voltage by the total circuit capacitance.

<sup>f</sup> Pulse diagnostics for these shots were based on CVRs with no voltage probes. Values in parentheses are calculated via current pulse data.  
<sup>g</sup> Value larger than for perfect unit. This is probably due to uncertainty in determining the initial slope of the voltage pulse.  
<sup>h</sup> CVR oscilloscope record did not show most of the positive portion of the current pulse.  
<sup>i</sup> Calculated from maximum voltage.  
<sup>j</sup> Voltage probe oscilloscope record for this shot did not show data. Values in parentheses are calculated via current pulse data.

The current and charge measurements obtained with the CVRs in Shots 38, 39, and 40 are compared in Table 10. A comparison of the voltage and current probe measurements of the charge transferred to the load capacitance for all the other shots is given in Table 11.

The Hugoniot elastic limit for PZT 52/48 is 1.9 GPa.<sup>21</sup> Since the peak input stresses to the PZT units were 4.6 GPa or greater for all the shots, it is expected that a multiple-wave structure, consisting of an elastic wave and at least one plastic wave, was produced in the shock-depoled PZT units. Comparing the depoling stress wave velocities from Table 8 with the 4.52 km/s ultrasonic longitudinal wave velocity for PZT 56/44<sup>1</sup> or with the 4.15 km/s elastic wave velocity for PZT 52/48<sup>21</sup> suggests that the elastic wave is primarily responsible for depoling the PZT unit in each shot. This is also suggested by the results shown in Figure 42; about 57 percent of the charge has been released with a shock stress of 4.6 GPa in Shot 42, and an additional charge release of only 7 percent is achieved for a shock stress of 6.6 GPa in Shot 43. These observations are also consistent with the results of the gas-gun impact depoling experiments with PZT 56/44.<sup>1</sup>

Lysne and Bartel<sup>15</sup> observed a ferroelectric-to-paraelectric phase change in axial-voltage-mode PZT 65/35 experiments at about 6 GPa. (PZT 65/35 is a solid solution containing 65 mole percent lead zirconate and 35 mole percent lead titanate, with niobium as a minor added constituent.) There is generally no strong evidence in the PZT 56/44 normal-voltage-mode experiments to indicate a ferroelectric-to-paraelectric phase change (such as a flat-topped current pulse that was observed in a 2.9 GPa PZT 95/5 gas-gun impact depoling experiment<sup>1</sup>); in Shot 42, the amplitude of the current pulse decreased by about 45 percent during the shock compression of the unit. (PZT 95/5 is a solid solution containing 95 mole percent lead zirconate and 5 mole percent lead titanate, with niobium as a minor added constituent.) An exception is Shot 58, for which a flat-topped current pulse was observed at 7.0 GPa; however, the suggestion of a ferroelectric-to-paraelectric phase change is probably fortuitous considering the misfire and reshocking conditions of the experiment.

Additional experimental studies, along with computational simulation, are needed to further understand the explosive-generated charge release phenomena in these ferroelectric ceramics and, hence, to improve their performance for potential pulse power source applications. The Hugoniot relations for the PZT materials of interest should also be determined.

Table 10. Comparison of current and charge measurements from the two CVRs used in Shots 38, 39, and 40.

Shot Number	CVR1		CVR2		Ratio of Measured Peak Currents <sup>c</sup>	CVR1		CVR2		Calculated Charge Release Ratio <sup>e</sup>	Measured Charge Release Ratio <sup>f</sup>
	Peak Current <sup>a</sup> (A)	Peak Current <sup>b</sup> (A)	Peak Current <sup>b</sup> (A)	Peak Current <sup>b</sup> (A)		Charge Release to Total Load <sup>d</sup> (μC)	Charge Release to Total Load <sup>d</sup> (μC)	Charge Release to Lumped Load <sup>d</sup> (μC)	Charge Release to Lumped Load <sup>d</sup> (μC)		
38	20.0	18.0	18.0	18.0	0.90	20	20	17	17	0.71	0.85
39	29.5	18.1	18.1	18.1	0.61	54	54	36	36	0.69	0.67
40	25.0	17.8	17.8	17.8	0.71	24	24	14	14	0.64	0.58

<sup>a</sup> CVR1 is located in the PZT/epoxy experimental configuration and is connected between the PZT unit and the circuit ground.

<sup>b</sup> CVR2 is located in the oil-filled box and is connected between the 1097 pF paper/oil capacitor and the circuit ground.

<sup>c</sup> Ratio of the CVR2 peak current value to the CVR1 peak current value.

<sup>d</sup> Determined by integrating the initial positive portion of the current pulse.

<sup>e</sup> Equal to the ratio of the 1097 pF capacitance to the total load capacitance.

<sup>f</sup> Ratio of the CVR2 charge release value to the CVR1 charge release value.

**Table 11. Comparison of voltage and current probe measurements of charge transferred to capacitive load.**

<b>Shot Number</b>	<b>Voltage Probe<sup>a,c</sup> (<math>\mu\text{C}</math>)</b>	<b>Current Probe<sup>b,c</sup> (<math>\mu\text{C}</math>)</b>
12	13	14
15	17	15
16	73	88
38	No probe	20
39	No probe	54
40	No probe	24
41	No probe	44
42	48	48
43	53	52
44	23	29
47	27	e
58	13	17
59	d	38

<sup>a</sup> Calculated from  $C_L V$ , where  $C_L$  is the load capacitance and  $V$  is the maximum voltage.

<sup>b</sup> Determined by integrating the initial positive portion of the current pulse from the CVR in the PZT/epoxy experimental configuration.

<sup>c</sup> If electrical breakdown occurred, the value shown is the maximum value prior to breakdown.

<sup>d</sup> Voltage probe oscilloscope record did not show data.

<sup>e</sup> CVR oscilloscope record did not show most of the initial positive portion of the current pulse.

## IX. SUMMARY

PZT 56/44 ferroelectric ceramics have been shock depoled in the normal mode using explosive plane wave techniques. The PZT material was shock loaded in the stress range from 4.6 to 13.1 GPa. Capacitors ranging from 260 to 1713 pF were charged in a few microseconds with pulses having powers ranging from about 100 kW to over 1 MW. Complete release of the PZT polarization charge was not observed in any of the experiments. This resulted from incomplete shock depoling of the PZT material or from the electrical breakdown and conduction that occurred in either the PZT units or the external circuits. Relief wave interactions, stress attenuation, or the effects of voltage buildup on the depoling process may also have contributed to incomplete charge release. A maximum load voltage of 95 kV was produced at 7.0 GPa.

## REFERENCES

1. W. Mock, Jr., and W. H. Holt, "Pulse Charging of Nanofarad Capacitors from the Shock Depoling of PZT 56/44 and PZT 95/5 Ferroelectric Ceramics," *Journal of Applied Physics*, Vol. 49, p. 5846 (1978). For further experimental details, see NSWC/DL TR-3804, Naval Surface Weapons Center, April 1978.
2. J. van Randerdaat, Ed., *Piezoelectric Ceramics*, Mullard, London (1968).
3. C. Percy, "High Voltage Generation from Piezoelectric Ceramics," *Electronic Engineering*, October 1965, p. 656.
4. W. Mock, Jr., and W. H. Holt, "Axial-Current-Mode Shock Depoling of PZT 56/44 Ferroelectric Ceramic Disks," *Journal of Applied Physics*, Vol. 50, p. 2740 (1979).
5. W. J. Halpin, "Current from a Shock-Loaded Short-Circuited Ferroelectric Ceramic Disk," *Journal of Applied Physics*, Vol. 37, p. 153 (1966).
6. J. E. Besancon, J. David, and J. Vedel, "Ferroelectric Transducers," in *Proc. Conf. on Megagauss Magnetic Field Generation by Explosives and Related Experiments*, H. Knoepfel and F. Herlach, Eds. (Euratom, 1966), p. 315.
7. P. C. Lysne and C. M. Percival, "Electric Energy Generation by Shock Compression of Ferroelectric Ceramics: Normal-Mode Response of PZT 95/5," *Journal of Applied Physics*, Vol. 46, p. 1519 (1975).
8. F. Bauer, K. Vollrath, Y. Fétiqueau, and L. Eyraud, "Ferroelectric Ceramics: Application to Mechanical Electrical Energy Conversion Under Shock Compression," *Ferroelectrics*, Vol. 10, p. 61 (1976).
9. P. C. Lysne and C. M. Percival, "Analysis of Shock-Wave-Actuated Ferroelectric Power Supplies," *Ferroelectrics*, Vol. 10, p. 129 (1976).
10. B. Jaffe, W. R. Cook, Jr., and H. Jaffe, *Piezoelectric Ceramics*, Academic Press, N.Y. (1971).
11. W. J. Halpin, "Resistivity Estimates for Some Shocked Ferroelectrics," *Journal of Applied Physics*, Vol. 39, p. 3821 (1968).
12. J. T. Cutchen, "Polarity Effects and Charge Liberation in Lead Zirconate Titanate Ceramics under High Dynamic Stress," *Journal of Applied Physics*, Vol. 37, p. 4745 (1966).
13. R. K. Linde, "Depolarization of Ferroelectrics at High Strain Rates," *Journal of Applied Physics*, Vol. 38, p. 4839 (1967).
14. P. C. Lysne, "Dielectric Breakdown of Shock-Loaded PZT 65/35," *Journal of Applied Physics*, Vol. 44, p. 577 (1973).

15. P. C. Lysne and L. C. Bartel, "Electromechanical Response of PZT 65/35 Subjected to Axial Shock Loading," *Journal of Applied Physics*, Vol. 46, p. 222 (1975).
16. P. C. Lysne, "Prediction of Dielectric Breakdown in Shock-Loaded Ferroelectric Ceramics," *Journal of Applied Physics*, Vol. 46, p. 230 (1975).
17. P. C. Lysne, "Kinetic Effects in the Electrical Response of a Shock-Compressed Ferroelectric Ceramic," *Journal of Applied Physics*, Vol. 46, p. 4078 (1975).
18. P. C. Lysne, "Dielectric Properties of Shock-Wave-Compressed PZT 95/5," *Journal of Applied Physics*, Vol. 48, p. 1020 (1977).
19. P. C. Lysne, "Shock-Induced Polarization of a Ferroelectric Ceramic," *Journal of Applied Physics*, Vol. 48, p. 1024 (1977).
20. W. H. Holt, J. B. Bickley, and W. Mock, Jr., *The Spikeducer: A Time-of-Arrival Pin Configuration for Shock Wave Experiments*, NSWC/DL TR-3492, Naval Surface Weapons Center, Dahlgren, Va. (June 1976).
21. C. E. Reynolds and G. E. Seay, "Two-Wave Shock Structures in the Ferroelectric Ceramics Barium Titanate and Lead Zirconate Titanate," *Journal of Applied Physics*, Vol. 33, p. 2234 (1962).
22. W. Mock, Jr., and W. H. Holt, "Shock-Wave Compression of an Alumina-Filled Epoxy in the Low Gigapascal Stress Range," *Journal of Applied Physics*, Vol. 49, p. 1156 (1978).
23. O. E. Jones, "Metal Response to Explosive Loading," in Behavior and Utilization of Explosives in Engineering Design, Proceedings of 12th Annual Symposium, New Mexico Section, American Society of Mechanical Engineers (Albuquerque, N.M., 1972), p. 125.
24. W. B. Benedict, "Detonation Wave Shaping," in Behavior and Utilization of Explosives in Engineering Design, Proceedings of 12th Annual Symposium, New Mexico Section, American Society of Mechanical Engineers (Albuquerque, N.M., 1972), p. 47.
25. L. H. Lee, "Nonlinearity in the Piezoresistive Coefficient of Impact-Loaded Manganin," *Journal of Applied Physics*, Vol. 44, p. 4017 (1973).
26. R. G. McQueen, S. P. Marsh, J. W. Taylor, J. N. Fritz, and W. J. Carter, "The Equation of State of Solids from Shock Wave Studies," in *High Velocity Impact Phenomena*, R. Kinslow, Ed. (Academic Press, N.Y., 1960), p. 293.
27. "Selected Hugoniot," Los Alamos Scientific Laboratory Report LA-4167-MS (1969).
28. W. E. Drummond, "Explosive Induced Shock Waves. Part I. Plane Shock Waves," *Journal of Applied Physics*, Vol. 28, p. 1437 (1957).

**APPENDIX A**

**DISCUSSION OF ELECTRICAL EQUATIONS FOR THE  
IDEAL RESPONSE OF A PZT UNIT WITH A  
CAPACITIVE LOAD**



In Section VII, a simplified model was presented for the ideal and nonideal responses of a PZT unit. Equations for the charge release, voltage, and current were derived for these responses. Some of the equations that were derived in Section VII are repeated here for completeness. In addition, the energy equations for the ideal response of a PZT unit are derived. Plots based on these equations and a discussion in terms of the load to source capacitance ratio  $C_L/C$  are provided.

At time  $t$ , the charge release by the shock wave is

$$Q(t) = \begin{cases} P_0 A \frac{t}{\tau}, & 0 \leq t \leq \tau, \\ P_0 A, & t > \tau \end{cases} \quad (A-1)$$

where  $\tau$  is the shock transit time in the PZT unit. The charge on the PZT unit is

$$q(t) = \begin{cases} P_0 A \frac{C}{C+C_L} \left( \frac{t}{\tau} \right), & 0 \leq t \leq \tau, \\ P_0 A \frac{C}{C+C_L}, & t > \tau \end{cases} \quad (A-2)$$

The charge on the capacitive load is

$$q_L(t) = \begin{cases} P_0 A \frac{C_L}{C+C_L} \left( \frac{t}{\tau} \right), & 0 \leq t \leq \tau, \\ P_0 A \frac{C_L}{C+C_L}, & t > \tau \end{cases} \quad (A-3)$$

The voltage on the PZT unit and capacitive load is

$$V(t) = \begin{cases} \frac{P_0 A}{C+C_L} \left( \frac{t}{\tau} \right), & 0 \leq t \leq \tau \\ \frac{P_0 A}{C+C_L}, & t > \tau \end{cases} \quad (A-4)$$

Figure A-1 is a plot of the normalized charge  $q(t)/(P_0A)$  and normalized voltage  $V(t)/(P_0A/C)$  on the PZT unit. The charging region ( $0 \leq t \leq \tau$ ) is characterized by a constant slope determined by the  $C_L/C$  ratio. For the open circuit case ( $C_L/C = 0$ ), no charge is transferred to the load; all the released charge remains on the PZT unit. The charging region slope is  $P_0A/\tau$  for the open circuit case. For the short circuit case ( $C_L/C = \infty$ ), all the charge is transferred to the load at zero voltage.

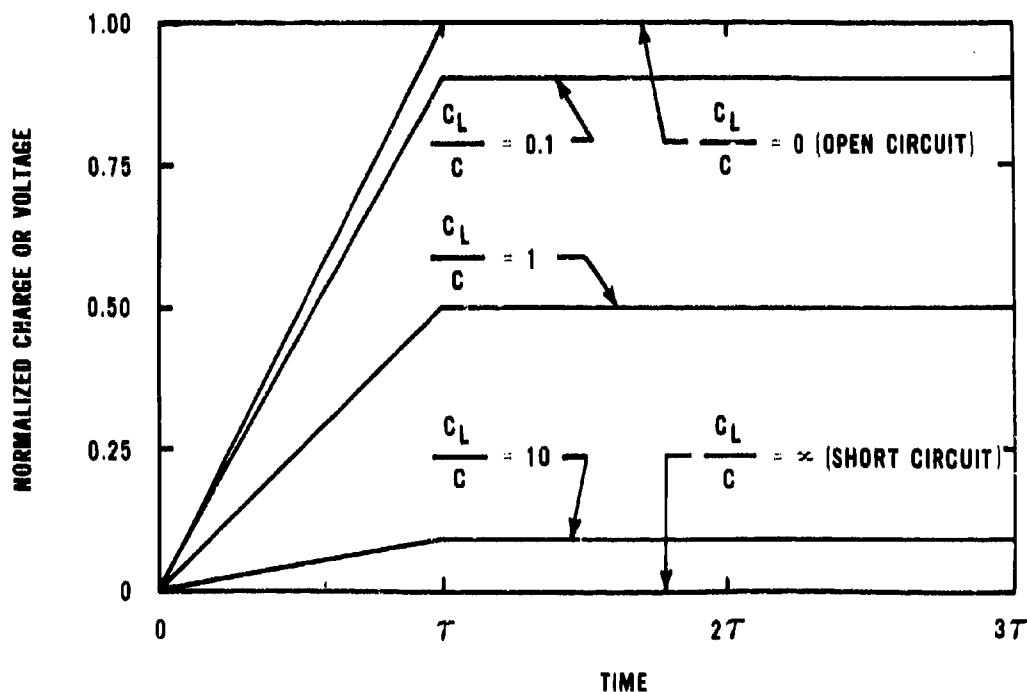


Figure A-1. Normalized charge and voltage on the PZT unit for various values of  $C_L/C$ .

The current is given by the equation

$$i(t) = \begin{cases} \frac{P_0A}{\tau} \frac{C_L}{C + C_L} & , 0 \leq t \leq \tau, \\ 0 & , t > \tau \end{cases} \quad (A-5)$$

Figure A-2 is a plot of the normalized current  $i(t)/(P_0 A/\tau)$ . The current is a constant amplitude pulse for  $0 \leq t \leq \tau$  and zero for  $t > \tau$ . For the short circuit case, the rate of charge release by the shock wave  $P_0 A/\tau$  equals the amplitude of the short-circuit current pulse. The amplitude of the current pulse for a general load capacitor is a fraction of the short circuit current; the fraction is determined by the ratio of the load capacitance  $C_L$  to the total circuit capacitance.

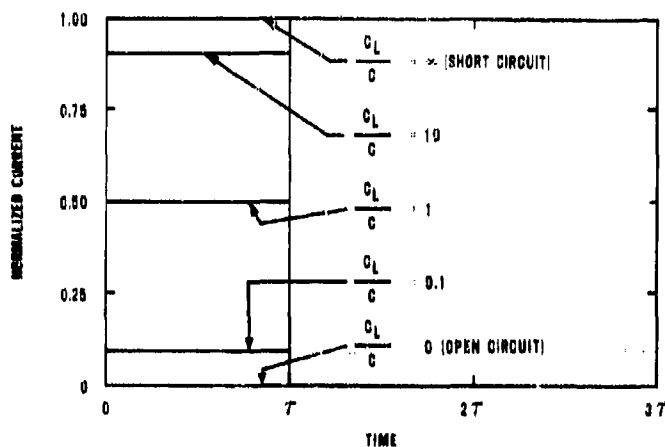


Figure A-2. Normalized circuit current for various values of  $C_L/C$ .

The energy on the PZT unit is given by

$$E(t) = \begin{cases} \frac{(P_0 A)^2}{2C} \left( \frac{C}{C + C_L} \right)^2 \left( \frac{t}{\tau} \right)^2, & 0 \leq t \leq \tau \\ \frac{(P_0 A)^2}{2C} \left( \frac{C}{C + C_L} \right)^2, & t > \tau \end{cases} \quad (A-6)$$

The energy on the capacitive load is

$$\mathcal{E}_L(t) = \begin{cases} \frac{(P_0 A)^2}{2C} \frac{CC_L}{(C + C_L)^2} \left(\frac{t}{\tau}\right)^2, & 0 \leq t \leq \tau, \\ \frac{(P_0 A)^2}{2C} \frac{CC_L}{(C + C_L)^2}, & t > \tau \end{cases} \quad (\text{A-7})$$

The total circuit energy  $\mathcal{E}_T(t) = \mathcal{E}(t) + \mathcal{E}_L(t)$  is

$$\mathcal{E}_T(t) = \begin{cases} \frac{(P_0 A)^2}{2C} \frac{C}{C + C_L} \left(\frac{t}{\tau}\right)^2, & 0 \leq t \leq \tau, \\ \frac{(P_0 A)^2}{2C} \frac{C}{C + C_L}, & t > \tau \end{cases} \quad (\text{A-8})$$

Figures A-3, A-4, and A-5 are plots of the normalized PZT energy  $\mathcal{E}(t)/((P_0 A)^2/2C)$ , the normalized load energy  $\mathcal{E}_L(t)/((P_0 A)^2/2C)$ , and the normalized total energy  $\mathcal{E}_T(t)/((P_0 A)^2/2C)$ , respectively. For the open circuit case ( $C_L/C = 0$ ), all the released charge remains on the PZT unit; the circuit energy has a maximum value of  $(P_0 A)^2/2C$ . For the short circuit case ( $C_L/C = \infty$ ), all the energy equations are zero for all time  $t$  even though a current of magnitude  $P_0 A/\tau$  flows in the circuit. As shown in Figure A-4, the energy transferred to the load capacitor is a maximum for  $C_L/C = 1$ ; less energy is transferred for  $C_L/C$  greater or less than this value. This maximum energy value is  $(P_0 A)^2/8C$ , which is four times smaller than the maximum energy on the PZT unit for the open circuit case. In summary, maximum charge is transferred to the load for  $C_L/C = \infty$ , but maximum energy transfer occurs for  $C_L/C = 1$ .

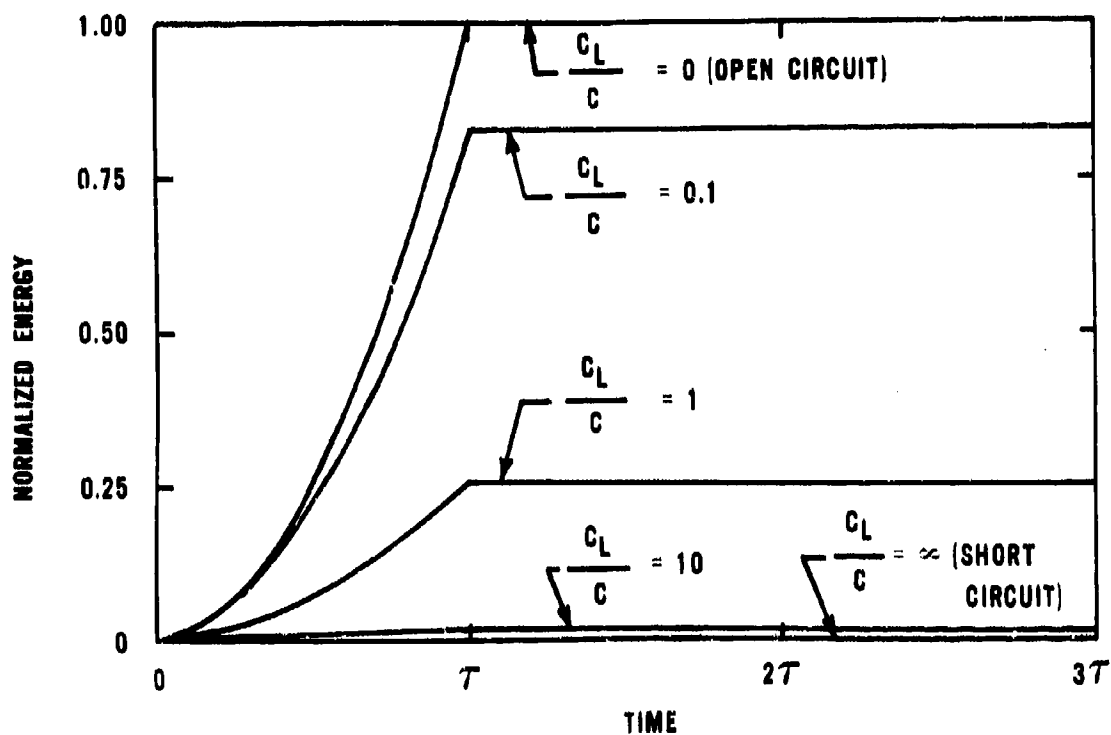


Figure A-3. Normalized energy on the PZT unit for various values of  $C_L/C$ .

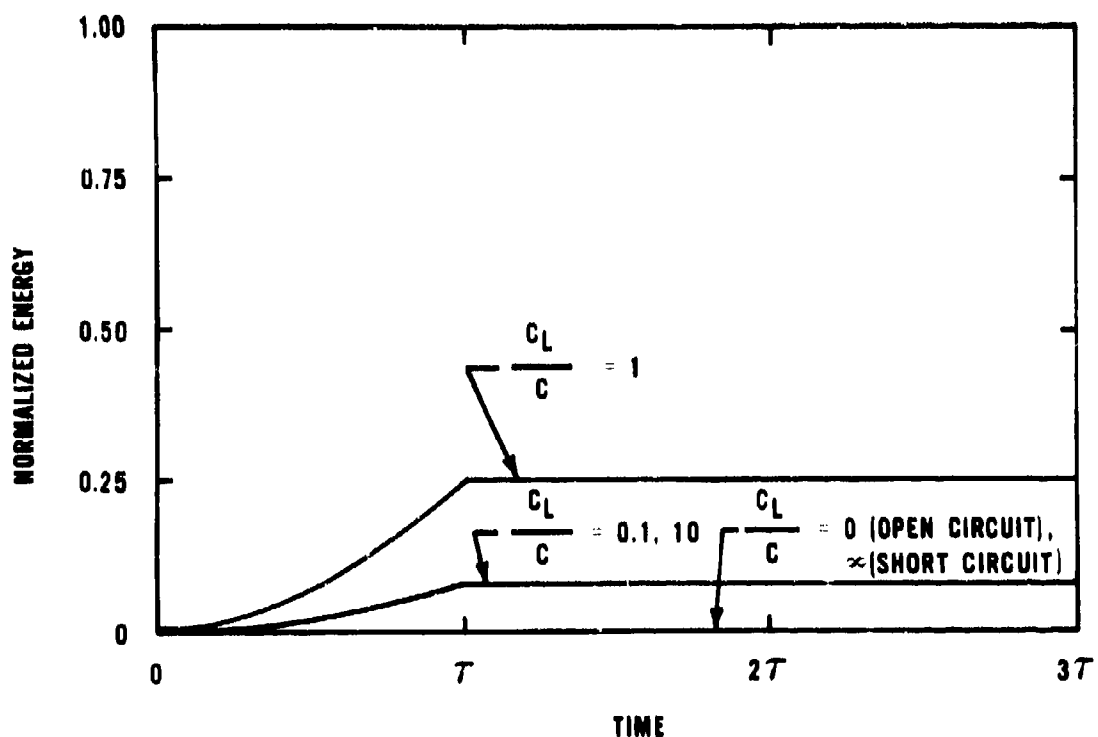


Figure A-4. Normalized energy on the load capacitor for various values of  $C_L/C$ .

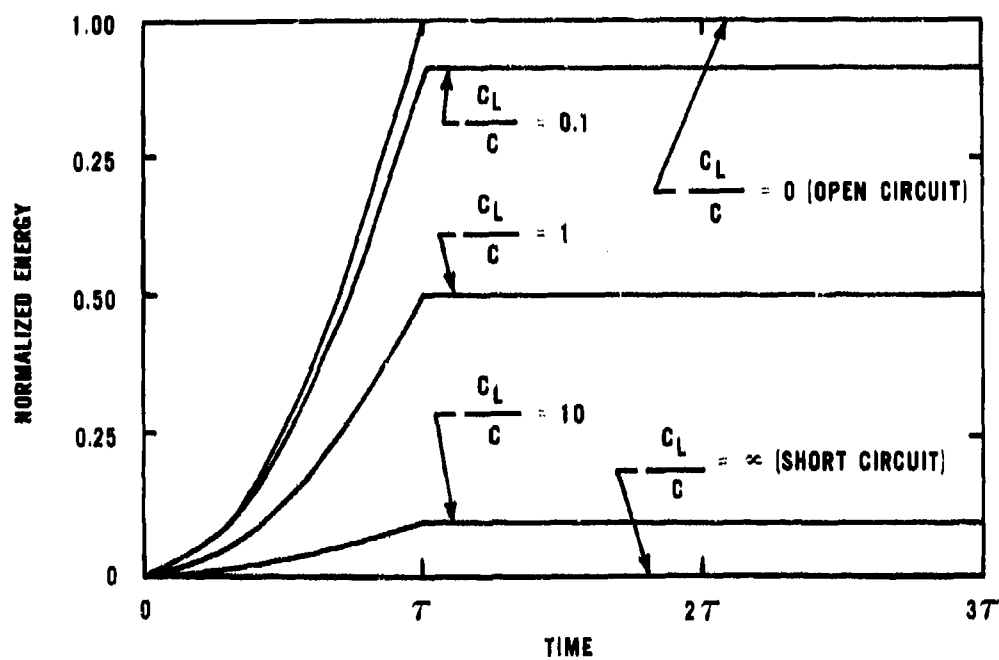
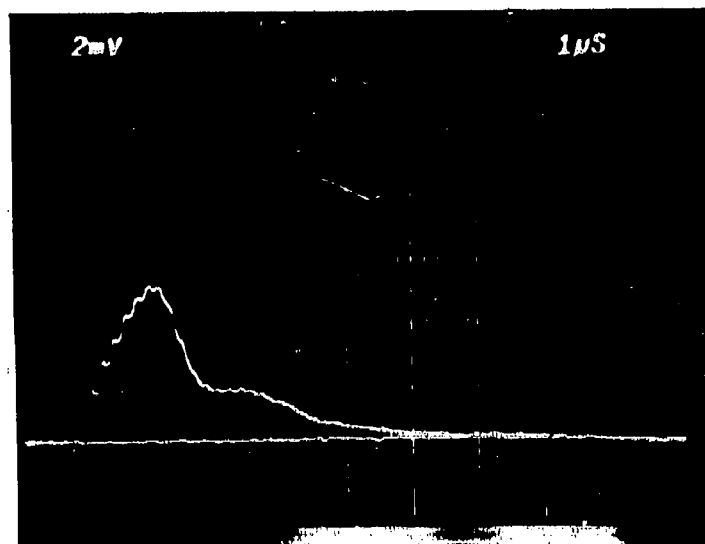


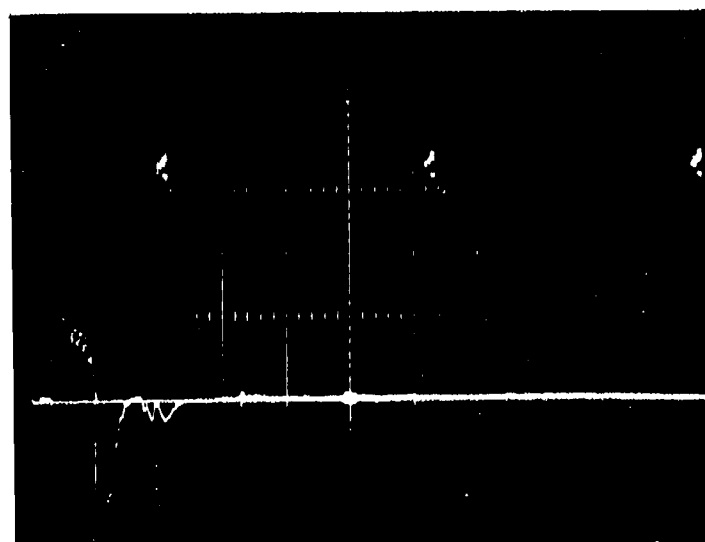
Figure A-5. Normalized circuit energy for various values of  $C_L/C$ .

**APPENDIX B**

**OSCILLOSCOPE RECORDS FOR SHOCK DEPOLING  
EXPERIMENTS**



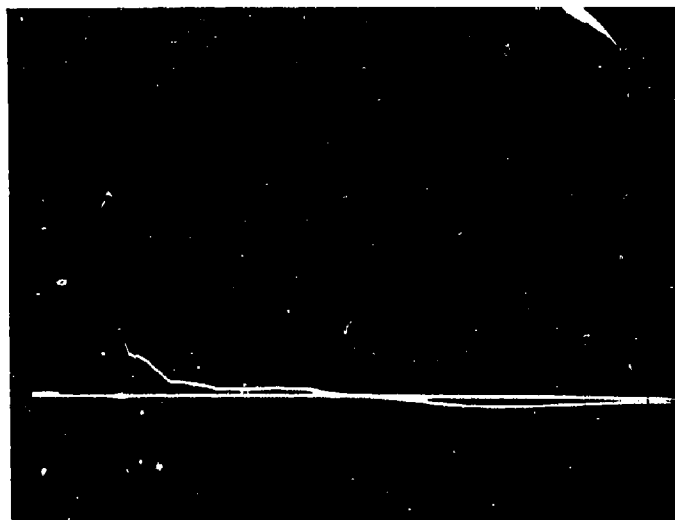
(a)



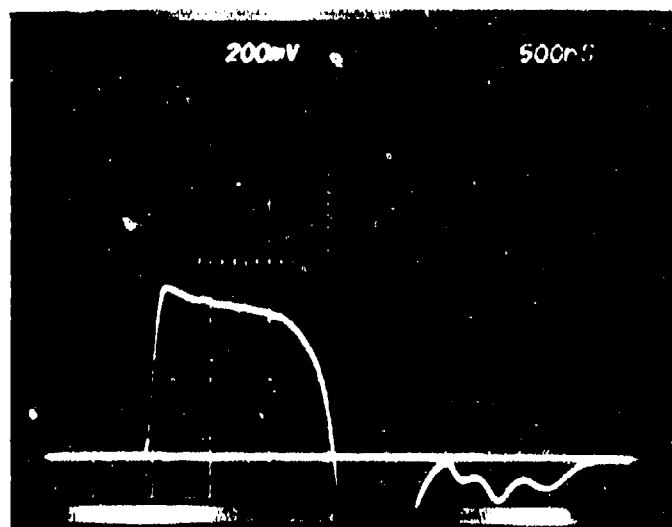
(b)

Figure B-1. Voltage and current records for Shot 12. Time increases from left to right. (a) Voltage record. The vertical scale is 14.8 kV/div, and the horizontal scale is 1  $\mu$ s/div. (b) Current record from probe in PZT/epoxy experimental configuration. The vertical scale is 10A/div, and the horizontal scale is 2  $\mu$ s/div.



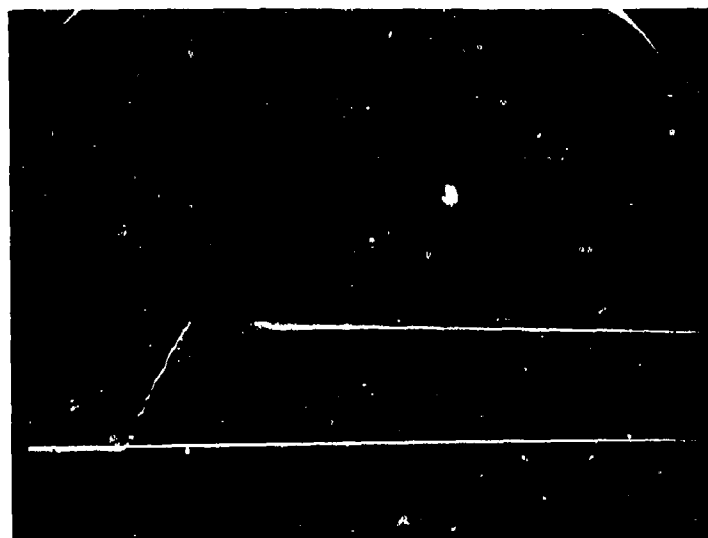


(a)

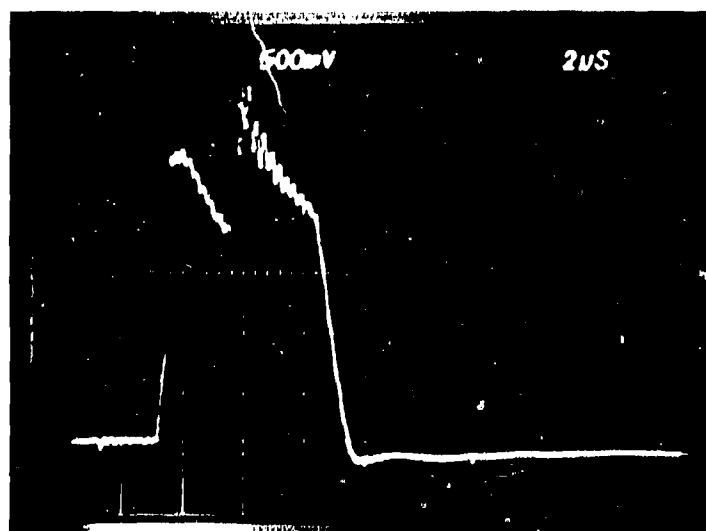


(b)

Figure B-2. Voltage and current records for Shot 15. Time increases from left to right. (a) Voltage record. The vertical scale is 14.5 kV/div, and the horizontal scale is 2  $\mu$ s/div. (b) Current record from probe in PZT/epoxy experimental configuration. The vertical scale is 4 A/div, and the horizontal scale is 0.5  $\mu$ s/div.

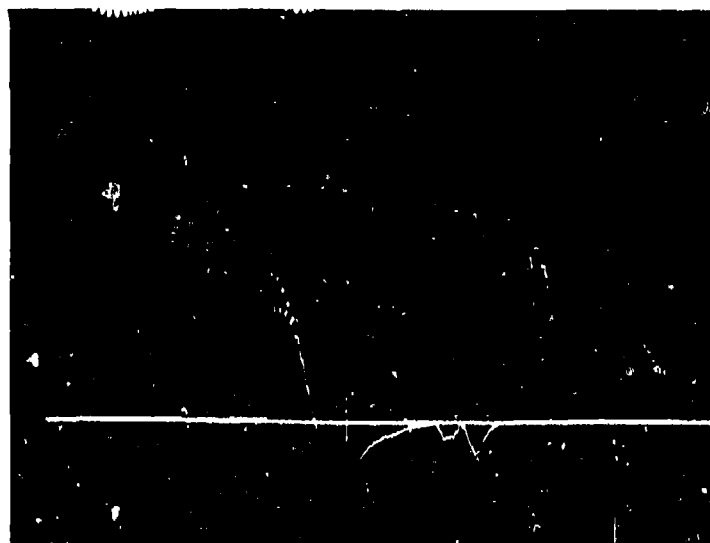


(a)

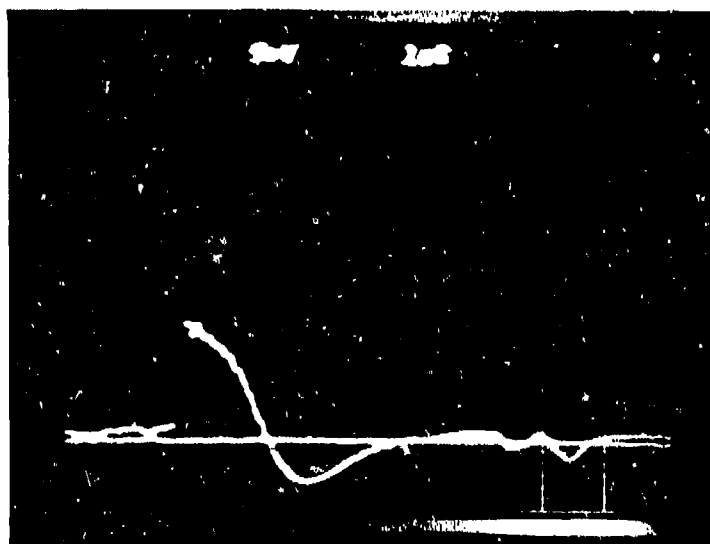


(b)

Figure B-3. Voltage and current records for Shot 16. Time increases from left to right. (a) Voltage record. The vertical scale is 35.8 kV/div, and the horizontal scale is 2  $\mu$ s/div. (b) Current record from probe in PZT/epoxy experimental configuration. The vertical scale is 10 A/div, and the horizontal scale is 2  $\mu$ s/div.

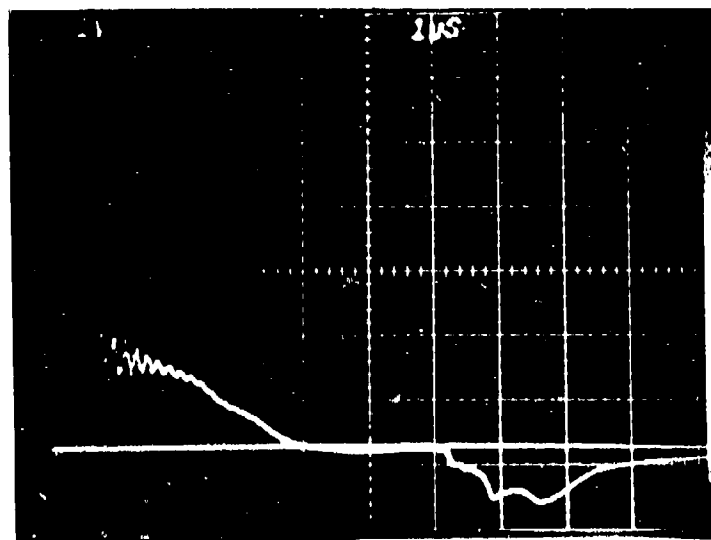


(a)

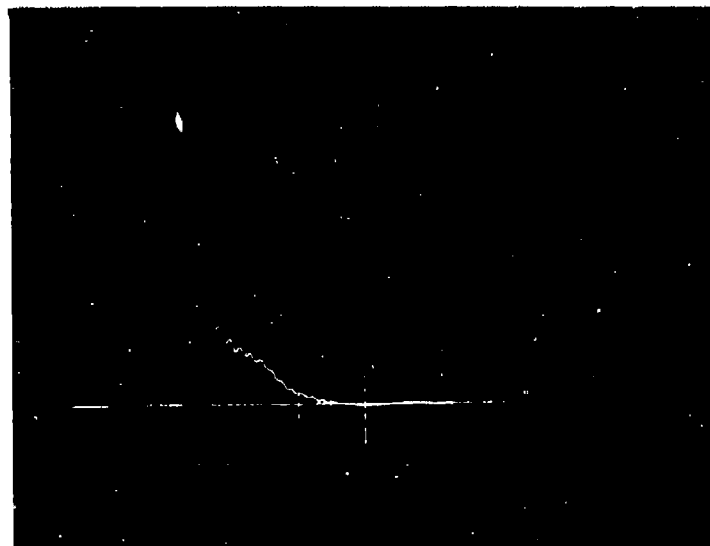


(b)

**Figure B-4.** Current records for Shot 39. Time increases from left to right. (a) Current record from probe in PZT/epoxy experimental configuration. The vertical scale is 10 A/div, and the horizontal scale is 2  $\mu$ s/div. (b) Current record from probe in oil-filled box. The vertical scale is 10 A/div, and the horizontal scale is 1  $\mu$ s/div.

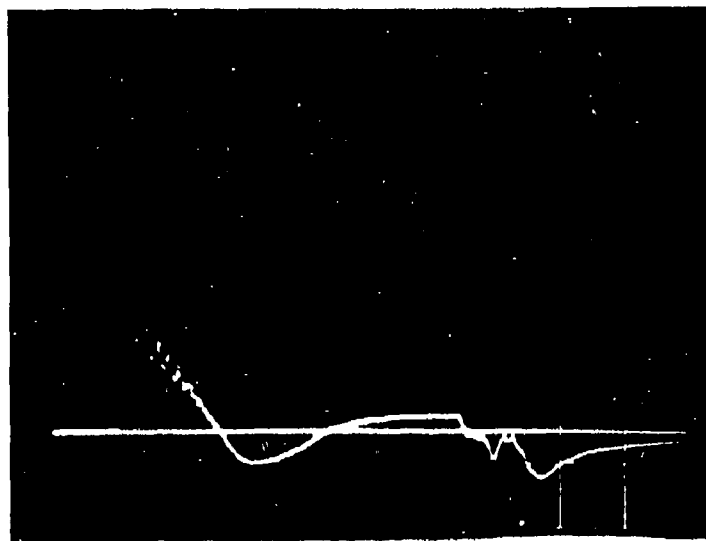


(a)

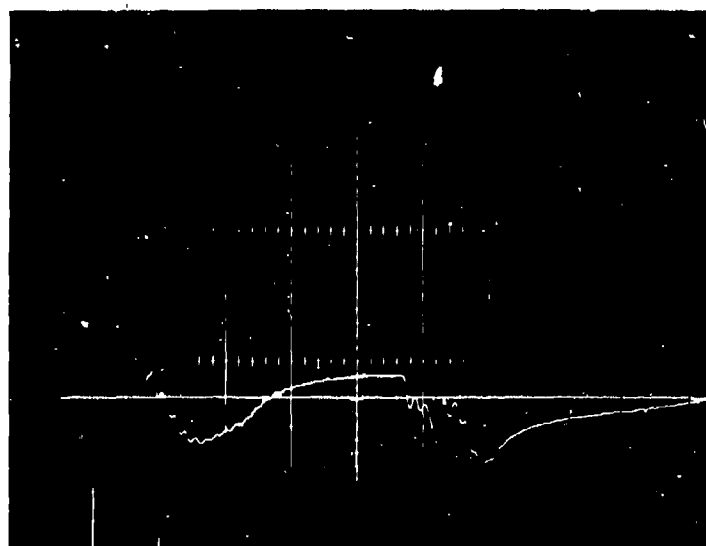


(b)

**Figure B-5.** Current records for Shot 39. Time increases from left to right. (a) Current record from probe in PZT/epoxy experimental configuration. The vertical scale is 20 A/div, and the horizontal scale is 1  $\mu$ s/div. (b) Current record for probe in oil-filled box. The vertical scale is 10 A/div, and the horizontal scale is 1  $\mu$ s/div.



(a)



(b)

Figure B-6. Current records for Shot 40. Time increases from left to right. (a) Current record for probe in PZT/epoxy experimental configuration. The vertical scale is 20 A/div, and the horizontal scale is 1  $\mu$ s/div. (b) Current record for probe in oil-filled box. The vertical scale is 10 A/div, and the horizontal scale is 1  $\mu$ s/div.

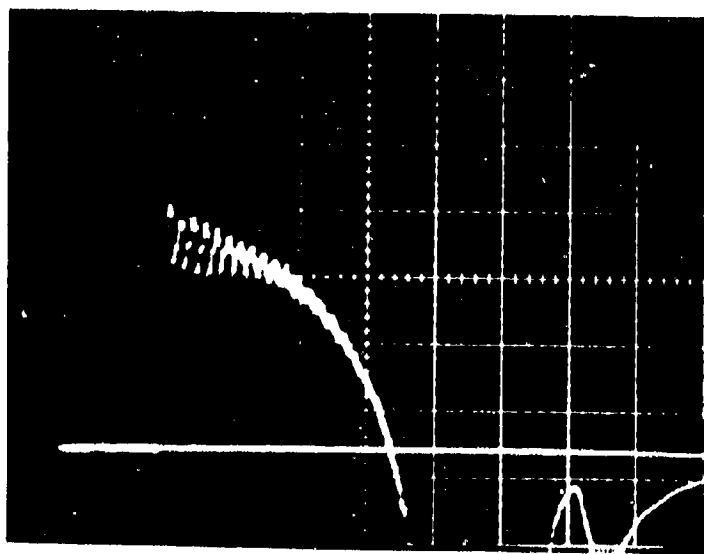
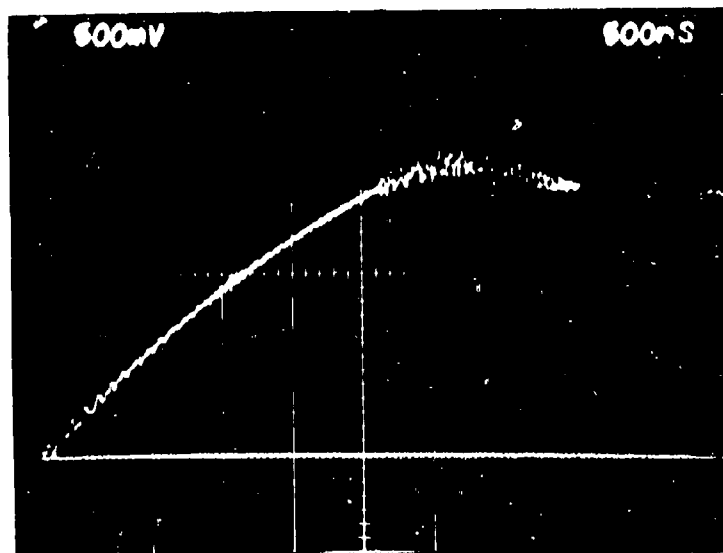
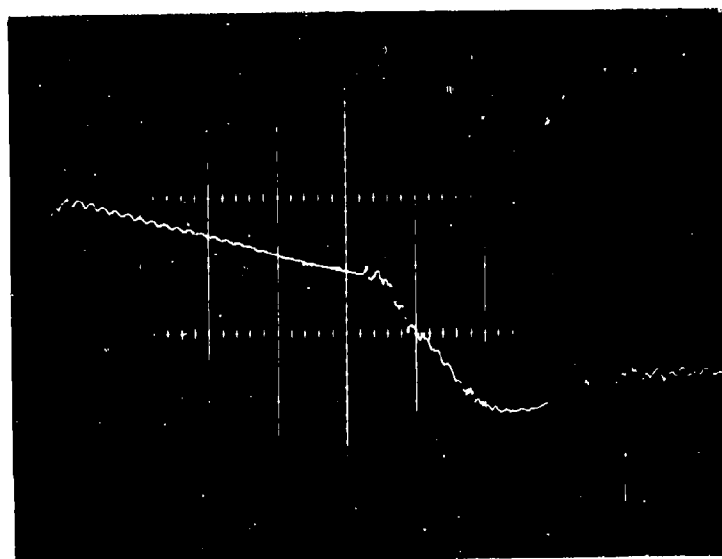


**Figure B-7.** Current record for Shot 41. Time increases from left to right. Current record from probe in PZT/epoxy experimental configuration. The vertical scale is 10 A/div, and the horizontal scale is 0.5  $\mu$ s/div.

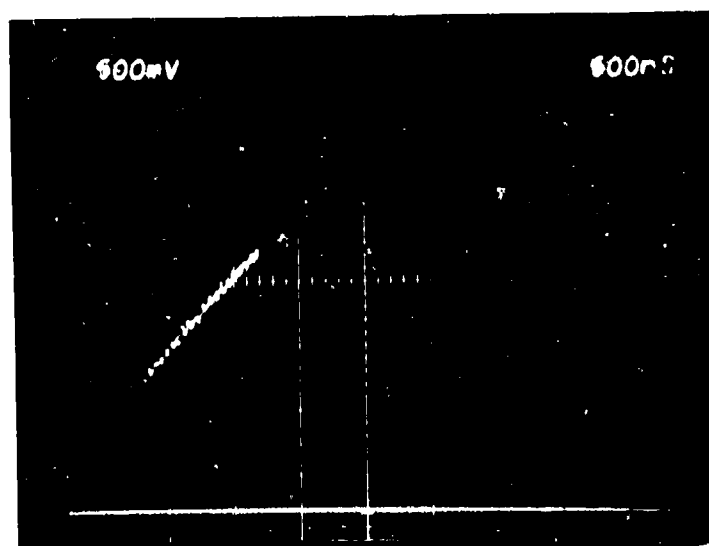


(a)

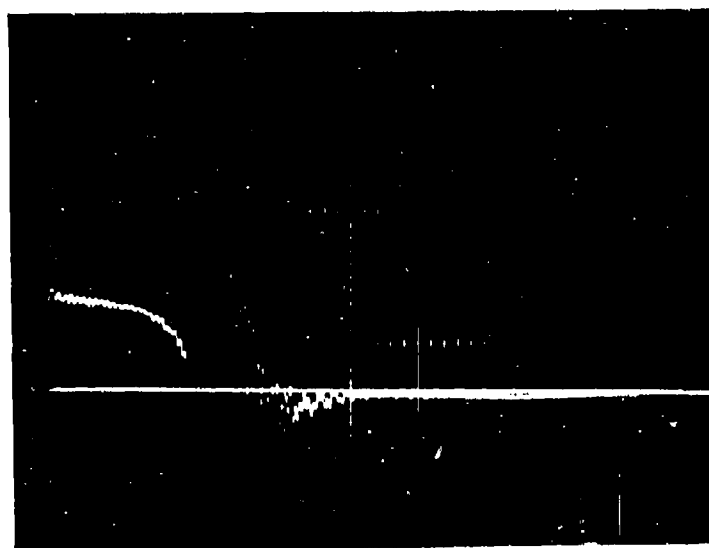


(b)

**Figure B-8.** Voltage and current records for Shot 42. Time increases from left to right. (a) Voltage record. The vertical scale is 15 kV/div, and the horizontal scale is 0.5  $\mu$ s/div. (b) Current record from probe in PZT/epoxy experimental configuration. The vertical scale is 10 A/div, and the horizontal scale is 0.5  $\mu$ s/div.



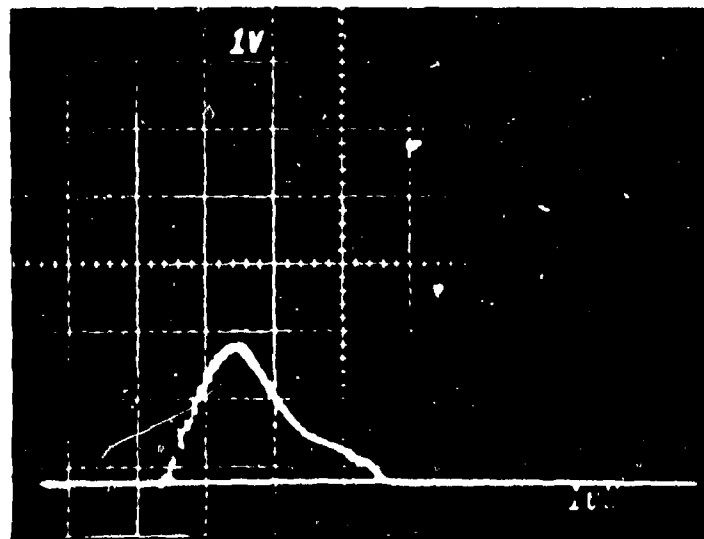
(a)



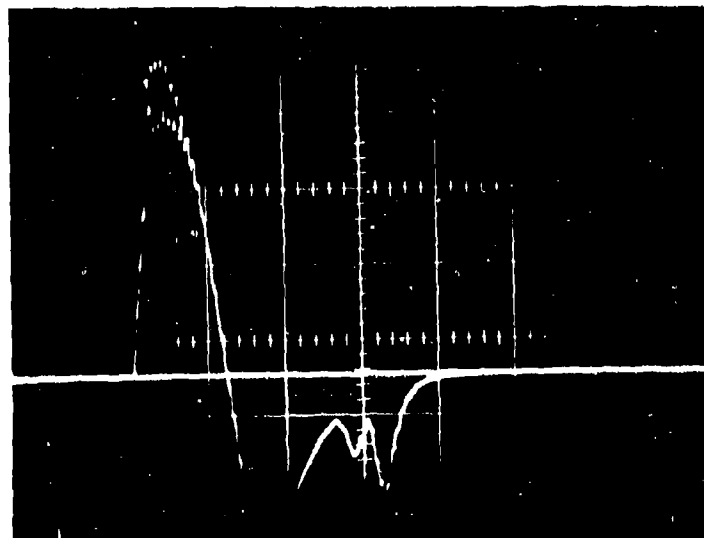
(b)

**Figure B-9.** Voltage and current records for Shot 43. Time increases from left to right. (a) Voltage record. The vertical scale is 15 kV/div, and the horizontal scale is 0.5  $\mu$ s/div. (b) Current record from probe in PZT/epoxy experimental configuration. The vertical scale is 19 A/div, and the horizontal scale is 1  $\mu$ s/div.



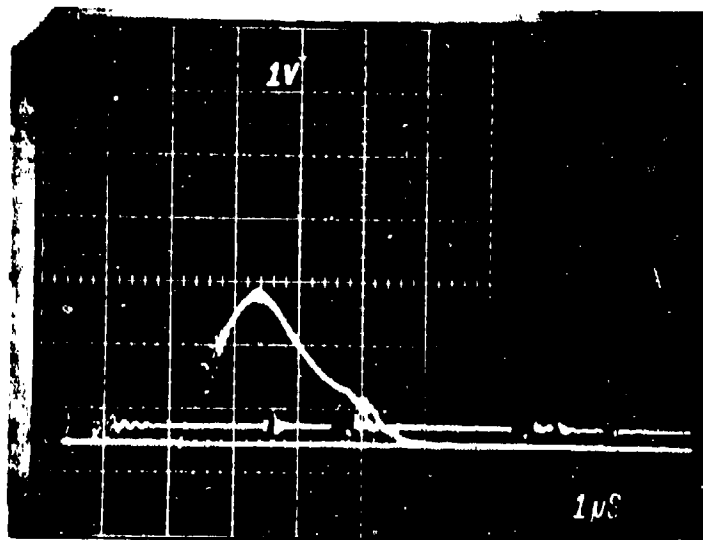


(a)

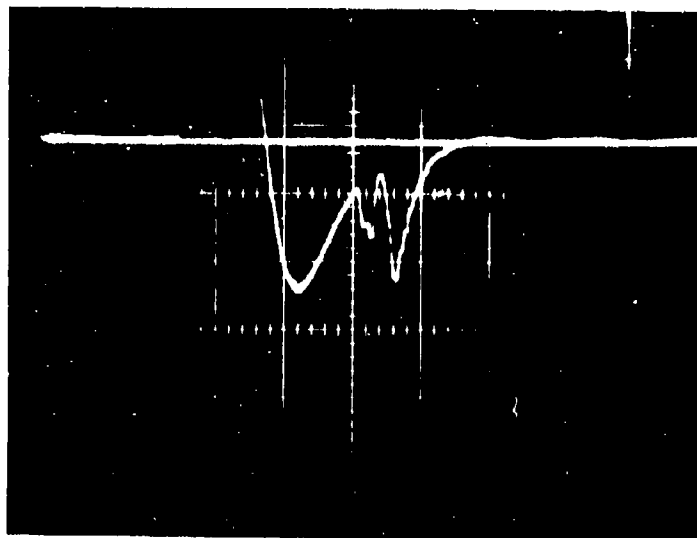


(b)

**Figure B-10.** Voltage and current records for Shot 44. Time increases from left to right. (a) Voltage record. The vertical scale is 30 kV/div, and the horizontal scale is 1  $\mu$ s/div. (b) Current record from probe in PZT/epoxy experimental configuration. The vertical scale is 10 A/div, and the horizontal scale is 1  $\mu$ s/div.

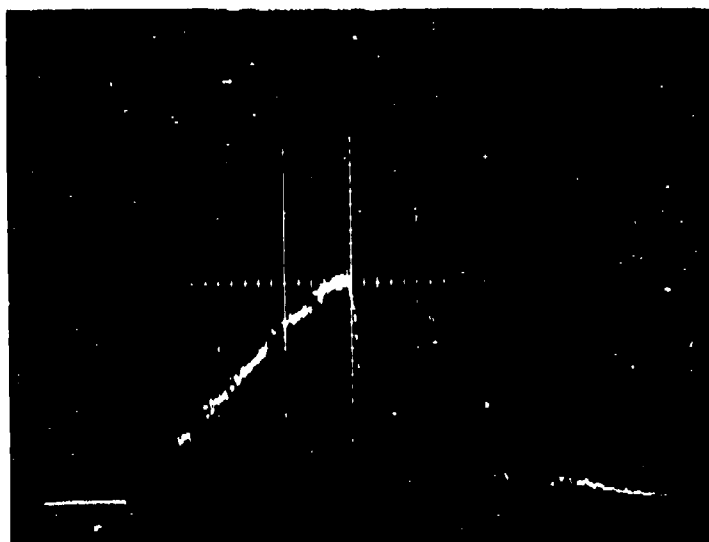


(a)

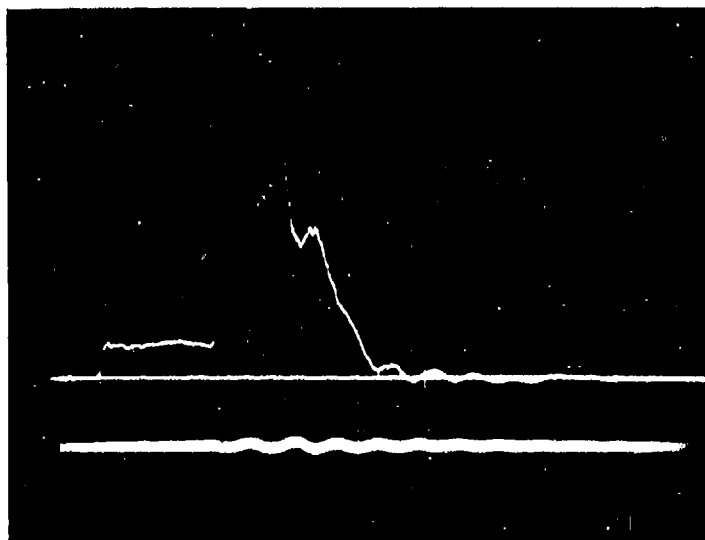


(b)

**Figure B-11.** Voltage and current records for Shot 47. Time increases from left to right. (a) Voltage record. The vertical scale is 30 kV/div, and the horizontal scale is 1  $\mu$ s/div. (b) Current record from probe in PZT/epoxy experimental configuration. The vertical scale is 10 A/div, and the horizontal scale is 1  $\mu$ s/div.



(a)



(b)

Figure B-12. Voltage and current records for Shot 58. Time increases from left to right. (a) Voltage record: The vertical scale is 15 kV/div, and the horizontal scale is 0.5  $\mu$ s/div. (b) Current record from probe in PZT/epoxy experimental configuration. The vertical scale is 20 A/div, and the horizontal scale is 1  $\mu$ s/div.



**Figure B-13.** Current record for Shot 59. Time increases from right to left. Current record from probe in the PZT/epoxy experimental configuration. The vertical scale is 10 A/div, and the horizontal scale is 1  $\mu$ s/div.

**APPENDIX C**  
**HUGONIOT RELATIONS FOR CASTALL 300 EPOXY**

**Table C-1. Explosive shock-wave data for Castall 300 epoxy.**

---

**Shot Number: 60**

**Description: Plane wave lens, Baratol pad, Castall, pinducers, manganin gauge**

**Plane Wave Lens: P-40**

**Baratol Pad Diameter (mm): 102**

**Baratol Pad Thickness (mm): 50.8**

**Baratol Composition, Fabrication: 76/24, pressed**

**Baratol Density ( $\text{Mg/m}^3$ ): 2.52**

**Castall 300 Thickness for Shock Velocity Measurement<sup>b</sup> (mm): 3.81**

**Castall 300 Thickness for Stress Measurement<sup>c</sup> (mm): 3.18**

**Castall 300 Shock Velocity (km/s): 4.48**

**Castall 300 Particle Velocity (km/s): 1.24**

**Castall 300 Shock Stress (GPa): 12.2**

**Castall 300 Strain <sup>d</sup>: 0.277**

---

<sup>a</sup> 76% barium nitrate, 24% TNT

<sup>b</sup> Shock propagation distance between two pinducers positioned in the Castall 300 epoxy.

<sup>c</sup> Shock propagation distance from Baratol/Castall 300 interface to manganin gauge.

<sup>d</sup> Calculated from the ratio of the particle velocity to the shock velocity.

**PRECEDING PAGE BLANK-NOT FILLED**

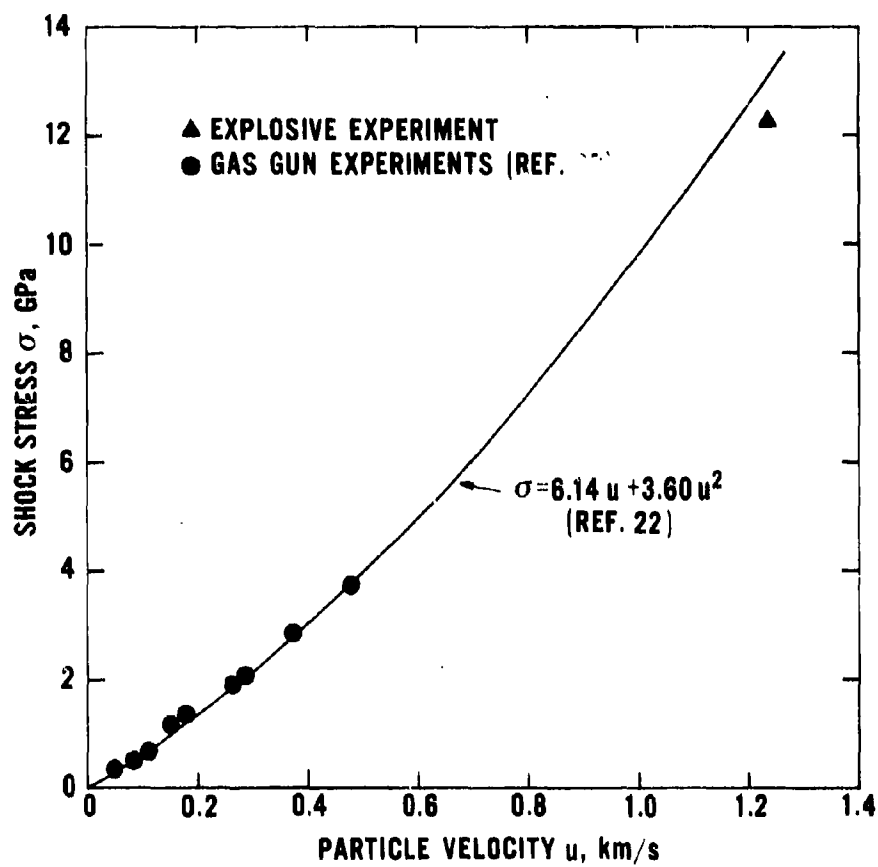


Figure C-1. Stress-particle velocity data for Castall 300 epoxy.

**APPENDIX D**

**DESCRIPTION OF BLAST CONFINEMENT CHAMBER**



A schematic of the blast confinement chamber and its appurtenant structures (also known as the NSWC/DL Explosive Chamber Facility) is shown in Figure D-1. The facility consists of the blast chamber, a capacitor bank room, and a high-speed camera room. The exterior height of the facility is 3.9 m, and the lateral dimensions are as shown in Figure D-1. The interior dimensions of the blast chamber are: 3.0 m long, 1.8 m wide, and 2.1 m high. The blast chamber walls are 0.9-m-thick steel-reinforced concrete and are lined with welded 51-mm-thick steel plates. The entrance to the chamber has a hinged 0.2-m-thick A441 steel door that is 1.4 m high and 1.1-m wide and weighs approximately  $10^3$  kg.

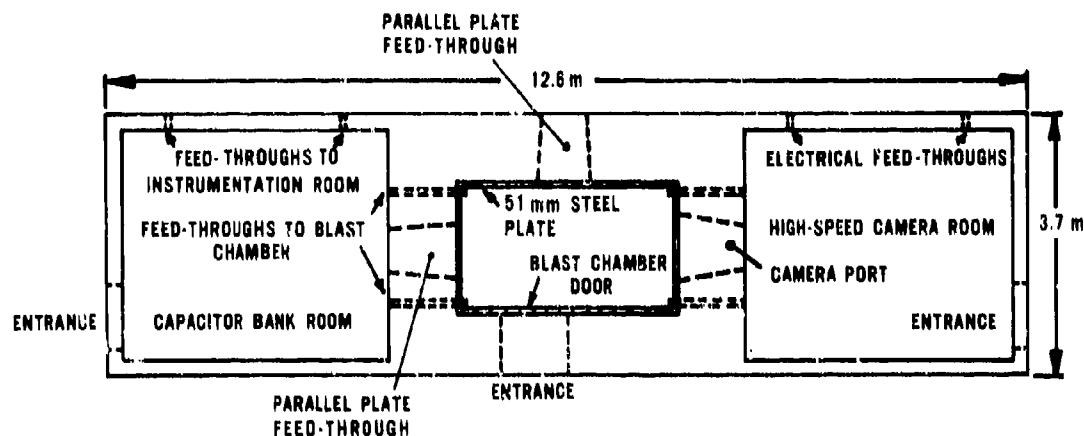


Figure D-1. Top view schematic of the blast confinement chamber (center) and appurtenant structures.

Four 58-mm-diameter steel pipe feedthroughs with threaded caps permit electrical cable access to the blast chamber from the adjacent rooms. The cables pass through holes drilled in the pipe caps. There are also two feedthroughs for low-inductance parallel-plate conductors. These openings are lined with 25-mm-thick steel plates and are tapered from 0.69 m by 76 mm on the interior to 0.61 m by 76 mm on the exterior. Tapered aluminum plugs fill the openings when not in use. The camera port consists of two circular Plexiglas plates housed in a tapered rectangular steel receptacle. Firing circuits, delay generators, oscilloscopes, and other electronic instrumentation are located in a room adjacent to the capacitor bank room.

The explosive products are vented through a 0.2-m-diameter pipe in the roof. In order to protect a large metal building that is adjacent to the facility, it was necessary to construct a blast deflector shield over the vent pipe. Approximately 100 shots involving explosive charges ranging from 453 g to 4.53 kg (TNT equivalent) have been fired with no visible structural damage to the facility. Although the blast chamber was designed for routine tests with a maximum explosive charge of approximately 45 kg, the facility has been certified safe for a maximum charge of only 4.5 kg due to the structural limitations of the blast deflector.

## DISTRIBUTION

Commander  
Naval Sea Systems Command  
Washington, DC 20360  
ATTN: SEA (S. R. Marcus)  
SEA (S. J. Matesky)  
SEA-62R (W. W. Blaine)  
SEA-62R31 (R. A. Bailey)  
SEA (G. N. Sorkin)  
SEA-62R (M. A. Kinna)  
SEA-62Y13C (L. H. Hawver)

Commander  
Naval Air Systems Command  
Washington, DC 20360  
ATTN: AIR-310B (J. W. Willis)  
AIR-320A (T. F. Kearns)  
AIR-350 (H. B. Benefiel)  
AIR-5324 (S. Englander)

Office of Naval Research  
Department of the Navy  
Washington, DC 20360  
ATTN: ONR-420 (T. G. Berlincourt)  
ONR-465 (E. I. Salkovitz)

Office of Naval Research  
536 S. Clark St.  
Chicago, IL 60605  
ATTN: George Sandoz

Office of Naval Research  
Bldg. 114 Section D  
666 Summer St.  
Boston, MA 02210  
ATTN: L. H. Peebles, Jr.

Commander  
Naval Research Laboratory  
Washington, DC 20375  
ATTN: 6370 (S. C. Sanday)  
6434 (E. Skelton)  
7908 (A. Williams)

Commander  
Naval Weapons Center  
China Lake, CA 93555  
ATTN: M. E. Backman  
R. L. Ballenger  
S. A. Finnegan  
J. Pearson  
E. B. Royce  
L. H. Smith  
T. R. Zulkoski

Director  
Army Ballistics Research Laboratories  
Terminal Ballistics Laboratory  
Aberdeen Proving Ground, MD 20015  
ATTN: W. S. deRosset  
R. E. Franz  
G. E. Hauver  
G. Moss  
R. Vitali

Commander  
Army Materials and Mechanics  
Research Center  
ATTN: D. T. Dandekar  
J. F. Mescall

Commander  
Army Research and Development  
Command  
Dover, NJ 07801  
ATTN: F. J. Owens

Commander  
Harry Diamond Laboratory  
Washington, DC 20438  
ATTN: P. S. Brody

U.S. Army Waterways Experiment  
Station  
Structures Division  
Weapons Effects Laboratory  
Vicksburg, MS 39180  
ATTN: D. R. Coltharp

Los Alamos Scientific Laboratory  
Los Alamos, NM 87544  
ATTN: J. J. Dick  
C. M. Fowler  
J. M. Holt, Jr.  
R. Morales  
Technical Library (2)

Sandia Laboratories  
Albuquerque, NM 87115  
ATTN: L. W. Davison  
R. A. Graham  
P. C. Lysne  
S. T. Montgomery

Lawrence Livermore Laboratory  
University of California  
Livermore, CA 94500  
ATTN: W. H. Gust  
E. Nidick, Jr.

Shock Dynamics Laboratory  
Washington State University  
Pullman, WA 99163  
ATTN: G. E. Duvall

Stanford Research Institute  
Poulter Laboratory  
333 Ravenswood Avenue  
Menlo Park, CA 94025  
ATTN: D. Curran  
L. Seaman

Defense Technical Information Center  
Cameron Station  
Alexandria, VA 22314 (12)

Defense Printing Service  
Washington Navy Yard  
Washington, DC 20374

Library of Congress  
Washington, DC 20540  
ATTN: Gift and Exchange Division (4)

Local:

C  
D  
E31 (GIDEP)  
E41  
F  
F10  
F12 (Berger, Jenkins, Luessen)  
G  
G05 (Soper)  
G10  
G10 (Williams)  
G13  
G20  
G25 (Bickley, Jennings, Bolt, Hales, Womack)  
G30  
G301  
G302 (Soper)  
G31  
G32  
G33  
G35  
G35 (Adams, Holt, Mock, Peterson, Wishard)  
G40  
G50  
G501  
G53  
G54  
G60  
K21 (Blackmon)  
R  
R04  
R10  
R10 (Jacobs)  
R11  
R11 (Kamlet)  
R13  
R13 (Coleburn, Erkman, Forbes, Hammond)  
R13 (Short, Roslund)  
R30  
R31  
R31 (Augl)  
R32  
R33  
R34  
X210 (6)